UNIVERSIDADE FEDERAL DE PERNAMBUCO
CENTRO DE CIÊNCIAS EXATAS E DA NATUREZA
PROGRAMA DE PÓS-GRADUAÇÃO EM FÍSICA

Nícolas Pessoa Alves

THE QUASI MODE-LOCKED REGIME

Glassy disorder and turbulent dynamics in a fiber laser

Recife

2025

Nícolas Pessoa Alves

THE QUASI MODE-LOCKED REGIME

Glassy disorder and turbulent dynamics in a fiber laser

Trabalho apresentado ao Programa de Pós-graduação em Física do Departamento de Física da Universidade Federal de Pernambuco, como requisito parcial para obtenção do título de Mestre em Física.

Área de Concentração: Óptica

Orientador (a): Marcio Heraclyto Gonçalves de Miranda

Recife

2025

.Catalogação de Publicação na Fonte. UFPE - Biblioteca Central

Alves, Nicolas Pessoa.
   The quasi mode-locked regime: glassy disorder and turbulent dynamics in fiber laser / Nicolas Pessoa Alves. - Recife, 2025.
   163 f.: il.

   Dissertação (Mestrado) - Universidade Federal de Pernambuco, Centro de Ciências Exatas e da Natureza, Programa de Pós-Graduação em Física, 2025.
   Orientação: Marcio Heraclyto Gonçalves de Miranda.
   Coorientação: Cid Bartolomeu de Araújo.
   Inclui referências e anexo.

   1. Quasi modo-travado; 2. Quebra de simetria de réplica; 3. Turbulência. I. Miranda, Marcio Heraclyto Gonçalves de. II. Araújo, Cid Bartolomeu de. III. Título.

UFPE-Biblioteca Central

NÍCOLAS PESSOA ALVES

THE QUASI MODE-LOCKED REGIME: GLASSY DISORDER AND TURBULENT DYNAMICS IN FIBER LASER

Dissertação apresentada ao Programa de Pós-Graduação em Física da Universidade Federal de Pernambuco, como requisito parcial para a obtenção do título de Mestre em Física.

Área de Concentração: Óptica

Data de aprovação: 29/08/2025.

BANCA EXAMINADORA

_____

Prof. Dr. Marcio Heraclyto Gonçalves de Miranda
Orientador
Universidade Federal de Pernambuco

_____

Prof. Dr. Anderson Monteiro Amaral
Examinador Interno
Universidade Federal de Pernambuco

_____

Prof. Dr. Gustavo Silva Wiederhecker
Examinador Externo
Universidade Estadual de Campinas

I dedicate this work to Time, the only one capable of transforming the words herein written into lies.

"Science knows no country, because knowledge belongs to humanity, and is the torch which illuminates the world." Louis Pasteur (DUBOS, 1950, p. 85) .

ABSTRACT

In this work, we investigate the quasi mode-locked (QML) regime in a Yb-doped mode-locked fiber laser, a new and largely unexplored operating phase where intensity fluctuations reveal complex collective behavior. Although this regime may be familiar to experimentalists working with mode-locked lasers, the QML has not been systematically studied in a fiber laser, and only recently has its importance begun to emerge. QML typically appears in the intermediate region between continuous-wave (CW) operation and the standard mode-locking (SLM). To characterize this regime, we turn to statistical analysis, which offers us powerful ways to uncover the underlying dynamics and emergent properties of the laser. By collecting realizations (replicas) of the laser output and examining their correlations, we identify signatures of glassy dynamics, including replica symmetry breaking (RSB). This situates the QML phase as a new optical platform — complementary to random lasers (RLs) — for connecting concepts from disordered magnetic systems to photonics. Beyond its glassy features, the QML regime also displays turbulence-like behavior. By employing a dynamical stochastic model (H-theory), we characterize Gaussian and non-Gaussian distributions on the intensity increments of the spectra, which reveal the presence of intermittent fluctuations and scaling behavior typical of turbulence-like dynamics. Principal component analysis (PCA) is also used to reduce the dimensionality of the data, allowing us to find hidden structures in the data and enabling a more robust identification of scaling regimes. The results presented in this dissertation provide experimental evidence of turbulence in a optical phase of a fiber laser supporting mode-locking operation. Understanding QML is not only important in itself, but also helps us to better comprehend the fully mode-locked regime, which is of central relevance for ultra-fast laser applications. Insights gained from studying QML can shed light on how pulses form, what determines their stability, and so on. Overall, this dissertation establishes the QML regime as a distinct and valuable optical phase for exploring complex collective phenomena in light. By bridging ideas from statistical physics, nonlinear dynamics, and photonics, we highlight the role of interaction in shaping laser dynamics, and we open new directions for understanding complexity in optical systems.

Keywords: Quasi Mode-Locking (QML). Replica Symmetry Breaking (RSB). Turbulence. Principal Component Analysis (PCA).

RESUMO

Neste trabalho, investigamos o regime Quasi Modos-travados (QMT) em lasers de fibra dopados com Yb. O QMT é uma fase operacional ainda pouco explorada, marcada por flutuações de intensidade que revelam comportamentos coletivos complexos. Embora já conhecida por experimentalistas que trabalham com lasers de modos-travados, essa fase não foi estudada sistematicamente em um laser de fibra, com sua relevância só começando a ganhar destaque recentemente. O QML surge tipicamente na região intermediária entre a operação em onda contínua (OC) e o modo-travado padrão (MTP). Para caracterizar esse regime, utilizamos ferramentas estatísticas capazes de revelar dinâmicas subjacentes e propriedades emergentes do laser. A partir da análise da emissão e de suas correlações, identificamos assinaturas típicas de sistemas vítreos, incluindo a quebra de simetria de réplica (QSR). Assim, o QML se estabelece como uma nova plataforma — complementar aos lasers aleatórios (LAs) — para aproximar conceitos da física de sistemas desordenados à fotônica. Além das características vítreas, o QML também apresenta dinâmicas semelhantes à turbulência em fluidos. Por meio de um modelo estocástico dinâmico (Teoria-H), caracterizamos distribuições Gaussianas e não-Gaussianas nos incrementos de intensidade espectral, evidenciando flutuações intermitentes e leis de escala típicas de sistemas turbulentos. A análise de componentes principais (ACP) também foi aplicada para reduzir a dimensionalidade dos dados, revelando estruturas ocultas e permitindo identificar com maior robustez os diferentes regimes. Os resultados apresentados aqui constituem uma evidência experimental de turbulência na fase óptica de um laser de fibra que suporta o travamento de modos. O estudo do QML contribui para uma compreensão mais profunda do regime modo-travado, fundamental em aplicações de lasers ultrarrápidos. As informações obtidas elucidam como os pulsos se formam, quais fatores determinam sua estabilidade e outros aspectos críticos da dinâmica laser. Em síntese, este trabalho consolida o regime QML como uma fase óptica distinta e promissora para investigar fenômenos coletivos da luz. Ao integrar conceitos da física estatística, da dinâmica não linear e da fotônica, evidenciamos o papel das interações na evolução da dinâmica de lasers, abrindo novas perspectivas para o estudo da complexidade em sistemas ópticos.

Palavras-chaves: Quasi modo-travado (QMT). Quebra de simetria de réplica (QSR). Turbulência. Análise de componentes principais (ACP).

LIST OF FIGURES

LISTA DE CÓDIGOS

LIST OF TABLES

LIST OF ABBREVIATIONS AND ACRONYMS

AF	Antiferromagnetic
BS	Beamsplitter
COLL.	Collimator
CW	Continuous-Wave
DG	Diffraction-Grating
DL	Diode Laser
DMI	Dzyaloshinskii-Moriya interaction
EA	Edwards-Anderson
FD	Photodetector
FM	Ferromagnetic
FMC	Frequency Matching Condition
FWHM	Full Width at Half Maximum
GVD	Group Velocity Dispersion
HWP	Half-Wave Plate
IFO	Intensity Fluctuation Overlap
K41	1941 Kolmogorov's Theory
K62	1962 Kolmogorov's Theory
LASER	Light Amplification by Stimulated Emission of Radiation
MLFL	Mode-locked Fiber Laser
MTF	Mean Field Theory
NLSE	Nonlinear Schrödinger Equation
NPR	Nonlinear Polarization Rotation
NSE	Navier-Stokes Equation
OI	Optical Isolator
PBS	Polarized Beamsplitter

PC	Principal Component
PCA	Principal Component Analysis
PCC	Pearson Correlation Coefficient
PLW	Phase Locking Wave
POP	Photonic Overlap Parameter
QML	Quasi-Mode-Locking
QWP	Quarter-Wave Plate
RKKY	Ruderman–Kittel–Kasuya–Yosida
RL	Random Laser
RMSE	Root Mean Square Error
RSB	Replica Symmetry Breaking
SA	Saturable Absorber
SAM	Self-Amplitude Modulation
SK	Sherrington-Kirkpatrick
SML	Standard Mode-Locked
SNR	signal-to-noise ratio
SPM	Self-Phase Modulation
TAP	Thouless-Anderson-Palmer
WDM	Wavelength Division Multiplexing
XPM	Cross-Phase Modulation
YDF	Yb-Doped Fiber

CONTENTS

1 INTRODUCTION

The study of complex physical systems occupies a special position in modern physics, not only because of the intrinsic intellectual challenge they pose, but also because of the unexpected bridges that appear between seemingly distant areas of research. Although identifying features shared by all complex systems is a challenging task, a useful — though perhaps not sufficient — approach is to view them in terms of their interactions (ESTRADA, 2023). In a complex system, the whole influences the parts, the parts shape the nature of the whole, and these influences flow both ways in a deep and inseparable manner. Therefore, fully understanding these systems requires a conceptual toolkit that transcends the boundaries of individual disciplines, as well as experimental platforms capable of capturing their subtleties.

Spin glasses are among the many categories of complex systems. They are magnetic materials in which the internal atomic moments interact via random couplings arranged in a spatially disordered fashion. The combined effects of disorder and frustration give rise to a remarkable low-temperature phase: the spins "freeze" into disordered configurations, producing a state that lacks conventional long-range magnetic order but remains highly correlated. The formal study of these materials in the latter half of the twentieth century led to profound theoretical advances, most notably the Replica Symmetry Breaking (RSB) theory introduced by the Italian physicist Giorgio Parisi. This purely statistical framework posits that the free-energy landscape of spin glasses is organized into a hierarchy of metastable states separated by energy barriers of many scales. The significance of this insight, which by the end of the century was shown to extend well beyond magnetism, was recognized in 2021 when Parisi was awarded the Nobel Prize in Physics (PHYSICS, 2021; NOBELPRIZE.ORG, 2021b).

For many years, the evidence supporting RSB came entirely from theory and numerical simulations (BARAHONA, 1982; YOUNG, 1983; KATZGRABER; PALASSINI; YOUNG, 2001), as direct experiments in magnetic systems were impractical—or even impossible. Verifying RSB requires knowledge of the distribution of overlaps between different equilibrium states of the same disorder realization. Experimentally, this is unfeasible because it is impossible to prepare two identical spin glasses and measure their full spin configurations. Also, macroscopic elements like magnetization or susceptibility only provide averaged information. In addition, the extremely slow dynamics of spin glasses prevent them from reaching true equilibrium, so any apparent RSB signature could be masked by non-equilibrium effects.

A turning point occurred when analogies were drawn between spin glasses and disordered photonic systems, particularly in the context of random lasers (RLs) (ANGELANI et al., 2006a). In these lasers, the feedback is not provided by a traditional mirror-based cavity. Instead, it comes from multiple scattering processes within a disordered gain medium, creating a situation in which the electromagnetic field experiences a complex interference landscape akin to the spin configurations in a glassy magnet. The influential work of Angelani et al. (2006a) demonstrated that, under certain approximations, the dynamics of the optical modes in a RL could be mapped onto a disordered Hamiltonian with the same structure as that of a spin glass. This mapping was not merely an analogy; it predicted that a true thermodynamic glass transition, accompanied by RSB, should occur in such systems. This prediction was later confirmed experimentally (GHOFRANIHA et al., 2015; GOMES et al., 2016b).

Since that first observation, RSB has been identified in an expanding range of optical platforms, most recently in a Mode-locked Fiber Laser (MLFL) (ALVES et al., 2024). This system is of particular relevance to this dissertation, since it is the one we will base our work. In the mode-locked regime, the longitudinal modes of the laser cavity become phase-synchronized, generating ultrashort pulses whose formation and stability depend sensitively on the balance of dispersion, nonlinearity, gain, and loss (CAMPOS, 2020). A remarkable aspect of this work is the identification of a phase preceding Standard Mode-Locked (SML), known as the Quasi-Mode-Locking (QML) regime, which can be characterized as a glassy transition from basic Continuous-Wave (CW) operation to the SML and is described by RSB. Thus, this system provides a new platform to verify RSB theory, while also uncovering insights into pulse dynamics.

In parallel with these developments, a second conceptual connection has begun to attract attention: the link between photonics and turbulence. Turbulence, long considered one of the most difficult challenges in classical physics, is characterized by multiscale energy cascades, intermittency, and strongly non-Gaussian statistics. Remarkably, these features have been observed in the intensity fluctuations of random lasers (GONZÁLEZ et al., 2017) and have appeared as indicators in the QML regime. This suggests that the tools of turbulence theory can be profitably applied to optical data. Furthermore, models such as the H-theory (GONZÁLEZ, 2017) provide a natural language for systems whose dynamics are governed by a hierarchy of coupled processes occurring on well-separated time scales, a situation that arises in both hydrodynamic turbulence and complex laser dynamics.

This work has three intertwined goals. First, it focuses on offering a comprehensive and

in-depth study of the QML region, a regime familiar to experimentalists in daily laboratory practice. Second, and the most straightforward, is to present original experimental results and analysis on the subjects of RSB and turbulence-like statistics occurring in a single optical platform — namely, a Yb-doped Mode-locked Fiber Laser (MLFL) operating via Nonlinear Polarization Rotation (NPR). Third, but by no means least, is to consolidate, in a unified text, the theoretical and experimental background needed to undertake such studies, thereby producing a resource for researchers entering the field.

This dissertation represents a compilation of my studies during my master's program. The text is structured as introductory material that leads the reader from the theory of magnetic spin glasses, through its translation into the optical domain, to a detailed description of our experimental system, and concludes with an introduction to statistical approaches to turbulence, analysis techniques, and their manifestation in our system. Despite being extensive, this dissertation does not delve into complex mathematical details—a point consistently reaffirmed throughout the text. Instead, it is rich in references that can be used to explore each topic in greater depth. Together, these references and the dissertation itself form a powerful theoretical archive for the study of disordered optical systems and their connections. Although the chapters are interconnected, each can be read independently, allowing readers to grasp the essential ideas of a section without reading the entire work.

The dissertation is organized into six main chapters:

- Chapter 2 provides a thorough introduction to the physics of spin glasses. It discusses the key ingredients of disorder, mixed interactions, and frustration, and reviews the canonical models along with the replica method and Parisi's hierarchical RSB solution. This chapter's goal is to ensure that readers are equipped with the theoretical constructs originally devised for magnetic systems.

- Chapter 3 develops the analogy between spin glasses and disordered photonic systems. It reviews the physics of conventional and RLs, the role of multiple scattering as a feedback mechanism, and the mapping of multimode phase dynamics onto spin-glass. The chapter also surveys the key experimental demonstrations of RSB in optical media, setting the stage for the specific system studied here.

- Chapter 4 deals with the elements regarding the experiment. It describes in detail the core elements of the Yb-doped MLFL, the mode-locking process via NPR, and the

identification of the QML glassy phase preceding stable mode locking operation. The statistical analysis of fluctuations is presented, with a focus on the overlap parameter as a diagnostic for RSB.

- Chapter 5 is devoted to the theoretical background of turbulence. It introduces the essential concepts of turbulence, presented from a simplified historical perspective, and establishes the statistical framework used in the analysis. Particular emphasis is given to the H-theory and to multivariate tools such as PCA, which serve as the methodological basis for the following chapter.

- Chapter 6 applies these concepts to our experimental system. We begin with a description of the experimental apparatus and numerical procedures, followed by the statistical analysis of the data. While the main focus is on the QML regime, for completeness we also show results for the CW and SML phases. This chapter consolidates the interpretation of the findings and establishes the presence of turbulent signatures in the QML phase.

- Chapter 7 offers conclusions and perspectives. It synthesizes the main findings, discusses their implications for the understanding of complex optical systems, and suggests possible avenues for future research.

Together, these elements position the dissertation as both a scientific contribution and a guide for researchers, highlighting the QML regime and its impact and connection with several topics of interest in the scientific literature.

2 PRINCIPLES OF MAGNETIC SPIN GLASSES

In 2021, the Royal Swedish Academy of Sciences awarded the Nobel Prize in Physics for groundbreaking contributions that have profoundly advanced our understanding of complex physical systems. Half of the prize was awarded to Giorgio Parisi "for the discovery of the interplay of disorder and fluctuations in physical systems from atomic to planetary scales" (NOBELPRIZE.ORG, 2021b). Parisi's research centered on unraveling the intricate behavior of disordered systems, particularly on spin glasses, a unique class of materials where magnetic interactions create complex, frozen states. His development of the theory not only demonstrated how disorder and randomness can give rise to hidden order and structure in spin glasses, but also established a universal framework for analyzing complexity across different physical systems. As the Nobel Committee for Physics stated, "Giorgio Parisi has been involved in uncovering the scaffolding of, and developing the tendrils between, a stunning range of physical systems" (PHYSICS, 2021). To unravel these connections, we must first contextualize the physics of spin glasses and some kind of theoretical approach. Although spin glasses originated in condensed matter physics, their mathematical structure and emergent behavior is closely connected to photonic systems. In this chapter, we present the general concept of magnetic spin glasses, focusing on their random coupling interactions and the resulting frustration. We introduce the Edwards-Anderson lattice model and the infinite-range Sherrington-Kirkpatrick model as foundational theoretical approaches to the spin glass phase, describe the replica method, and discuss its implications. We also outline Parisi's hierarchical Replica Symmetry Breaking (RSB) ansatz as a solution to the limitations of the infinite-range model, while avoiding a deep formalism.

2.1 MAGNETIC SPIN GLASSES

To understand spin glasses, one must first ask the following: What is glass? In condensed matter physics, most solids studied are crystals. In this state, the equilibrium configuration of atoms forms a translationally periodic array with long-range order. In contrast, an amorphous solid lacks long-range atomic order; its equilibrium atomic positions form a disordered array. Glass falls into the category of an amorphous solid (ZALLEN, 1998). Fig. 1 illustrates the lattice configurations of these two structural states.

Figure 1 – Schematic drawings of the atomic arrangement in (a) a crystalline solid and (b) an amorphous solid (glass).

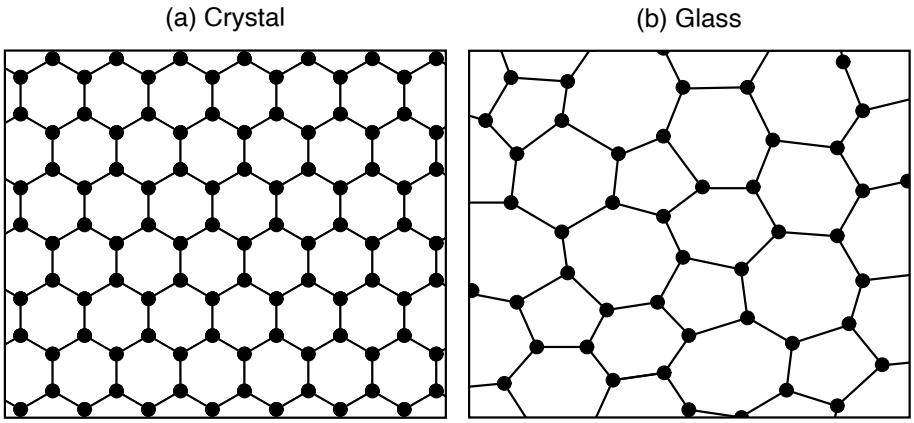

Source: Adapted from ZALLEN (1998)

In Fig. 1a, the atoms are arranged in a neat, periodic, hexagonal structure, with uniform near-neighbor distances and bond lengths. In Fig. 1b, distances and bonds vary, and there is no well-defined periodicity[1]. The glass state of a substance forms when a liquid is rapidly cooled, causing the atoms to freeze into well-defined equilibrium positions around where they oscillate. Spin glasses represent the magnetic analogue of this state. They occur in materials where the atomic lattice can retain a crystal-like structure, but their spins (magnetic moments) adopt a frozen disordered configuration.

To better understand this concept, we shall play a spin 'coupling game' in a regular two-dimensional triangular lattice, where the lattice sites are represented by blue dots in Fig. 2.

Figure 2 – Illustration of a two-dimensional triangular lattice with (a) non-interacting spins, (b) spins coupled exclusively via FM interactions, and (c) a single AF interaction introducing frustration into the lattice.

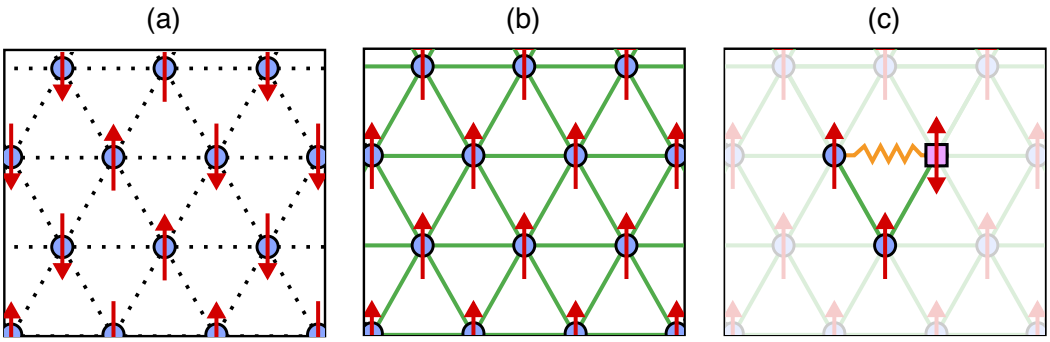

Source: The Author (2025)

[1]Although the atomic arrangement in a glass state seems random, there is significant local correlation. Both glass and crystals exhibit a high level of short-range order, but differ in terms of long-range order, with glass lacking it and becoming essentially random (ZALLEN, 1998).

First, for simplicity, let us assume, for now, that we are dealing with Ising spins, which can only adopt an 'up' ($\uparrow$) or 'down' ($\downarrow$) configuration. Second, each spin interacts with its neighbors through ferromagnetic (FM) or antiferromagnetic (AF) coupling: In ferromagnetic interactions, spins tend to align in a parallel configuration ($\uparrow\uparrow$), while antiferromagnetic interactions result in an antiparallel alignment ($\uparrow\downarrow$).

In the absence of magnetic interactions among moments (dashed lines in Fig. 2a), each site randomly adopts an $\uparrow$ or $\downarrow$ orientation. This state can be achieved by introducing thermal energy, where thermal fluctuations overpower interactions, causing the spins to randomly reorient over time (STEIN, 1989). In this configuration, the lattice exhibits, on average, equal proportions of $\uparrow$ and $\downarrow$ spins. This corresponds to a paramagnetic phase, characterized by non-cooperative behavior in spin coupling (HURD, 1982). Let us 'turn on' the magnetic interaction by reducing the temperature until the thermal effects become negligible. When only FM interactions are present (depicted by solid green lines in Fig. 2b), the spins will tend to align in a uniform direction. Below a certain critical temperature T_c, the configuration of the atoms changes abruptly, aligning the majority of the moments in a unified direction. This minimizes the system's energy, yielding a unique ground state at zero temperature where all spins are completely parallel. At T_c, the lattice has experienced a phase transition from paramagnetic to ferromagnetic (STEIN, 1989).

Complexity arises when we randomly replace a single FM bond with an AF one (zigzag orange line in Fig. 2c). Evidently, the spin at the square pink site cannot satisfy all bonds simultaneously. An upward orientation violates the AF coupling (J_-) with the left neighbor; a downward orientation disrupts the FM bonds (J_+) with the others. When the bonds are of equal strength, there is a tendency for the spin to align upward, since this configuration results in the fewest unsatisfied connections and has the lower energy. However, if $|J_-| = 5|J_+|$, where the factor 5 corresponds to the number of ferromagnetic bonds associated with the site in question, the spin cannot align in a way that simultaneously satisfies all interactions or lowers the energy. That is, there is no longer a clear tendency toward a minimum-energy configuration, since any choice the site makes results in the same total energy. From this perspective, it does not matter if the spin is oriented $\uparrow$ or $\downarrow$[2]. A system whose interaction cannot be satisfied simultaneously is considered frustrated. By progressively replacing more

[2]It is worthwhile mentioning that spin will eventually adopt an orientation, but the absence of a preferred direction creates degenerate ground states of equal energy (neglecting any kind of anysotropy). However, a degenerate ground state does not imply the existence of frustration

FM bonds, we introduce an increasing frustration into the lattice. The same effect could be achieved with all interactions being solely AF. Once a direction has been chosen for one spin, the following spins cannot establish a preferred direction, resulting in a 'frozen frustrated' state (MYDOSH, 1993).

This coupling game illustrates the fundamental behavior of spin glasses. Just as atoms in a glass are frozen in random positions, the spins in a spin glass become frozen in disordered, frustrated arrangements. A concise working definition describes spin glass

> [...] as a random, mixed-interacting, magnetic system characterized by a random, yet co-operative, freezing of spins at a well-defined temperature T_f below which a highly irreversible, metastable frozen state occurs without the usual long-range spatial magnetic order. [...] the term spin glass is used to generically represent the class of material exhibiting the frozen-state transition (MYDOSH, 1993, p. 3).

To clarify key terms in this definition: The term cooperative denotes systematic behavior that arises due to interactions among spins. Basically, magnetism can be categorized into two types based on coupling: non-cooperative systems, where spins act independently and remain unaffected by neighboring moments, and cooperative systems, where interactions between spins govern collective order (HURD, 1982). Finally, the phrase highly irreversible and metastable state describes that, below the critical temperature T_c, the spins become trapped in one of many possible configurations for extended periods. These configurations resist returning to prior states because of the energy barriers that separate them (this topic will be further examined in Section 2.4).

Building on these concepts, we have the essential ingredients for spin glasses: disorder (randomness), mixed interactions, and frustration. Without introducing a AF interaction in the triangular lattice, the system would adopt a purely ferromagnetic configuration. Introducing randomness in the bonds and their competitive nature induces frustration, a defining feature of the spin-glass ground state. This frustration prevents the system from settling into a simple ordered state, leading to a highly degenerate energy landscape with many nearly equivalent configurations.

Before diving deeper into the unique physics of spin glasses, let us briefly revisit some classical magnetic phases that arise in a homogeneous, disorder-free lattice. When all bonds are identical and either thermal agitation or uniform interaction dominates, the system can manifest, but not limited to, three canonical magnetic phases: paramagnetism, ferromagnetism,

or antiferromagnetism, each characterized by a distinct form of spin alignment and collective excitations. In the following subsection, we try to provide a concise definition of these concepts.

2.1.1 Paramagnetism, Ferro- and Antiferromagnetism

Before the pursuit of spin glasses, some magnetic phases were already well known. Some of the most common are the paramagnetism, ferromagnetism, and antiferromagnetism phases. We shall give a brief description of them, but before that, it is important to define two key properties of magnetic systems: magnetization $\boldsymbol{M}$ and magnetic susceptibility χ. Magnetization measures the extent to which a material becomes magnetized when exposed to an external magnetic field $\boldsymbol{H}$, reflecting the collective alignment of microscopic magnetic moments within the material. Magnetic susceptibility quantifies this response, indicating how easily the internal moments of a material realign under an applied field, typically expressed as $\chi = \partial M/\partial H$ (GUIMARÃES, 1998). These two properties enable us to characterize different magnetic phases.

Figure 3 – Illustration of a one-dimensional spin chain in (a) a paramagnetic phase, (b) a ferromagnetic phase, and (c) an antiferromagnetic phase.

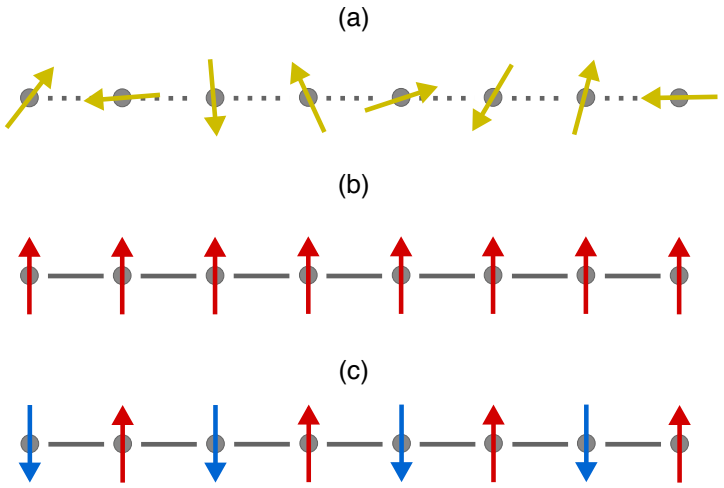

Source: The Author (2025)

Paramagnetism: As already mentioned, the paramagnetic state is a non-cooperative form of magnetism. This phenomenon emerges from individual magnetic moments that, under perfect conditions, are identical and exist in an isotropic environment sufficiently isolated to behave independently. The orientation of each spin is randomized by its thermal energy, resulting in no magnetic order in the system (HURD, 1982). However, when an

external magnetic field $\boldsymbol{H}$ is applied, the spins align partially with the field direction, the degree of alignment depending on the field strength. Paramagnetism is characterized by $\chi > 0$, where susceptibility varies inversely with temperature ($\chi \propto 1/T$). While increasing the magnetic field enhances spin alignment, raising the temperature disrupts it. Consequently, magnetization depends on the ratio H/T (BLUNDELL, 2001). The idealized paramagnetism posits that the spins are entirely independent. In reality, a weak exchange coupling between spins is often present. Below a critical temperature, cooperative magnetism emerges as these interactions overcome thermal energy. This behavior is captured by the Curie-Weiss law (HURD, 1982)

$$\chi = \frac{C}{T - \theta}, \ \forall \ T > \theta, \tag{2.1}$$

where C is the Currie constant and θ marks the onset of interaction dominance over thermal fluctuations, i.e., the temperature where occurs a phase transition. For practical purposes, we consider θ as a discrete temperature ($\theta = T_{\text{critical}}$).

Ferromagnetism : Ferromagnetism is a cooperative form of magnetism characterized by long-range collinear alignment of spins. It exhibits spontaneous magnetization even in the absence of an external field. This alignment arises from uniformly positive exchange interactions throughout the system ($J > 0$) (HURD, 1982). In ferromagnetic materials, the system divides into domains, each with uniform magnetization along a specific anisotropy axis. However, neighboring domains orient their magnetization in different directions. When an external field $\boldsymbol{H}$ is applied, the domains aligned favorably between $\mathbf{H}$ and the axial vector $\mathbf{D}$ (preferred spin-lattice direction) expand at the expense of others, although the magnitude of intrinsic magnetization within each domain remains largely unchanged. The field thus makes evident on a macroscopic scale the ordering that exists microscopically but does not alter the inherent magnetization strength within domains. Ferromagnetism is also characterized by $\chi > 0$. As the temperature increases, thermal energy disrupts the cooperative alignment. At Curie temperature T_C, spontaneous magnetization vanishes, and the system transitions to paramagnetism, obeying Eq. 2.1 for $T_{\text{critical}} = T_C$ (BLUNDELL, 2001).

Antiferromagnetism : Like ferromagnetism, antiferromagnetism is a cooperative form of magnetism characterized by long-range order among aligned moments. The key distinc-

tion lies in the negative exchange interaction ($J < 0$), which causes neighboring spins to orient in exactly opposite directions. This results in no net spontaneous magnetization. The antiferromagnetic state can be visualized as two interpenetrating ferromagnetic sublattices: one with magnetic moments aligned in one direction and the other in the opposite direction (BLUNDELL, 2001). The temperature at which thermal energy overcomes the exchange interaction is termed the Néel temperature (T_N). Above T_N, the system transitions to paramagnetism and obeys the Curie-Weiss law (Eq. 2.1).

Fig. 3 is a representation of a one-dimensional spin chain in one of these three classical magnetic phases. Having reviewed these foundational magnetic phases, we now return to spin glasses and examine how randomness plays a role in their behavior.

2.1.2 Disorder and Frustration

Disorder in spin glasses arises from the introduction of randomness into the system. This randomness can manifest itself as impurities or even topological defects. A prime example is found in magnetic alloys, which consist of magnetic impurities with localized spins randomly distributed within a non-magnetic host metal (MYDOSH, 1993). In fact, spin glasses were first discovered in such materials, for instance, in non-magnetic Au doped with Fe atoms (CANNELLA; MYDOSH, 1972). Canonical spin glass systems include alloys of the type $Au_{x-1}Fe_x$ or $Cu_{x-1}Mn_x$, where x represents the impurity concentration. Although magnetic alloys were the first systems observed to exhibit a spin glass transition, the phenomenon is not exclusive to them. It is also manifested in insulating hosts (MALETTA; FELSCH, 1979) and in amorphous materials formed by disrupting the crystalline lattice of intermetallic compounds (ZHOU; BAKKER, 1994). The examples cited above are classified as site disorder. However, merely introducing impurities into a system does not guarantee spin-glass behavior; the manner in which the disorder is introduced is vital. Systems generally exhibit two classes of disorder regarding the site: annealed and quenched. A way to differentiate them is to consider mixing impurities into a liquefied solid and gradually cooling it. An annealed disorder arises if the impurities and the host material maintain thermal equilibrium throughout cooling. In contrast, quenched disorder occurs when impurities remain static in random positions, never equilibrating with the host or the environment (CUGLIANDOLO, 2022). Spin glasses belong to the quenched disorder category (GROSS; MEZARD, 1984; WEISSMAN, 1993; DOTSENKO, 1995), where the randomness remains

perpetually fixed or unchanged.

It is important to emphasize that site disorder is not the only mechanism for generating spin glasses. A different mechanism was discussed in Section 2.1 through the coupling game, where the idea of bond disorder was introduced, although it was not properly named. In this scenario, magnetic interactions J alternate randomly between $+J$ and $-J$ (ferro- and antiferromagnetically) couplings across a geometrically ordered lattice. A good example of this is the compound $Rb_2Cu_{1-x}Co_xF_4$ (DEKKER; ARTS; WIJN, 1988), where Co and Cu atoms possess FM and AF interactions distributed arbitrarily across a 2D lattice. In addition, the triangular lattice symmetry in Fig. 2 prevents AF interactions from being mutually satisfied. Because of the triangle connectivity, starting at one corner and aligning each spin antiferromagnetically with its neighbor leads, upon returning to the initial site, to a spin orientation opposite to the starting one. Thus, a consistent AF alignment is impossible. Although this geometric constraint could subjectively be termed as a 'geometric disorder', it is insufficient to produce a spin glass state by itself. Fig. 4 illustrates the two essential types of disorder (site and bond) required to introduce the critical randomness characteristic of a spin glass.

Figure 4 – Illustrative representation of disorder in spin glasses via: (a) site disorder, where, for example, iron atoms (red dots) are randomly embedded in a copper lattice (green dots), each carrying a localized magnetic moment (spin) that interacts with neighboring iron spins but has its orientation frozen; (b) bond disorder, characterized by a roughly equal distribution of FM bonds (solid lines) and AF bonds (zigzag lines) randomly scattered across the lattice.

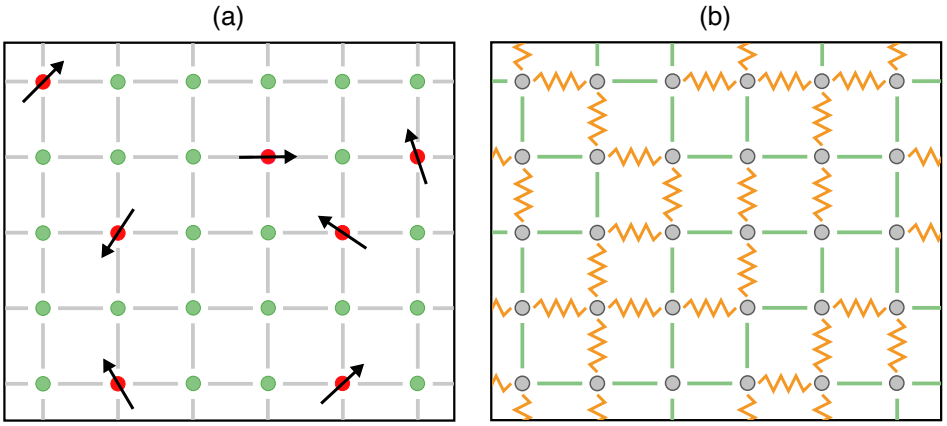

Source: Adapted from NOBELPRIZE.ORG (2021a) and MYDOSH (1993)

Disorder generates frustration: simultaneously fulfilling all the couplings is not possible. Analyzing an isolated triangle with AF interactions in Fig. 2, we identify some possible spin configurations. Frustration is an essential ingredient to establish how the ground state behaves.

Now consider a square lattice (cut from Fig. 4b) with spins at its corners: for the left panel (Fig. 5a), two $+J$ and two $-J$ bonds are present. Determining the initial spin configuration

Figure 5 – A square lattice with mixed FM ($+J$) and AF ($-J$) interactions exhibits distinct configurations: (a) unfrustrated, and (b) frustrated.

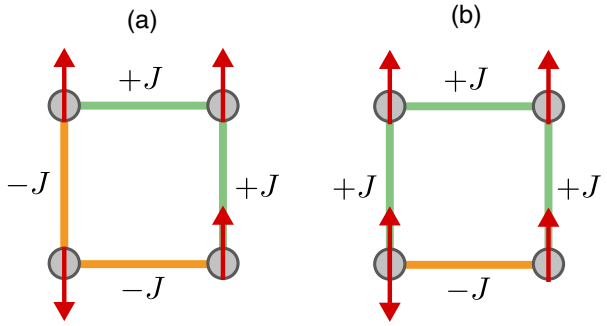

Source: Adapted from MYDOSH (1993)

at any corner fixes all other orientations, yielding a two-fold degenerate ground state. This configuration is unfrustrated. In contrast, the right panel (Fig. 5b) features three $+J$ and one $-J$ bonds, where no spin arrangement satisfies all interactions, resulting in frustration. The concept is very similar to the triangular lattice, but now without the geometric constraint. This analysis is formalized by assigning to each bond J_{ij} (interaction between spins i and j) a value ± 1. The system will be frustrated if (MEZARD; PARISI; VIRASORO, 1986)

$$\prod J_{mn} = -1. \tag{2.2}$$

For the case in Fig. 5, it is easy to see that the configuration assumes the value of $+1$ in the unfrustrated configuration and -1 in the frustrated case. In an extended lattice, there may be numerous frustrated bonds. Determining the optimal spin orientation to minimize energy is non-trivial, as frustration creates a multidegenerate, metastable, frozen ground state. Identifying the global minimum reduces to an optimization problem where the location of local minima becomes significant (PÁL, 1996; BOUNDS, 1987). Furthermore, frustration is not a tool to create spin glasses, but rather a consequence of disorder and competing interactions. Although frustration is a necessary condition for spin glass behavior, it is insufficient on its own (MYDOSH, 1993).

2.2 ONE LAST LOOK ON INTERACTIONS

We now briefly examine how interactions manifest in spin glass systems. The goal is not to provide an exhaustive description, but to list key interactions. A Hamiltonian formulation can describe the behavior of the spin glass. Disorder, as discussed in subsection 2.1.2, typi-

cally appears in the Hamiltonian as random couplings J among spins S. The first theoretical framework for the spin glass phase was proposed by Edwards and Anderson (1975), where they defined the spin glass Hamiltonian $\mathcal{H}$ as

$$\mathcal{H} = \sum_{\langle i,j \rangle} J_{ij}(\boldsymbol{S}_i \cdot \boldsymbol{S}_j). \tag{2.3}$$

In their model, the Heisenberg Hamiltonian was modified by replacing the constant coupling J with a variable J_{ij}, representing the interaction between spins S at the lattice sites i and j. Note that the spin can now assume any direction, rather than being limited to only the up or down configurations. The notation $\langle i, j \rangle$ under the summation restricts interactions to the nearest neighbors. First-neighbor coupling may arise via direct exchange, involving wave function overlap between sites and Coulomb electrostatic repulsion (EISBERG; RESNICK, 1985). This exchange effect originates from the Pauli exclusion principle, as detailed by Hurd (1982). However, due to the exponential decrease in the wave function with increasing distance from the nucleus, the resulting J_{ij} is too small to achieve the required next-neighbor coupling. Alternatively, indirect exchange mediates interactions over longer distances. In metallic alloys, conduction electrons propagate spin information between sites. This mechanism is typically modeled by the Ruderman–Kittel–Kasuya–Yosida (RKKY) interaction, which for sites i and j separated by distance r_{ij}, takes the form (JENSEN; MACKINTOSH, 1991)

$$J(r_{ij}) = \frac{12\pi\nu|j_0|^2\overline{\mathcal{N}}(\tilde{\epsilon}_F)}{(2k_F r_{ij})^4}[\sin(2k_F r_{ij}) - 2k_F r_{ij}\cos(2k_F r_{ij})], \tag{2.4}$$

where ν is the number of conduction electrons per atom, j_0 is the exchange constant, $\overline{\mathcal{N}}(\tilde{\epsilon}_F)$ is the average energy density of states at the Fermi energy level ϵ_F, and k_F is the Fermi momentum. Eq. 2.4 displays an oscillatory behavior of $J(r)$, where the interaction sign alternates with distance. Notice that for large r, $J(r) \propto r^{-3}$, which remains sufficiently long-range to influence multiple near neighbors. The RKKY interaction generates nearly symmetric numbers of $+$ and $-$ bonds across the lattice. This competition between the exchanges of FM and AF is a critical element for the behavior of the spin glass, as discussed in Section 2.1. Directly modeling the RKKY interaction is often a complex task. As an alternative, J_{ij} can be treated as a random variable governed by a probability distribution $P(J)$, typically Gaussian, which is identical for all spin pairs (MYDOSH, 1993; CASTELLANI; CAVAGNA, 2005).

$$P(J_{ij}) = \frac{1}{\sqrt{2\pi\Delta^2}} \exp\left[\frac{-(J_{ij} - J_0)^2}{2\Delta^2}\right], \tag{2.5}$$

where Δ is the variance and J_0 is the mean.

Another mechanism that causes spin interaction is the dipolar energy. Although generally weak, it can play an important role in causing spin glass behavior (VILLAIN, 1979; RANCOURT et al., 1990; CUERVO-REYES, 2016). It typically presents itself as (VUGMEISTER; GLINCHUK, 1990)

$$\mathcal{H}_{\text{dip}} = \sum_{ij} \frac{1}{r_{ij}^3}[\boldsymbol{\mu}_i \cdot \boldsymbol{\mu}_j - 3(\boldsymbol{\mu}_i \cdot \boldsymbol{n}_{ij})(\boldsymbol{\mu}_j \cdot \boldsymbol{n}_{ij})], \tag{2.6}$$

in which $\boldsymbol{\mu}$ is the magnetic dipole and $\boldsymbol{n}_{ij}$ is the vector pointing from the site i to the site j, $\boldsymbol{n}_{ij} = \boldsymbol{r}_{ij}/\|r_{ij}\|$. In several aspects, dipole interactions bear a similarity to RKKY interactions; competition between FM and AF interactions, and a $(1/r_{ij})^3$ factor. If the spins are oriented along $\boldsymbol{r}_{ij}$, they align parallelly. However, if they are perpendicular to $\boldsymbol{r}_{ij}$, they align antiparallelly (VILLAIN, 1979; MYDOSH, 1993). It can be seen from Eq. 2.5 that the lowest energy configuration is obtained when $\boldsymbol{\mu} \parallel \boldsymbol{n}_{ij}$. Interactions without dipolar coupling depends solely on distance r. Dipolar couplings introduce an angular dependence, linking to the final topic of this section: anisotropy.

By defining spins as Ising-type at the beginning of the chapter for the coupling game, we introduced one of the simplest forms of anisotropy in magnetic systems. The discrete spin orientations ($\uparrow$ or $\downarrow$) arise from strong uniaxial anisotropy along a preferred axis (usually named the z-axis). It is important to note that the Heisenberg model (Eq. 2.3) is isotropic, enabling spins to orient in any 3D direction without restriction, which includes non-collinear arrangements. Anisotropy plays a significant role in governing the frozen-in properties of spin glasses (MYDOSH, 1993). A preferred direction can emerge through multiple mechanisms. One is the dipolar interaction discussed earlier. Another source is single-ion anisotropy, produced by the local crystalline electrostatic field acting on magnetic ions. This field imposes preferential alignment directions for magnetic moments, typically aligned with the principal axes of the crystal lattice, resulting in magnetocrystalline anisotropy. The associated energy is expressed in spin-only Hamiltonian form as (HURD, 1982)

$$\mathcal{H}_{\text{SI}} = -\sum_i D(S_z)_i^2. \tag{2.7}$$

This expression is valid for uniaxial symmetry. Here, D is the axial crystal field constant, and S_z represents the total spin of the ion along the local z-axis. In amorphous materials, $D \rightarrow D_i$, where the local anisotropy D_i varies in magnitude and direction for every site i. Therefore, in these amorphous solids, there can be a random anisotropy characterized by a locally variable preferred axis (MYDOSH, 1993). Finally, we briefly address another anisotropy type in metallic spin glasses: the Dzyaloshinskii-Moriya interaction (DMI). This exchange interaction arises from spin-orbit coupling. The mechanism involves a conduction electron scattering off a spin $\boldsymbol{S}_i$, interacting with a nonmagnetic scatterer that exhibits strong spin-orbit coupling and subsequently scattering off another spin $\boldsymbol{S}_j$. This intermediate spin-orbit-mediated process underpins DMI anisotropy. The Hamiltonian is given by (MORIYA, 1960)

$$\mathcal{H}_{\text{DMI}} = \sum_{i<j} \boldsymbol{D}_{ij} \cdot (\boldsymbol{S}_i \times \boldsymbol{S}_j), \tag{2.8}$$

where $\boldsymbol{D}_{ij}$ is the Dzyaloshinskii-Moriya (DM) vector, determined by the crystal's symmetry and spin-orbit coupling strength. Eq. 2.8 is definitely antisymmetric. The sign of the cross product is reversed when S_i and S_j are interchanged. DMI favors the formation of a chiral spin structure, i.e., a configuration in which the spins have a preferred direction of rotation. Camley and Livesey (2023) provides a comprehensive explanation of how DMI influences magnetic and multiferroic materials.

In summary, the complex interactions coupled with inherent anisotropies in spin glass systems are key to understanding their unique, frustrated behavior, and rich dynamical phenomena.

2.3 DEALING WITH THE SPIN-GLASS PHASE

Now that the fundamental elements of the spin glass are well-established, we aim to solve its thermodynamic phase. Here, *solve* refers to computing the Helmholtz free energy $\mathcal{F}$, from which all thermodynamic properties of the system can be derived. Statistical mechanics provides the essential tools: once the Hamiltonian $\mathcal{H}$ is defined, we try to calculate the partition function $\mathcal{Z}$, defined as (KARDAR, 2007)

$$\mathcal{Z} = \sum_{\{\mu\}} \mathrm{e}^{-\beta \mathcal{H}(\mu)}, \tag{2.9}$$

where $\beta = (k_B T)^{-1}$, k_B is the Boltzmann constant, T is temperature, and the summation runs through all configurations of the system $\{\mu\}$. The free energy is then obtained via (KARDAR, 2007)

$$\mathcal{F} = -\frac{1}{\beta} \ln \mathcal{Z}. \tag{2.10}$$

At this stage, it is important to clarify that our goal is not to pursue exhaustive mathematical derivations of spin-glass theory. Instead, we aim to elucidate its foundational ideas, conceptual tricks, and methodological approaches, prioritizing qualitative understanding over quantitative rigor. A more detailed mathematical treatment can be found in the references cited throughout this section. One might construct a spin-glass Hamiltonian by synthesizing the elements established earlier: mixed interactions, spin-orbit coupling, etc. For example, combining the interactions discussed in Section 2.2 we can arrive at a slightly generalized spin-glass Hamiltonian:

$$\mathcal{H}_{\text{SG}} = \underbrace{\sum_{\langle i,j \rangle} J_{ij} (\boldsymbol{S}_i \cdot \boldsymbol{S}_j)}_{\text{Exchange Interaction}} + \underbrace{D \sum_i (S_z)_i^2}_{\substack{\text{Single-ion} \\ \text{anisotropy}}} + \underbrace{K \sum_{\langle i,j \rangle} (S_{ix} S_{jy} - S_{iy} S_{jx})}_{\text{DMI}} + \underbrace{g \mu_0 \mu_B \sum_i \mathbf{H} \cdot \boldsymbol{S}_i}_{\substack{\text{External} \\ \text{Magnetic Field}}} \tag{2.11}$$

In Eq. 2.11 we set $\boldsymbol{D}_{ij} = K\hat{z}$ and include an external magnetic field interaction, where g is the g-factor, μ_0 is the vacuum magnetic permeability and μ_B is the Bohr magneton. Although this Hamiltonian is highly complex and contains many of the elements necessary discussed for a spin glass, it is not the only formulation capable of generating this phase. An example of a different Hamiltonian is the p-spin spherical spin glass model, which, for N continuous spins S_i, is defined as (CRISANTI; SOMMERS, 1992):

$$\mathcal{H}_{pSG} = - \sum_{1 \leq i_1 < i_2 \ldots < i_p \leq N} J_{i_1 i_2 \ldots i_p} S_{i_1} S_{i_2} \ldots S_{i_p}, \tag{2.12}$$

where $p \geq 3$, and the couplings J_i follow a Gaussian distribution. Unlike Ising spins ($S_i = \pm 1$), this model incorporates spins as continuous real variables and constrains them by $\sum_{i=1}^{N} S_i^2 = N$. Although this system is less frustrated, it enables a more thorough analytical examination while the model continues to exhibit fascinating behavior (BARRAT, 1997). It is worth noting that spin-glass phases can emerge from a diverse class of Hamiltonian models. Regardless of the specific model, the presence of frustration and quenched disorder in these Hamiltonians consistently leads to a metastable energy landscape. The absence of a single ground state may

be related to a critical question: Is spin glass a distinct phase of matter, or is it simply a lethargic form of paramagnetism? To handle this, we can try to find evidence of a thermodynamic phase transition: an abrupt change in the magnetic and thermodynamic properties of the system. Cannella and Mydosh (1972), studying iron-gold alloys, observed, among other things, a sharp change in magnetic susceptibility χ below a certain critical temperature T_{SG}[3], suggesting a phase transition. We also would expect discontinuities in thermodynamic response functions (e.g., specific heat) for second-order transitions. However, experiments on spin glasses (MARTIN, 1979; GALAZKA; NAGATA; KEESOM, 1980; NAGATA et al., 1980) reveal no abrupt changes; instead, the specific heat exhibits a broad, continuous temperature dependence. Despite this discrepancy, theorists initially explored disordered systems using simplified, analytically tractable models to unravel spin glass thermodynamics. The Edwards-Anderson (EA) model (Eq. 2.3), as previously discussed, was among the first and simplest to describe spin glass behavior[4] (EDWARDS; ANDERSON, 1975). They used a Gaussian distribution (Eq. 2.5) with zero mean and unitary variance for the coupling parameter.

2.3.1 Order parameter and the replica trick

In order to characterize a phase transition, it is necessary to define an order parameter, which is a variable that quantifies the degree of order within a system phase. This order parameter assumes a nonzero value when below a critical temperature, while it becomes zero when above this temperature. In the context of a ferromagnetic system, the order parameter typically corresponds to the net average magnetization per spin, essentially representing the average spin value (NISHIMORI, 2001).

$$\langle M \rangle = m = \frac{1}{N} \sum_{i=1}^{N} \langle S_i \rangle. \tag{2.13}$$

While magnetization serves as the order parameter for ferromagnetism, antiferromagnetism lacks net magnetization due to equal populations of spins aligned in opposite directions. Instead, we use a sublattice magnetization (M_{sub}), as antiferromagnetism comprises two interpenetrating sublattices, as mentioned in subsection 2.1.1. Here, $M_{\text{sub}} \neq 0$ below the Néel temperature T_N. However, in spin glass systems, both M and M_{sub} vanish above and below

[3] T_{SG} : Spin glass critical temperature.

[4] This same Hamiltonian (with a slight modification in the coupling parameter J) can also capture conventional magnetic phases such as paramagnetism, ferromagnetism, and antiferromagnetism. It is usually refereed as the Ising Model, in honor of the german physicist Ernst Ising.

the critical temperature T_{SG}, which has no difference to the paramagnetic state. Due to the absence of long-range order, traditional parameters that emphasize spatial correlation are not applicable. Therefore, it is necessary to introduce a new order parameter. The EA model addresses this by focusing on temporal order. If a spin at a site i is frozen into a certain direction, there is a nonvanishing probability that it will point in the same direction a long time later (EDWARDS; ANDERSON, 1975). Therefore, we can define a correlation parameter as

$$q_{EA} = \lim_{t\to\infty} \frac{1}{N} \sum_i \overline{\langle \boldsymbol{S}_i(t_0) \cdot \boldsymbol{S}_i(t_0 + t) \rangle}. \tag{2.14}$$

The angular brackets $\langle \cdots \rangle$ denote a thermal (ensemble) averaging, while the overline $\overline{\cdots}$ represents a configurational average over all spins. A way to visualize q_{EA} is to imagine taking snapshots of the spin glass at widely separated times. If spins retain their orientations across snapshots (frozen disorder), $q_{EA} \neq 0$. If orientations fluctuate randomly (paramagnetic-like dynamics), $q_{EA} = 0$. Of course, $q_{EA} = 1$ at $T = 0$ and $q_{EA} \to 0$ as $T \to T_{SG}$ (MYDOSH, 1993).

Now that we have a way to determine whether the system is in the spin glass phase, we must address the Hamiltonian. The challenge is that, in principle, the system's free energy depends on the coupling constants J. This is problematic, as it implies that the physical properties of spin glasses vary for each distinct realization of the quenched disorder J. However, thermodynamics dictates that for sufficiently large systems, physical properties no longer depend on J. Quantities exhibiting this behavior are defined as self-averaging, with the free energy serving as a example (MEZARD; PARISI; VIRASORO, 1986). That is (CASTELLANI; CAVAGNA, 2005)

$$\lim_{N\to\infty} \mathcal{F}_N(\beta, J) = \mathcal{F}(\beta). \tag{2.15}$$

This is advantageous, as it allows us to analytically average over J, yielding results consistent with the observable's physical value. To perform this averaging for the free energy, we must compute

$$\overline{f_J} = \int dJ p(J) f(J) = \overline{f}, \tag{2.16}$$

where f is free energy density ($f = \mathcal{F}/N$) and $p(J)$ the coupling probability distribution. Utilizing Eq. 2.9 and 2.10, we obtain

$$\overline{f} = -\frac{1}{\beta N}\overline{\ln \mathcal{Z}},$$

$$\overline{f} = -\frac{1}{\beta N}\int dJp(J)\ln \int ds \mathrm{e}^{-\beta \mathcal{H}(s;J)}. \tag{2.17}$$

Computing Eq. 2.17 is not a simple task. Nevertheless, rather than computing the integral directly, we can calculate the average of the partition function raised to the power n, where n is an integer (MYDOSH, 1993)

$$\overline{\ln \mathcal{Z}} = \lim_{n\to 0} \frac{\overline{\mathcal{Z}^n} - 1}{n}. \tag{2.18}$$

This mathematical tool is known as the replica method (trick). What we do is prepare n replicas (snapshots) of the original system, evaluate the configurational average of the product of their partition functions, $\overline{\mathcal{Z}^n}$, and then take the limit $n \to 0$. This technique is useful because it is much easier to evaluate $\overline{\mathcal{Z}^n}$ than $\overline{\ln \mathcal{Z}}$. Utilizing the tools provided, the EA model has accounted for numerous aspects of the spin glass phenomena. The use of a temporal correlation parameter emerges as one of the most important factors, causing the freezing process to be trackable from a statistical mechanics perspective. However, the model does not account for everything. For example, the specific heat of $1/2$ spin systems disagrees with experimental results, except for the low-temperature linear dependence (FISCHER, 1975; MYDOSH, 1993), indicating that an improvement is necessary.

2.4 THE LONG-RANGE MODEL AND ITS APPROACHES

As an improvement to the EA model, David Sherrington and Scott Kirkpatrick proposed, in the same year, that a proper Mean Field Theory (MTF) for spin glasses should be an exact solution of an infinite-range EA model (SHERRINGTON; KIRKPATRICK, 1975). MTF is an approximation method used to simplify complex systems with many interacting components by replacing detailed interactions with an average (mean) effect. Instead of tracking how every part of the system influences every other part, each component is assumed to interact with an average field generated by all the others. This reduces a many-body problem to a more manageable single-body problem. The Sherrington-Kirkpatrick (SK) model proposes that every spin couples equally with every other spin, removing the nearest-neighbor approximation of the

EA model. This means that the probability distribution of J_{ij} is assumed, although unphysically, to be the same for all pairs (i, j), regardless of the distance between the spins (MYDOSH, 1993). They also included a mean $J_0 \neq 0$ to account for the possibility of ferromagnetism in the Gaussian function. The infinite-range interaction also needs the scaling of the variance and the mean by $1/\sqrt{N}$ and $1/N$ respectively, so that these are now intensive quantities (SHERRINGTON; KIRKPATRICK, 1975).

In their work, applying the same replica trick and after extensive mathematics, they arrive at a rather complicated expression for the partition function. Although we will not show it here, this expression depends on dummy variables x^{α} and $y^{\alpha\beta}$ associated with each distinct pair of replicas α and β (where $\alpha, \beta = 1, 2, \ldots, n$ and n is the number of replicas). The SK model treats all replicas as indistinguishable; a choice known as the replica-symmetric solution. The order parameter in Eq. 2.14 can now be written as

$$q_{\alpha\beta} = \frac{1}{N} \sum_i \overline{\langle S_i^{\alpha} S_i^{\beta} \rangle^2} = \frac{1}{N} \sum_i \overline{\langle S_i \rangle^2} = q, \tag{2.19}$$

with the addition of a ferromagnetic parameter

$$m_{\alpha} = \frac{1}{N} \sum_i \overline{\langle S_i^{\alpha} \rangle} = \frac{1}{N} \sum_i \overline{\langle S_i \rangle} = m. \tag{2.20}$$

If $q \neq 0$, this indicates that there is magnetic order; if, in addition, $m \neq 0$, the magnetic order is ferromagnetic. Therefore, the spin-glass state is characterized by $q \neq 0$ and $m = 0$ (SHERRINGTON; KIRKPATRICK, 1975). The SK model can construct a phase diagram that real spin-glass materials closely mimic and accurately describes certain susceptibility behaviors. Although it yields an exact solution, the model has a fundamental flaw: the entropy as $T \rightarrow 0$ approaches a negative value, clearly violating the third law of thermodynamics. Almeida and Thouless (1978) performed, a few years later, a detailed analysis of the SK model and demonstrated that the solution is unstable at low temperatures in both the spin-glass and paramagnetic phases. This instability comes from treating all replicas as indistinguishable ($\alpha = \beta$), an assumption that leads to invalid solutions of the mean-field EA model. The theoretical remedy is to seek a solution that breaks this replica symmetry.

2.4.1 Parisi's Replica Symmetry Breaking

Some attempts to break replica symmetry were made (BLANDIN, 1978; BRAY; MOORE, 1978), but the precise mechanism remained uncertain. The breakthrough came in 1979 with Giorgio Parisi (PARISI, 1979a; PARISI, 1979b), who solved the problem by proposing a hierarchical scheme of Replica Symmetry Breaking (RSB) , in which replicas are grouped into clusters, and these clusters are further subdivided in a recursive manner (PARISI, 1980; MÉZARD et al., 1984). In the glassy phase there is no unique locally stable thermodynamic state, but many states, where each replica corresponds to different solutions to the mean field equations. These solutions are in the N-dimensional configuration space of the N spins. This construction reflects the existence of a highly nontrivial energy landscape, characterized by a multitude of metastable states and a complex organization of pure states. Let us now turn to a more detailed, though not overly specific, treatment of the subject.

Figure 6 – Schematic representation of the spin glass multi-valley energy landscape acording to RSB

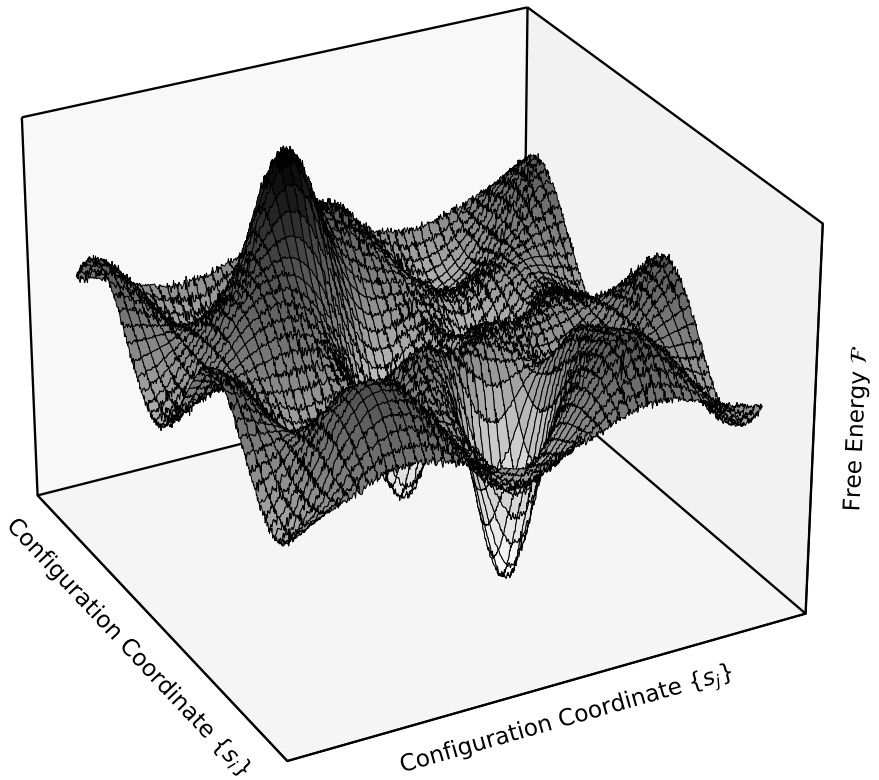

Source: The Author (2025)

During the freezing of a spin glass, the various spins can align their direction in many ways, such that it can settle into many configurations with nearly the same free energy. For $T < T_{SG}$ and in the thermodynamic limit $N \to \infty$, ergodicity of the configuration space can be broken. Although the system is in equilibrium, it no longer explores the entire phase space but is confined to particular sub-regions. Configurations that have the lowest free energy are pure equilibrium states, while those of higher free energy are metastable. Fig. 6 shows a qualitative representation of a two-dimensional slice of the multidimensional free-energy landscape, where the lowest-lying minima correspond to the pure states. How can we even characterize this ensemble of states? We can write the expectation of any observable s as a weighted probability sum over pure states (MEZARD; PARISI; VIRASORO, 1986)

$$\langle s \rangle = \sum_{\alpha} w_{\alpha} \langle s \rangle_{\alpha}, \tag{2.21}$$

where

$$w_{\alpha} = \frac{\mathcal{Z}_{\alpha}}{\mathcal{Z}} = \mathrm{e}^{-(\beta \mathcal{F}_{\alpha} - \beta \mathcal{F})}, \tag{2.22}$$

and $\mathcal{Z}_{\alpha}$ ($\mathcal{F}_{\alpha}$) is the partition function (free energy) of the state α. A defining element of pure states is the clustering property. This expresses the idea that the statistical correlation between two distant points vanishes as their separation tends to infinity.

$$\langle s_i s_j \rangle \longrightarrow \langle s_i \rangle \langle s_j \rangle \quad \text{for} \quad |i - j| \to \infty. \tag{2.23}$$

In other words, this reflects a form of physical locality: at large separations, the joint expectation value factorizes into the product of individual expectation values, indicating that distant regions no longer influence each other. Having established this, we turn our attention to another significant point. In finite-dimensional systems (without taking the thermodynamic limit), free-energy barriers around metastable states remain finite. Hence, the system cannot stay indefinitely in a metastable state; it will eventually escape and settle into a minimum. In Fig. 6, this corresponds to the system moving along high-energy paths until it falls into a valley and becomes confined there. Thus, if the system is initially located in a metastable state, it will inevitably transition to the stable state characterized by a lower free energy density. In contrast, in a mean-field (infinite-dimensional) model, these barriers can become infinite as

we apply $N \to \infty$, so that metastable configurations behave as pure states with well-defined weights w_α.

Now that we have our equilibrium states, we need a way to tell one state α from another β. To achieve this, we introduce a "distance" $d^2_{\alpha\beta}$ between them as the difference of their average spin square (MEZARD; PARISI; VIRASORO, 1986)

$$d^2_{\alpha\beta} = \frac{1}{N}\sum_i (\langle S_i\rangle_\alpha - \langle S_i\rangle_\beta)^2. \tag{2.24}$$

By expanding this expression, we arrive at the overlap parameter, which measures similarity between states, and is defined as

$$q_{\alpha\beta} = \frac{1}{N}\sum_i \langle S_i\rangle_\alpha \langle S_i\rangle_\beta. \tag{2.25}$$

This overlap is not the same as in Eq. 2.19. Here the EA parameter (q_{EA}) is only the overlap state with itself, i.e., $q_{EA} = q_{\alpha\alpha} = q_{\beta\beta}$, which does not depend on the state. Hence

$$d^2_{\alpha\beta} = 2(q_{EA} - q_{\alpha\beta}) \tag{2.26}$$

We now have a distance measure in state space and can tell how different two states are. Since at low temperatures, many nonequivalent pure states exist, we need to characterize its distribution. Let us define the probability distribution of overlaps between all pairs of pure states (MEZARD; PARISI; VIRASORO, 1986)

$$P(q) = \overline{P_J(q)} = \overline{\sum_{\alpha\beta} w^J_\alpha w^J_\beta \delta(q_{\alpha\beta} - q)}, \tag{2.27}$$

where the overbar denotes an average over realizations of the coupling J. The function $P(q)$ above captures the full landscape of pure states in the spin glass. Let us explain this.

The function $P(q)$ is not simply a statistical curiosity; it is the central order parameter of the spin glass phase in mean-field theory. As mentioned before, the defining trait of spin glass is the system becoming trapped in one of many pure states, each with its own microscopic configuration and macroscopic observables. However, since these pure states are not individually accessible experimentally, we must ask: What measurable or computable quantities can meaningfully capture this complex structure? Here, the overlap distribution $P(q)$ provides a complete description; it gives the probability of finding two states with overlap q,

weighting each pair by its probability of appearing in the ensemble ($w_\alpha w_\beta$). Only states for which the free-energy differences remain finite retain $w_\alpha > 0$, consequently contributing in Eq. 2.27. In the thermodynamic limit, all relevant states share the same free-energy density and therefore occur with equal probability[5] (MEZARD; PARISI; VIRASORO, 1986). We illustrate this concept with the simplest case: the ferromagnetic Ising model at zero field. For $T > T_c$, there is only one pure state (all spins uncorrelated), so every configuration is identical and $P(q) = \delta(q - q_{EA}) = \delta(0)$. For $T < T_C$, we have four possible overlaps:

$$\begin{aligned} q_{\uparrow\uparrow} &= \frac{1}{N}\sum_i \langle S_i\rangle_\uparrow^2 = \frac{1}{N}\sum_i m_i^2 = m^2, \\ q_{\downarrow\downarrow} &= \frac{1}{N}\sum_i \langle S_i\rangle_\downarrow^2 = \frac{1}{N}\sum_i m_i^2 = m^2, \\ q_{\uparrow\downarrow} = q_{\downarrow\uparrow} &= \frac{1}{N}\sum_i \langle S_i\rangle_\uparrow \langle S_i\rangle_\downarrow = -\frac{1}{N}\sum_i m_i m_i = -m^2. \end{aligned} \tag{2.28}$$

There are two pure states, so the function $P(q)$ has two delta functions, one at $q = m^2$, the other at $q = -m^2$. Note that the number of peaks in $P(q)$ is the number of distinct overlap values, not the number of states. For a spin glass, when the temperature is above the critical one, the probability distribution remains a single delta at $q = 0$ (paramagnetic phase). However, as T is lowered below T_{SG}, $P(q)$ acquires a non-trivial structure, often continuous with weight across an interval $[q_{\min}, q_{\max}]$ (typically, this range is $[0, 1]$). Fig. 7 illustrates these three different behaviors of $P(q)$.

$P(q)$ indicates this complex landscape with infinitely many pure states. Each value of q represents the similarity between two such states. The organization of pure states represented in the probability distribution has a profound hierarchical structure. This was one of Parisi's most striking insights: in the full RSB solution, pure states are not just numerous; they are organized in a nested, tree-like way. This means that for any three states α, β, and γ, their mutual overlaps satisfy the ultrametric[6] inequality (MYDOSH, 1993):

[5] In the thermodynamic limit, metastable states become irrelevant because their free-energy density is higher than that of equilibrium states, so they contribute negligibly to the partition function. Moreover, the free-energy barriers separating them scale with system size and diverge, making transitions between states effectively impossible.

[6] The concept of ultrametricity refers to a specific geometric structure in which, for any three points A, B, and C, their pairwise distances $d(x, y)$ satisfy the inequality

$$d(A, C) \leq \max\{d(A, B), d(B, C)\}.$$

This condition implies that the largest two distances among the three are always equal, forming isosceles (or equilateral) triangles in the space of states.

Figure 7 – The $P(q)$ function in (a) a ferromagnetic above Currie temperature; (b) at a temperature $T < T_C$; and (c) for a spin glass at way below the critical temperature. All cases have no magnetic field applied.

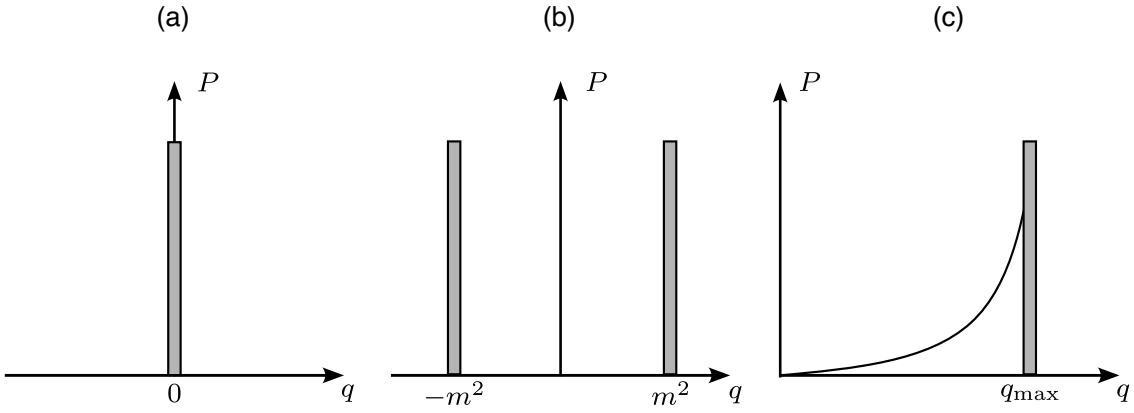

Source: Adapted from MEZARD; PARISI; VIRASORO (1986)

$$q_{\alpha\gamma} \geq \min\{q_{\alpha\beta}, q_{\beta\gamma}\}. \tag{2.29}$$

A way of visualizing is depicted in Fig. 8. End points represent states, while branches (circles) along with all their descendants signify clusters.

Figure 8 – Tree representation of the configuration clustering

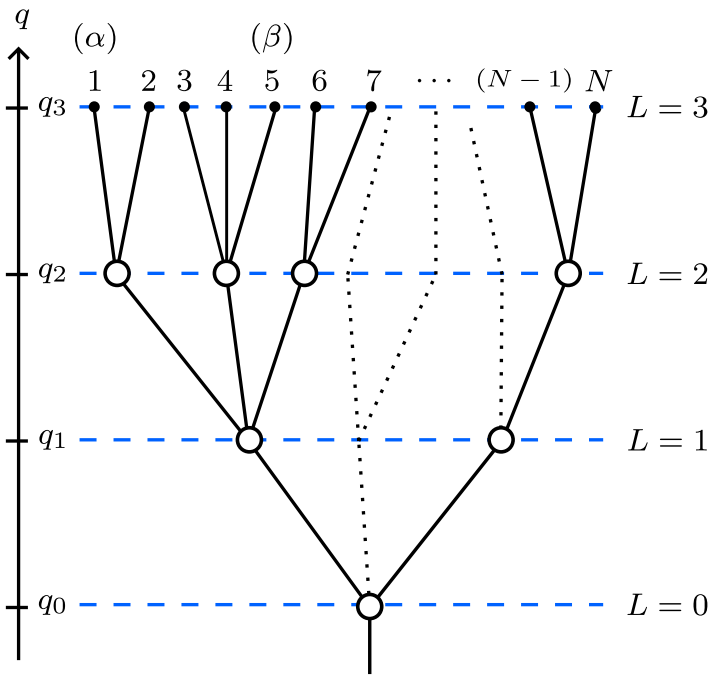

Source: The Author (2025)

To determine the overleap value $q_{\alpha\beta}$ between any two replicas (say $\alpha = 1$ and $\beta = 5$), we

backtrack them to their convergence point at the level $L = 1$, where the value is denoted as q_1. All the overlaps that lie in the same horizontal line are equal. For example, in Fig. 8, q_{12} and q_{34} have equal overlap with value q_2. However, replicas 1 and 3 have a different q value since they only join at a distinct level. Heating up the system would correspond to cutting the tree branches. The clusters of a low temperature regime now correspond to states of the system at high temperatures. There is an infinite number of ramifications at any temperature (keep in mind that we are considering the limit as $N \to \infty$), below the spin-glass transition (MÉZARD et al., 1984), depicted as dotted lines in Fig. 8. This means that at least the initial point of the tree has an infinite number of descendants. The overlap q values go towards one, which represents the replica overlap with itself. Another way to visualize the ultrametric structure is via the partition of the configurational space in Fig. 6, appearing as multiple valleys in the energy landscape. Each valley may split into smaller sub-valleys at lower energy scales, and this branching continues recursively.

To summarize, the overlap distribution $P(q)$ is the true order parameter of spin glasses, capturing the number, similarity, organization of pure states, etc. It connects abstract theory with measurable physical behavior in disordered systems. Crucially, RSB provides a consistent mean-field solution that fully solves the spin-glass phase and has proven broadly powerful, finding applications in fields as diverse as optimization, neural networks, and information theory (NOBELPRIZE.ORG, 2021a). With this, I believe we have covered the principal elements surrounding the spin glass phase and its theoretical foundations.

2.5 COMMENTS ON OTHER SPIN GLASS FRAMEWORKS

The RSB became by far the established framework for the infinite-range SK model, but alternative approaches exist for the spin glass problem. The Thouless-Anderson-Palmer (TAP) method provides an alternative route by directly constructing a free-energy functional (function of functions) of the local magnetizations $\{m_i\}$ (THOULESS; ANDERSON; PALMER, 1977), without relying on the replica trick. The solutions m_α derived from the TAP equations, when properly weighted, correspond to the fundamental pure states described by RSB theory, and they reveal a rich landscape of metastable states (MEZARD; PARISI; VIRASORO, 1986). Another approach is the cavity method. It revolves around a recursive procedure, where we analyze the properties of a system with N spins by examining how these properties change upon the addition or removal of a single spin, thus creating a ‘cavity‘. This perturbative scheme reproduces

TAP-like equations and highlights the same multiplicity of states.

For the short-range EA model, droplet theory (FISHER; HUSE, 1986) provides a scaling picture of low-temperature behavior based on ground-state excitations. Its central idea is that spin-glass properties are determined by their ground states. At low temperatures, low-energy excitations in a spin glass involve the flipping of one or more contiguous spins, forming connected domains known as "droplets" with length scale L and around a particular point x_j (MYDOSH, 1993). A fundamental prediction is that, in the thermodynamic limit and with zero external field, a spin glass has exactly two ground states (similar to Fig. 7b), related by global spin reversal: if $\{S_i\}$ is a ground state, then $\{-S_i\}$ is a ground state with the same energy. This contrasts sharply with RSB theory, which implies infinitely many distinct ground states.

3 FROM MAGNETIC DISORDER TO OPTICAL COMPLEXITY

Although numerous models have been proposed to describe the complex behavior of spin glasses, the RSB framework ultimately emerged as the central theoretical approach. For a long time, validation for RSB relied primarily on numerical methods, such as Monte Carlo simulations (BARAHONA, 1982; YOUNG, 1983; KATZGRABER; PALASSINI; YOUNG, 2001), which, while supportive, could not provide direct experimental confirmation. This changed with the advent of studies in the field of optics, particularly through investigations of random lasers and other disordered photonic media. These optical systems offered tangible, experimentally accessible platforms where the predictions of RSB theory could be directly tested.

To understand why optical systems were employed, let us use the following reasoning. Long before spin glasses emerged, it was well understood that conventional lasers admit a Hamiltonian formulation. Certain lasers incorporate structural disorder, named Random Laser (RL). So, this raises the question: Can we construct a disordered Hamiltonian for such systems? However, as noted in the previous sections, disorder by itself does not guarantee spin glass behavior. Thus, a sharper question is: Can photonic systems exhibit a counterpart to magnetic spin glasses? An affirmative answer came with Angelani et al. (2006a), which proposed a profound analogy between light propagation in disordered nonlinear media and glassy systems. Their work demonstrated that under a one-step replica-symmetry-breaking (1RSB) formalism[1], a solution with a nonzero overlap q emerges, and the system undergoes a true thermodynamic glass transition below a critical temperature. In this chapter, we will begin by reviewing the basic principles of RLs. Next, we will introduce the magnetic–photonic analogy and derive the key theoretical results that link multimode laser dynamics to spin-glass models. We then turn to the first experimental demonstration of replica symmetry breaking in a photonic system, showing how pulse-to-pulse intensity fluctuations serve as real replicas. Finally, we will define and discuss the order parameters that allow us to identify and characterize glassy phases in optical media.

[1] 1RSB involves dividing the n replicas into clusters of size m. Consequently, there are only two overlap parameters, q_0 and q_1.

3.1 CONVENTIONAL LASER VS. RANDOM LASER

Before describing a RL, we first define a laser. LASER is an acronym for Light Amplification by Stimulated Emission of Radiation, which concisely captures its operating principle. Lasers generate or amplify a narrow, coherent beam of light[2] with a well-defined wavelength in the electromagnetic spectrum (THOMAS; ISAACS, 2011). In laser action, atoms in the gain medium are excited by a pumping source, creating a population inversion that enables optical amplification[3]. The lasing process described above involves three essential components: the gain (lasing) medium, the pump (excitation) source, and the optical resonator, which are depicted in Fig. 9. Let us now give a simple description of them.

Figure 9 – Illustration of the essential elements of a laser, which mimics the original device developed by Theodore Maiman in 1960 (MAIMAN, 1960).

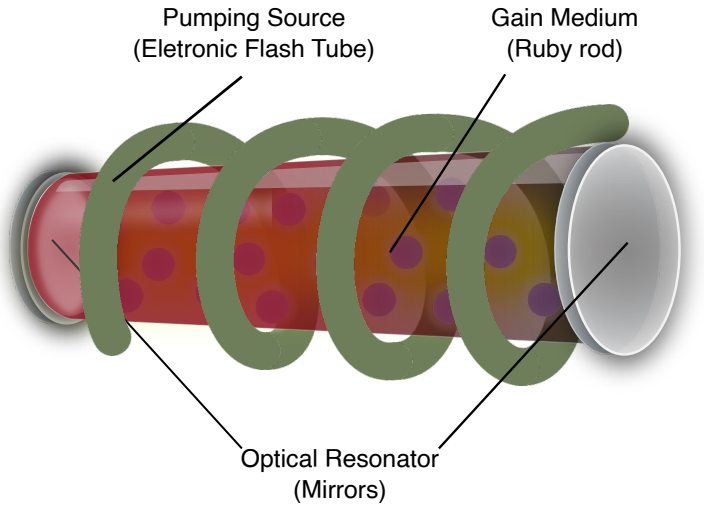

Source: Adapted from CARVALHO et al. (2024)

Gain medium : This is the material in which light amplification takes place, which may be a solid (glasses, crystals, or semiconductors), a liquid (typically dyes) or a gas (including mixtures). The medium has excitations that transition between energy levels when the atom absorbs or emits light. It is in the lasing medium that the principal processes of light emission can occur; absorption, spontaneous emission, and stimulated emission. Absorption happens when a ground-state system of energy level E_1 absorbs a photon

[2] Although "light" strictly refers only to the visible part of the electromagnetic spectrum, here we use it to mean all wavelengths indiscriminately.

[3] Amplification alone is insufficient for lasing; oscillation is also required, a condition fulfilled by the optical cavity (GOMES et al., 2021)

and transitions to a higher energy level E_2. The excited system tends to decay back to the ground state. If the energy difference of the levels is released as an electromagnetic wave spontaneously, it is emitted a photon of energy

$$h\nu = \Delta E = E_2 - E_1, \tag{3.1}$$

where h is the Planck constant and ν is the frequency of the emitted light. Stimulated emission arises when an excited state system is struck by a photon matching the energy in 3.1. This induces a transition $2 \rightarrow 1$, amplifying the incident optical wave.

All three processes coexist: an incident photon may be absorbed by a ground state electron or duplicated via stimulated emission. Absorption and stimulated emission are reciprocal processes with equal probabilities (THOMAS; ISAACS, 2011). For lasing, conditions must favor stimulated emission over absorption and spontaneous emission. This requires a population inversion, where more elements occupy excited states than ground states. Although outside the scope of this work, a complete description of these processes can be found in Svelto and Hanna (2013).

Pumping source : The pumping source delivers the energy needed to invert the population of the gain medium, alloying the amplification of the light. Pumping systems may be divided into three categories: optical (e.g., flashlamps, continuous-arc lamps, tungsten-filament lamps or other lasers), electrical (e.g., gas-discharge tubes or electric currents in semiconductors) and chemical (THOMAS; ISAACS, 2011).

Optical resonator (cavity) : In its basic form, it is composed of two mirrors positioned on opposite sides of the gain medium to form a resonant optical cavity[4]. One mirror is highly reflective, while the other, the output coupler, is partially transmissive. This arrangement results in optical feedback, where part of the coherent emission is reflected back into the cavity, enhancing stimulated emission. The optical cavity is designed to support specific resonant frequencies, also known as modes, which correspond to wavelengths of light that constructively interfere within the cavity. Only light that matches these resonant conditions is significantly amplified and is transmitted through the output coupler as an intense, coherent beam.

[4]This type of cavity is usually known as Fabry-Pérot resonator (FOX; LI, 1961)

Having reviewed the basics of a traditional laser, now we may ask: what distinguishes a RL from the conventional one? A RL is an optical device that achieves both amplification and feedback through multiple scattering within a disordered gain medium, rather than relying on a mirror-based cavity (WIERSMA, 2008). The concept was initially proposed by Letokhov (1967), yet the first evidence emerged years afterward (MARKUSHEV; ZOLIN; BRISKINA, 1986). Nonetheless, a significant advancement and definitive validation of the scheme were achieved in 1994 through the work of Lawandy et al. (1994), in which they documented laser emission in a highly scattering medium (TiO_2 nanoparticles on an organic dye suspension). The distinguishing feature of a RL from the conventional laser is the presence of scattering particles or inhomogeneities within the gain medium. As photons propagate through this medium, they undergo many random scattering events, which greatly extend their path length. This extended path length enhances the probability of photons interacting with excited atoms, leading to additional stimulated emission and amplification of light. Furthermore, some of the scattered light may eventually return to regions it has previously traversed, effectively providing feedback for the amplification process (NI et al., 2022). Figure 10 illustrates these random scattering paths occurring as light traverses the medium.

Figure 10 – Depiction of scattering in a RL system. Light penetrates a colloidal medium consisting of scattering particles embedded in a gain material. Multiple scattering events extend optical paths, raising the probability of stimulated emission.

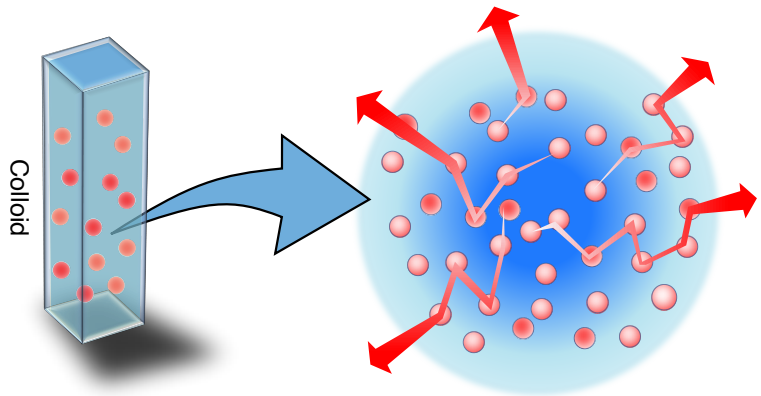

Source: Adapted from WIERSMA (2000)

Let us analyze the lasing process in more detail. An external pump (e.g., second harmonic of a Q-switched Nd:YAG laser) excites the gain medium, analogous to a traditional laser. The excited emitters decay spontaneously, emitting broadband fluorescence photons whose wavelengths reflect the energy-level structure of the gain material. These photons undergo repeated elastic scattering within the disordered matrix, effectively increasing their path length

in the gain region (ZIMNYAKOV et al., 2024). Though initially incoherent (with random phases and directions), these photons serve as a "seed" population for stimulated emission. When a seed photon interacts with an excited emitter of matching transition energy, it triggers the emission of an identical photon, causing exponential intensity growth. Modes within the random medium compete for the optical gain provided by the excited material. If spatially overlapping modes share the same region of the gain medium, lasing in one mode saturates the gain in that area, thereby reducing the available gain for competing modes (JIANG et al., 2004). This phenomenon, known as cross-saturation, leads to suppression or diminished intensity of certain modes, favoring those with higher effective gain or modes that achieve the lasing threshold more efficiently (WIERSMA, 2008). As pump intensity increases, both the number and output of modes rise, though modes with the longest lifetimes (lowest lasing thresholds) dominate in intensity. Lasing occurs when net optical gain exceeds intrinsic losses. At the threshold, the output intensity abruptly rises, and the emission spectrum narrows, producing either a single broad peak or sharp spectral spikes, depending on the feedback mechanism (SAPIENZA, 2022).

Optical feedback in a RL comes from the multiple scattering within the gain medium. Depending on the scattering strength, the RL is classified as incoherent or coherent (GOMES et al., 2021). In the weak scattering regime, incoherent feedback produces a single, broad emission peak. Alternatively, in the strong scattering regime, coherent feedback creates closed-loop photon trajectories through recurrent scattering, yielding resonant modes at discrete frequencies and multiple narrow spectral peaks (GOMES et al., 2021). The regimes can also be distinguished by the transport mean free path ℓ^*, which is the average distance before a photon's direction randomizes. For $\ell^* \gg \lambda$ (wavelength of the mode), the system operates in the non-resonant regime, where diffusive photon transport dominates, and interference effects are negligible. Conversely, $\ell^* \lesssim \lambda$ characterizes the resonant regime, where scattering is sufficiently strong to allow photons to retrace closed-loop paths, forming effective "cavities" where interference critically shapes lasing modes. RL typically exhibit low spatial coherence and broad angular emission. Their versatility stems from compatibility with diverse materials (e.g., powders, liquids, polymers, biological tissues, etc.), enabling simpler, cost-effective designs compared to conventional lasers. For an in-depth exploration of the theory and structure of the RLs, refer to the review articles by Wiersma (2008) and Gomes et al. (2021).

3.2 THE PHOTONIC SPIN GLASS

Now that we have a clearer picture of RLs, we can turn our attention to the phenomenon of RSB in optical systems. As discussed at the beginning of this section, Angelani et al. (2006a) demonstrated that light propagation in a random, nonlinear medium can exhibit glass-like behavior, analogous to that of magnetic spin glasses. Under rather general assumptions, they showed that the dynamics of a multimode RL can be mapped onto a disordered Hamiltonian for the phases of the modes. In their framework, the pumping rate $\mathcal{P}$ plays the role of the inverse of the temperature ($\mathcal{P} \propto 1/T$)[5], establishing a thermodynamic link. The complex amplitudes of the modes are assumed to vary slowly, allowing them to be treated as quenched variables (effectively fixed over the timescales of interest). Therefore, the relevant dynamical degrees of freedom are in the phases of the modes, which behave similarly to spins in a disordered magnetic system (ANGELANI et al., 2006a). This hypothesis is referred to as the quenched-amplitude approximation. Starting from coupled-mode equations that describe the evolution of these complex amplitudes in a disordered cavity, they were able to derive an effective "phase-only" φ Hamiltonian

$$\mathcal{H}(\varphi) = \mathcal{H}_0 + \sum_{s,p,q,r} G_{sqpr} \cos\left(\varphi_s + \varphi_p - \varphi_q - \varphi_r\right), \tag{3.2}$$

where

$$\mathcal{H}_0 = \sum_m (\gamma_m - \kappa_m) A_m^2, \tag{3.3}$$

and

$$G_{sqpr} = g_{spqr} A_s A_p A_q A_r. \tag{3.4}$$

Let us succinctly analyze the equations mentioned above. In Eq. 3.3, γ_m and κ_m represent the linear gain and loss coefficients for mode m, which possesses a fixed amplitude denoted as A_m. The amplitude relaxation time τ_A is much greater than the phase relaxation time τ_φ ($\tau_A \gg \tau_\varphi$), i.e., the amplitudes change so slowly relative to the much faster phase dynamics; this is known as the slow-amplitude approximation. This lets us separate the dynamics into

[5] future investigations will, in fact, connect to the reciprocal square root of the temperature ($\mathcal{P}^2 \propto 1/T$) (LEUZZI et al., 2009; ANTENUCCI et al., 2015)

"fast" phases and "slow" amplitudes and write each mode's complex amplitude as (ANGELANI et al., 2006a)

$$a_k(t) = A_k(t)\mathrm{e}^{i\varphi_k(t)}. \tag{3.5}$$

Under the quenched-amplitude approximation, we now put $A_k(t) \approx A_k$, so it can be treated as (quenched) constants. In this limit, $\mathcal{H}_0$ is just an overall constant offset that does not influence the phase dynamics directly (ANGELANI et al., 2006a). The subindices s, p, q, and r represent the lasing modes with a respective phase φ. The $\cos(\varphi_s + \varphi_p - \varphi_q - \varphi_r)$ term couples their phases in a four-body manner. The term g_{spqr} referenced in Eq. 3.4 serves as a coupling parameter. It is multiplied by the mode amplitudes A_i, thereby transferring the energy contained within each mode into the coupling process. Because the cavity is random and varies with each realization for a given pumping rate, these G_{sqpr} are quenched random variables. For this reason, is convenient to take G_{sqpr} as random Gaussian variables (Eq. 2.5) with zero mean value ($\langle G \rangle = 0$).

Applying the replica trick to compute the disorder-averaged free energy, they uncovered a 1 (one-step) RSB transition as the pump power increases. This approach revealed that, much like in traditional spin glasses, the phase space of the system fragments into many metastable states beyond a critical threshold, signaling the emergence of glassy behavior. Their results not only unveil the complex and rich dynamics of light in active disordered media, but also highlight the potential of such systems as experimental platforms for probing the RSB transitions (ANGELANI et al., 2006a). This study initiated a series of works by the Photonics Research Group at Università di Roma "La Sapienza" that extended theory to disordered, nonlinear multimode optical systems (ANGELANI et al., 2006b; LEUZZI et al., 2009; ANTENUCCI et al., 2015; ANTENUCCI; CRISANTI; LEUZZI, 2015a; ANTENUCCI; CRISANTI; LEUZZI, 2015b; ANTENUCCI, 2016; ANTENUCCI et al., 2016).

Although the magnetic–optics analogy was established in mid-2000, significant progress remained minimal at first. A key obstacle was that mode phases are not directly measurable, so no viable experiment could be performed. Significant progress only came with the first experimental observation of RSB in the pulse-to-pulse mode fluctuations of a RL (GHOFRANIHA et al., 2015) (more on Sec. 3.3). This breakthrough spurred a new theoretical framework that lifts the quenched-amplitude approximation by explicitly including mode amplitudes (ANTENUCCI et al., 2015). This advancement allowed the theory to describe regimes in multimodal lasers

across varying levels of pumping, disorder, and cavity leakage. Crucially, mode intensities could now fluctuate, saturate, and interact non-linearly, placing them on equal footing with phase dynamics. Consequently, the effective Hamiltonian transitioned from a purely "phase-only" cosine model to a complex-amplitude formulation:

$$\mathcal{H} = -\frac{1}{2}\sum_{jk} J^{(2)}_{jk} a_j a^*_k - \frac{1}{4!}\sum_{jklm} J^{(4)}_{jklm} a_j a^*_k a_l a^*_m, \tag{3.6}$$

where the amplitudes are subject to a spherical constraint (fixed total optical power)

$$\sum_k |a_k|^2 = \mathcal{E} = \text{cte.} \tag{3.7}$$

The terms $J^{(2)}_{jk}$ and $J^{(4)}_{jklm}$ represent quadratic and quartic coupling terms, respectively. The quadratic component describes linear interactions between modes, whereas the quartic component governs all-to-all nonlinear interactions[6]. This bears a direct analogy to the p-spin spherical model as expressed in Eq 2.12, with $p = 2 + 4$. Consequently, this is referred to as the spherical $2 + 4$ spin glass model (ANTENUCCI; CRISANTI; LEUZZI, 2015a). Eqs. 3.2 and 3.6 are equivalent. By substituting 3.5 into 3.6, relabeling indices, and appropriately redefining the coupling coefficients, one recovers the form of Eq. 3.2.

A significant achievement of this approach is the construction of a phase diagram based on the pumping rate and level of disorder for these photonic systems, as displayed in Fig. 11.

The phase diagram is inherently three-dimensional (Fig. 11 being a cut from this space), parameterized by degrees of nonlinearity α_0 and α (associated with the quartic coupling term), which span the interval $[0, 1]$. These parameters quantify the interplay between ordered and disordered parts of the Hamiltonian, effectively measuring how "closed" versus "open" the laser cavity behaves (ANTENUCCI; CRISANTI; LEUZZI, 2015a). In other words, α usually refers to how strongly the cavity dynamics are governed by nonlinear optical effects when compared to the linear response. When $\alpha_0 = \alpha = 1$, all mode-mode couplings are purely Hermitian (energy-conserving), corresponding to an ideal, lossless resonator. Conversely, at $\alpha_0 = \alpha = 0$, couplings become entirely dissipative (non-Hermitian), resembling a maximally open cavity where light escapes rapidly. Intermediate values smoothly interpolate between these extremes, governing the balance between coherent feedback and radiative loss.

The phase diagram's remaining parameters include the squared pump rate $\mathcal{P}^2$ and the disorder parameter R_J. As noted earlier, $\mathcal{P}^2$ serves as the inverse temperature. The disorder

[6]The Js remain characterized by random Gaussian distributions (ANTENUCCI et al., 2015).

Figure 11 – Phase diagram for a closed cavity ($\alpha = \alpha_0 = 1$), plotted versus disorder strength R_J (vertical axis) and effective pump parameter $\mathcal{P}^2$ (horizontal axis), showing four regimes (Continuous-Wave (CW), Phase Locking Wave (PLW), Random Laser (RL), Standard Mode-Locked (SML)) separated by threshold lines: dotted lines denote discontinuous transitions, while solid lines are continuous transition.

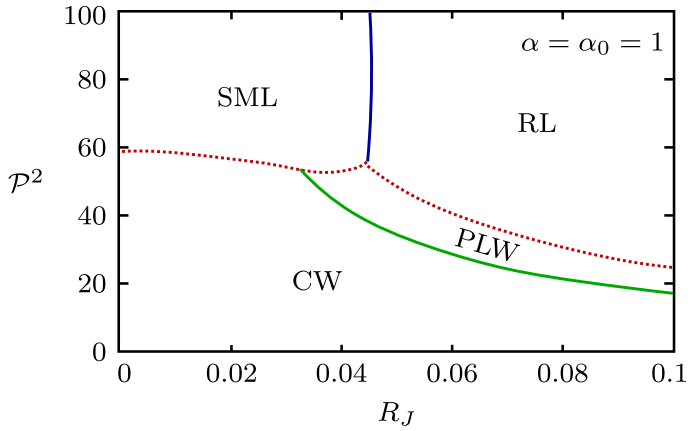

Source: Adapted from ANTENUCCI et al. (2015)

parameter R_J, which quantifies the relative strength of randomness in the quartic mode-mode couplings, is defined as the ratio of the standard deviation to the mean of these couplings,

$$R_J = \frac{J^{(4)}}{J_0^{(4)}}. \tag{3.8}$$

When $R_J = 0$, the system exhibits no disorder: all four-mode interactions share identical coupling strengths, resulting in a closed, perfectly periodic cavity. For $R_J > 0$, we introduce increasing amounts of quenched randomness in how different mode-quartets couple via Kerr nonlinearity. This increases the ruggedness of the energy landscape, fostering a glassy regime. One can change R_J by controlling the structural disorder of the gain medium or cavity. For instance, we can vary the scatterer concentration in a random laser, introduce deliberate refractive-index inhomogeneities, or adjust roughness in a photonic-crystal device. Greater disorder amplifies fluctuations $J^{(4)}$ relative to the mean coupling $J_0^{(4)}$, yielding a higher R_J.

Under the replica method, the phase behavior is characterized by three order parameters. The first is the global coherence

$$m = \frac{\sqrt{2}}{N} \sum_k \mathrm{Re}[a_k^\alpha], \tag{3.9}$$

with Re denoting the real part, since a_k is a complex amplitude of the mode k. This is analogous to magnetization in spin models (Eq. 2.20). The other two are the generalized overlap matrices

$$Q_{\alpha\beta} = \frac{1}{\mathcal{E}} \sum_{k=1}^{N} a_k^{\alpha} \left(a_k^{\beta}\right)^* \qquad\qquad R_{\alpha\beta} = \frac{1}{\mathcal{E}} \sum_{k=1}^{N} a_k^{\alpha} a_k^{\beta}, \tag{3.10}$$

These overlap matrices mirror the spin-glass overlaps of Eq. 2.25. When replica symmetry breaks, the elements of $Q_{\alpha\beta}$ and $R_{\alpha\beta}$ are no longer uniform and are instead described by probability distributions, indicating a complex, non-ergodic structure in the phase space. This signifies that identical copies of the system, subject to the same macroscopic conditions, can settle into distinct equilibrium amplitude configurations (ANTENUCCI et al., 2016). Varying $\mathcal{P}$, α, α_0, and R_J leads to four distinct photonic regimes in the resulting phase diagram:

- Continuous-Wave (CW): In this regime, the laser modes oscillate incoherently, resulting in the emission of a continuous, spatially unstructured wave. The energy is uniformly distributed across all passive modes, with no preferential direction or phase alignment. At low pump intensities, this is the sole solution. Regardless of the values of the disorder strength of R_J and nonlinearity α, the system settles into a replica-symmetric solution characterized by vanishing order parameters ($m = Q_{\alpha\beta} = R_{\alpha\beta} = 0$). This photonic phase is directly analogous to the paramagnetic phase in magnetic spin systems.

- Standard Mode-Locked (SML): This regime is characterized by a non-zero global coherence parameter ($m \neq 0$) and intensity sharing among activated modes, indicating that the modes oscillate coherently with a shared phase. The output light is emitted in the form of short, intense optical pulses, typical of mode-locking behavior. SML solutions can occur with or without replica symmetry breaking. This regime is the sole solution for high pumping rates ($\mathcal{P}^2$) in the absence of disorder ($R_J = 0$). Even with weak disorder, it persists at high pumping intensities. It is the photonic analog of the ferromagnetic phase in spin systems.

- Random Laser (RL): In this regime, modes lack intensity coherence ($m = 0$) but exhibit phase coherence ($R_{\alpha\beta} \neq 0$), with overlap matrices displaying nontrivial structure. It is the only phase for high pumping and large disorder. It corresponds to the spin-glass phase in spin models with disordered interactions.

- Phase Locking Wave (PLW): In this phase, the laser modes spontaneously lock their phases, so that $R_{\alpha\alpha}$ are the only nonzero terms ($m = Q_{\alpha\beta} = 0$). The intensities are uncondensed, i.e., the total optical energy in the cavity is still evenly spread across many

modes. Physically, this means you get a globally phase-coherent field but no net stimulated emission or pulsed mode-locking. In magnetic terms, the PLW phase corresponds to spins whose orientations are uniformly aligned while their magnitudes fluctuate. However, this does not represent any counterpart in spin models. PLW emerges as an intermediate regime between the CW and RL (or SML) phases. Moreover, increasing the nonlinearity parameter α shifts the onset of PLW to progressively lower pump intensities.

In summary, across these works, the authors achieved a full theoretical framework showing that multimode random lasers behave as optical analogs of mean-field spin glasses and, by progressively relaxing approximations, uncovered a hierarchy of novel photonic phases.

3.3 EXPERIMENTAL EVIDENCE OF RSB AND THE OVERLAP PARAMETER

Although Parisi solved the SK model in 1979 (PARISI, 1979b), more than thirty years elapsed before Ghofraniha et al. (2015) performed pulse-to-pulse measurements in an organic RL[7], providing the first direct experimental evidence of replica symmetry breaking in light; this milestone arrived nearly a decade after the magnetic–photonic analogy was first proposed (ANGELANI et al., 2006a).

In multimode RL, no single frequency dominates; shot-to-shot emission spectra fluctuate wildly, and their correlations are highly nontrivial (MOLEN; MOSK; LAGENDIJK, 2006; MUJUMDAR et al., 2007). These fluctuations reflect the presence of many degenerate lasing states, each defined by a specific set of activated modes with its own wavelengths, phases, and intensities. As the pump power crosses a critical threshold, this complex, glassy landscape emerges. Ghofraniha et al. (2015) measured the replica-overlap distribution $P(q)$ in a RL system and observed exactly the transition predicted by spin-glass theory. In their experiment, disorder remains fixed while increasing pump energy increases the effective nonlinearity. At low energy (high temperature), gain competition is negligible, so modes oscillate independently in a continuous-wave, paramagnetic regime. At high energy (low temperature), gain competition and disorder-induced frustration combine to produce a glassy regime. In this regime, numerous electromagnetic modes are simultaneously activated and interact; their configuration set changes from pulse to pulse, allowing each pulse's mode configuration to be treated as a distinct state. The observation of many different states under identical conditions provides ev-

[7] More specifically, a two-dimensional T_5OC_x amorphous solid-state RL

idence for a thermodynamic phase characterized by multiple valleys separated by free-energy barriers. Each emission event thus serves as a physical realization of a replica. To characterize the phase transition experimentally, it is necessary to introduce a new order parameter, which is defined by the overlap of intensity fluctuations between different replicas.

First, let us compute the average intensity $\langle I(k)\rangle$ of each mode (frequency) k over all replicas

$$\langle I(k)\rangle = \frac{1}{N_s}\sum_{\alpha=1}^{N_s} I_a(k), \tag{3.11}$$

where N_s is the total number of replicas. The intensity variation at a specific frequency represents a coarse-grained description of the behavior of individual modes,

$$\Delta_\alpha(k) = I_a(k) - \langle I(k)\rangle\,. \tag{3.12}$$

Finally, we define the overlap between two replicas α and β (pulse-to-pulse intensity fluctuations) as

$$q_{\alpha\beta} = \frac{\sum_{k=1}^{N}\Delta_\alpha(k)\Delta_\beta(k)}{\sqrt{\sum_{k=1}^{N}\Delta_\alpha^2(k)}\sqrt{\sum_{k=1}^{N}\Delta_\beta^2(k)}}. \tag{3.13}$$

The sum over k runs to the N^{th} frequency, determined by the spectral resolution. This overlap of intensity fluctuations, originally called the Intensity Fluctuation Overlap (IFO) (ANTENUCCI; CRISANTI; LEUZZI, 2015b), is defined on fluctuations rather than raw intensities in order to remove the effects of amplified spontaneous emission. The values of $q_{\alpha\beta}$ form a $N_s \times N_s$ symmetric matrix. Its diagonal entries $q_{\alpha\alpha}$ represent overlaps of each replica with itself. Since $q_{\alpha\beta} = q_{\beta\alpha}$ and self-overlaps are not counted, there are $\mathrm{C}_2^{N_s} = N_s(N_s-1)/2$ independent overlaps for each pump energy. Their distribution $P(q)$ provides a direct probe of the glassy phase. Ghofraniha et al. (2015) showed six such distributions, four of which are shown in Fig. 12.

At low pumping energies, the overlap distribution $P(q)$ exhibits a sharply defined peak at $q = 0$, as illustrated in Fig. 12a. This behavior indicates that the intensity fluctuations of each emission shot around the average spectrum are largely independent. This is analogous to how spins in a paramagnetic material fluctuate independently without interacting with each other. However, as the pump energy increases, mode intensities start to compete for gain and interact through nonlinear dynamics. This phenomenon is seen through the broadening of $P(q)$ (see

Figure 12 – Overlap distribution $P(q)$ illustrating replica-symmetry breaking as pump energy increases

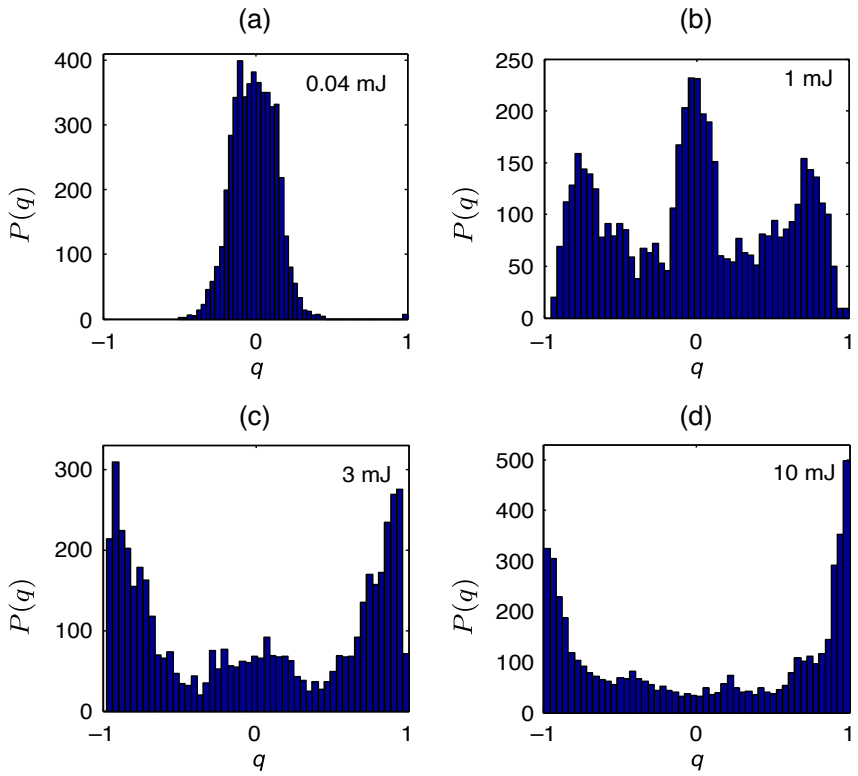

Source: Adapted from GHOFRANIHA et al. (2015)

Fig. 12b), with an increasing distribution moving away from zero overlap. In this intermediate regime, secondary peaks emerge, indicating the initiation of correlated fluctuations among certain mode subsets.

In the high-energy "glassy" phase, evident above the threshold (see Fig. 12c-d), the system exhibits strong nonlinear coupling and the disorder obstructs global coherence. Consequently, $P(q)$ transforms into a wide-ranging, continuous function over the interval $[-1, 1]$. Here, an overlap $q \approx 1$ indicates that the fluctuation patterns of two shots are very similar across all wavelengths, regardless of their absolute amplitudes. In contrast, $q \approx -1$ signifies that the fluctuations are of the same magnitude but have opposite signs, with peaks in one shot aligning with decreases in another. The emergence of substantial positive and negative overlaps only after crossing the threshold is a significant indication of the numerous metastable lasing states; each pulse corresponds to one such state. The complete form of $P(q)$ reveals the intricate free-energy landscape of the system.

To monitor the evolution of $P(q)$ as a function of pump energy, one often plots the magnitude of its peak overlap, $|q_{\mathsf{max}}|$, versus the input energy (Fig. 13). In the terminology of spin

glasses, $|q_{\max}|$ corresponds to the EA order parameter q_{EA} (Eq. 2.14) (PARISI, 1979a). As the energy input increases, the value of $|q_{\max}|$ stays close to zero within the prelasing, paramagnetic phase, but then it sharply increases at the lasing threshold, indicating the transition to the glassy RL state.

Figure 13 – Absolute value of $|q_{\max}|$ (the position of the peak of $P(|q|)$) plotted as a function of pumping energy. The paramagnetic-glass transition occurs between 2 and 3 mJ

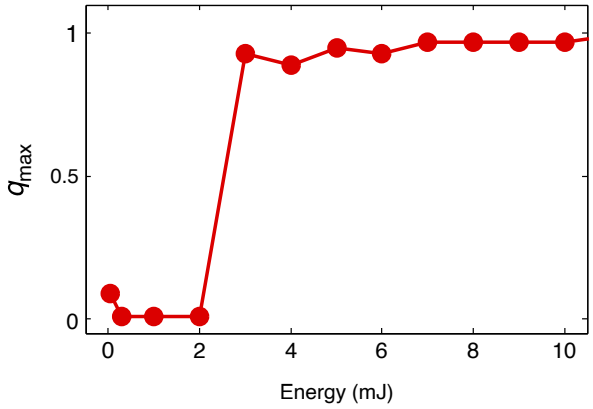

Source: GHOFRANIHA et al. (2015)

One might naturally ask: why not use the order parameters from Eq. 3.9 and Eq. 3.10 to determine the spin glass transition instead of introducing a new overlap? The reason is that parameters such as $Q_{\alpha\beta}$ and $R_{\alpha\beta}$ depend on the complex amplitudes a_k^α, specifically their phases $\phi_k = \arg(a_k)$. In disordered systems, the magnitudes $|a_k|$ are easily accessible experimentally, whereas extracting the corresponding phase information is considerably more challenging. As a result, reconstructing the distributions in Eqs. 3.9 and 3.10 is impractical.

After the first experimental indications of RSB, Antenucci, Crisanti and Leuzzi (2015b) provided an analytical basis for the intensity-based order parameter in the RSB context. They considered shot-to-shot intensity spectra from each shot as real replicas, with intensity fluctuations being the only observable variables. By omitting the normalization factor $\sqrt{\sum_k \Delta_\alpha^2(k)}$ relative to the fluctuations $\Delta_\alpha(k)$, they formulated the IFO within the framework of the $2+4$ complex-amplitude spin-glass model as

$$q_{\alpha\beta} \equiv \mathcal{C}_{\alpha\beta} = \frac{N}{8\mathcal{E}^2} \sum_{k=1}^{N} \left[\left\langle |a_k^\alpha|^2 \left| a_k^\beta \right|^2 \right\rangle - \left\langle |a_k^\alpha|^2 \right\rangle \left\langle \left| a_k^\beta \right|^2 \right\rangle \right]. \tag{3.14}$$

Equation3.14 reproduces the IFO up to an overall sign. In fact, the form given in the above equation, originally defined for $\mathcal{C} \in [0,1]$, remains valid if one interprets $P(q_{\alpha\beta} = \mathcal{C}) \longleftrightarrow$

$P(\mathcal{C}_{\alpha\beta} = |\mathcal{C}|)$. To match experiments, they worked with the symmetrized overlap distribution $P(\mathcal{C})$ for $\mathcal{C} \in [-1, 1]$, which retains all relevant information without loss of generality.

It is also possible to relate the IFO to the standard overlap parameters (ANTENUCCI; CRISANTI; LEUZZI, 2015b):

$$\mathcal{C}_{\alpha\beta} = Q_{\alpha\beta}^2 - \frac{m^4}{4}, \quad \forall \quad \alpha \neq \beta. \tag{3.15}$$

This equation offers a rigorous experimental probe of RSB: whenever $Q_{\alpha\beta}$ exhibits replica breaking, the IFO follows the same pattern. The theory further predicts that, as the system crosses the lasing threshold, the photonic overlap distribution will show a discontinuous jump in closed cavities but will evolve continuously in open cavities. A construction of a phase diagram and numerical simulation confirms these contrasting behaviors, demonstrating quantitative agreement between theory and experiment.

Before wrapping up the chapter, let us examine one important point. It can be asserted that the IFO primarily acts as a correlation parameter. The IFO measures the normalized correlation between the intensity-fluctuation vectors of two distinct replicas (shots), α and β, effectively assessing how similar their overall spectra are. From this viewpoint, it is natural to imagine an alternative perspective: instead of focusing on the similarity between replicas, one could analyze the similarity among different mode frequencies within the intensity spectrum. Given a series of N_s measurements (replicas) of the intensity pairs $\{I(i), I(j)\}$, where $i, j \in [1, 2, \ldots, N]$ (with N being total number of sampled points in the spectrum)[8], the Pearson Correlation Coefficient (PCC) ρ_{ij} is defined as (CORONEL et al., 2021)

$$\rho_{ij} = \frac{\sum_{\alpha=1}^{N_s} \left[I_\alpha(i) - \langle I(i)\rangle\right] \left[I_\alpha(j) - \langle I(j)\rangle\right]}{\sqrt{\sum_{\alpha=1}^{N_s} \left[I_\alpha(i) - \langle I(i)\rangle\right]^2 \sum_{\alpha=1}^{N_s} \left[I_\alpha(j) - \langle I(j)\rangle\right]^2}}, \tag{3.16}$$

The PCC measures the extent of normalized linear correlation amongst the intensity variations between two distinct frequencies, i and j across multiple shots. A value close to 1 indicates a strong positive correlation of fluctuations for modes i and j, whereas a value near -1 signifies considerable anticorrelation. Conversely, a value approaching 0 implies that the two frequencies are statistically independent. Thus, when spatially overlapped coupled

[8] the indices i and j label two distinct spectral positions (i.e., frequencies). In practice, each index corresponds to one point of the measured spectrum, and the spacing between consecutive indices is set by the optical resolution of the apparatus. Thus, the pair (i, j) refers to the intensities recorded simultaneously at two different frequencies within the same spectrum.

modes occur, they can either share gain, compete for it, or operate independently along the measurements, contingent upon the specific value of ρ_{ij}.

Both the IFO and the PCC are Pearson-style measures: $q_{\alpha\beta}$ sums over frequencies for each pair of shots, while ρ_{ij} sums over shots for each pair of frequencies. Coronel et al. (2021) proposed a unified parameter that captures both shot-to-shot and mode-to-mode correlations simultaneously. To develop this measurement, it is essential to consider the various potential frequencies and indices of summation within Eq. 3.13. Let $I_{\gamma i}$ be the intensity at the frequency ω_i in the spectrum γ. Let us also define $\langle I_i \rangle$ as averaged intensity at the frequency ω_i over all the spectra. Consequently, we can express a revised relative difference average (Eq. 3.12) as

$$\overline{\Delta_{\gamma i}} = \frac{\Delta_{\gamma i}}{\sqrt{\sum_K \left(\Delta_{\gamma i}\right)^2}}, \quad \Delta_{\gamma i} = I_{\gamma i} - \langle I_i \rangle \,. \tag{3.17}$$

Here, Greek indices label replicas (e.g., γ, α), lowercase Latin indices label frequencies (e.g.,i, j). and uppercase Latin letters can denote either a replica or a frequency (e.g., $K = \gamma$ or $K = i$). Note that K does not appear as a label or parameter on the left-hand side of the equation, because it will ultimately assume one of the indices already present in the expression. Observe that in Eqs. 3.11 and Eqs. 3.12, the frequencies are now denoted as subscripts. The unified parameter, called the Photonic Overlap Parameter (POP) in this work, is then defined as

$$P_{MN} = \sum_K \overline{\Delta_{MK}\Delta_{NK}}, \tag{3.18}$$

The advantage of the POP lies in its unification of both IFO and PCC. By assigning spectrum indices $M = \alpha$, $N = \beta$, and frequency $K = i$, we recover Eq. 3.13. Conversely, setting frequency indices $M = i$, $N = j$, and spectrum index $K = \alpha$, we obtain Eq. 3.16.

In summary, pulse-to-pulse overlap measurements in RL have confirmed that light can undergo a genuine RSB transition, evolving from an uncorrelated, paramagnetic regime to a complex, glassy phase with a broad overlap distribution. The unified POP offers us a direct link between spin-glass theory and photonic experiments, providing a readily accessible test of glassy properties in continuous media without fixed-magnitude constraints.

4 ANALYSIS ON A MODE-LOCKED FIBER LASER

Over the following decade, experimental studies of RSB proliferated across a wide range of optical platforms. RSB was observed in random lasers (GOMES et al., 2016b; PINCHEIRA et al., 2016; BASAK; BLANCO; LÓPEZ, 2016; CORONEL et al., 2022b; CÂMARA et al., 2022; NIDEESH et al., 2024), in random fiber lasers (GOMES et al., 2016a; LIMA et al., 2017; CORONEL et al., 2021; QI et al., 2024), and in Q-switching lasers (MOURA et al., 2017; CORONEL et al., 2022a). Other demonstrations came from waveguide systems (PIERANGELI et al., 2017), mode-locked fiber lasers (ALVES et al., 2024), and numerical simulations of random lasers (PALACIOS et al., 2023). More recently, analogues of quantum spin glasses have been investigated (MARSH et al., 2024), and glassy behavior was reported in multifilamentation (SIQUEIRA et al., 2025) and soliton-fission dynamics (PALACIOS et al., 2025).

In this chapter (and the subsequent ones), our primary focus will be the Mode-locked Fiber Laser (MLFL) described in (ALVES et al., 2024), which represents a first result of this dissertation. Here, we introduce the SML regime and its core principles. We then delve into the emergence of a glassy phase that precedes SML and is defined by RSB. Finally, we analyze the statistical properties of the intensity fluctuations within this glassy phase and elaborate on their physical significance.

4.1 THE MODE-LOCKED FIBER LASER

Describing the full phenomenology of a MLFL would require extensive chapters and sections. A more effective strategy involves focusing specifically on our experiment, allowing us to elaborate on its principles without diverting into unrelated subjects. Our setup is a unidirectional ring fiber laser that includes Ytterbium-doped fiber pumped at 976 nm, polarization controllers, an optical isolator, fiber Bragg gratings, and an output coupler (see experimental desciption on Section 6.1). This section aims to present the essential principles associated with this specific type of laser and to provide a succinct description of it. Similar to the earlier chapters, the intention is not to be comprehensive, but rather to communicate the central concepts pertinent to the topic.

4.1.1 The Ytterbium Fiber Laser

Within the broader family of laser technologies, fiber lasers constitute a significant category. Their defining feature is the use of an optical fiber as the active gain medium, a concept first proposed in the 1960s (SNITZER, 1961). Typically, the fiber is doped with rare earth ions such as erbium (Er^{3+}), neodymium (Nd^{3+}), or ytterbium (Yb^{3+}). Yb^{3+} ions in silica matrices offer an ideal gain medium for fiber lasers, as they present a simplified spectroscopic system with only two main levels ($^2F_{7/2}$ and $^2F_{5/2}$) (PASCHOTTA et al., 1997), each subdivided into multiple sublevels; this minimizes excited-state absorption losses and enables high population inversion rates. Ytterbium-doped fibers commonly emit around 1 μm (PASK et al., 1995), and are widely used in various fields, including metrology, spectroscopy, and quantum optics.

When pumped at a specific wavelength, rare-earth ions absorb energy and emit light at a longer wavelength via stimulated emission, achieving optical amplification. The pumping source is usually a semiconductor laser diode tuned to a wavelength efficiently absorbed by the ions[1]. For Yb^{3+} in germanosilicate fibers, absorption peaks near 975 nm and emission centers around 1030 nm, allowing narrow-linewidth 976 nm pumping to populate up to 50% of the metastable level (PASCHOTTA et al., 1997). Pumping light is coupled into the fiber via a dichroic fiber coupler, which transmits the pumping wavelength into the active fiber while enabling laser light at the emission wavelength to circulate within the cavity. In a fiber laser, the resonator can adopt either a linear or ring configuration. A linear cavity employs two reflective elements, such as optical mirrors or fiber Bragg gratings, positioned at each end of the active fiber. Amplified light reflects between, for example, mirrors, traversing the gain medium on each round trip. Conversely, a ring cavity (which is our case) forms a closed loop by "connecting"[2] the fiber ends, enabling continuous light circulation through the active fiber and other cavity components.

Fiber lasers are particularly good at producing ultrashort pulses, such as those on the picosecond or femtosecond scale, owing to their extensive gain bandwidth, high efficiency, and affordability (FERMANN; HARTL, 2013). Nevertheless, their efficacy within this domain is frequently limited by significant fiber nonlinearities, which can affect aspects like pulse energy, peak power, and overall pulse quality (ZERVAS; CODEMARD, 2014).

[1] This choice depends on the ions' absorption cross-sections (PASCHOTTA et al., 1997).

[2] In this context, "Connect" signifies that the light emitted from the fiber re-enters the fiber without necessitating a physical junction. The light is capable of traveling through free space before it re-enters the fiber.

4.1.2 The mode-locking process

In a SML laser, ultrashort light pulses are produced by synchronizing the phase relationships of the longitudinal cavity modes, compelling them to oscillate in unison[3] (HAUS, 2000). This differs significantly from conventional lasers, in which modes generally oscillate independently with phases that are random and uncorrelated. Achieving phase-synchronized oscillation of longitudinal modes results in the superposition of modes, creating a short pulse within the resonator. Each time this pulse interacts with the output coupler, it results in a pulse exiting the laser, producing a consistent sequence of ultrashort pulses. Although "mode locking" refers to the frequency domain, its underlying mechanism is more intuitive in the time domain. Fig. 14 provides a depiction of this process. When resonator modes (left panel) share a fixed phase relationship, their superposed fields interfere constructively at specific instants, producing a high-intensity light pulse (top-right plot). Between pulses, out-of-phase modes interfere destructively, yielding periods of zero intensity. In the presence of arbitrary relative phases, the evolution of the intracavity field becomes indeterminate (bottom-right plot).

Figure 14 – Comparison of phase-matched and random-phase mode oscillations for a different frequencies set. In the left panel, each mode is vertically displaced by a constant amount for clarity. In the top-right panel, all modes share a common phase, so their constructive interference produces well-defined pulses at a fixed rate. In the bottom-right panel, the mode phases are random, so interference is irregular and no distinct pulses emerge.

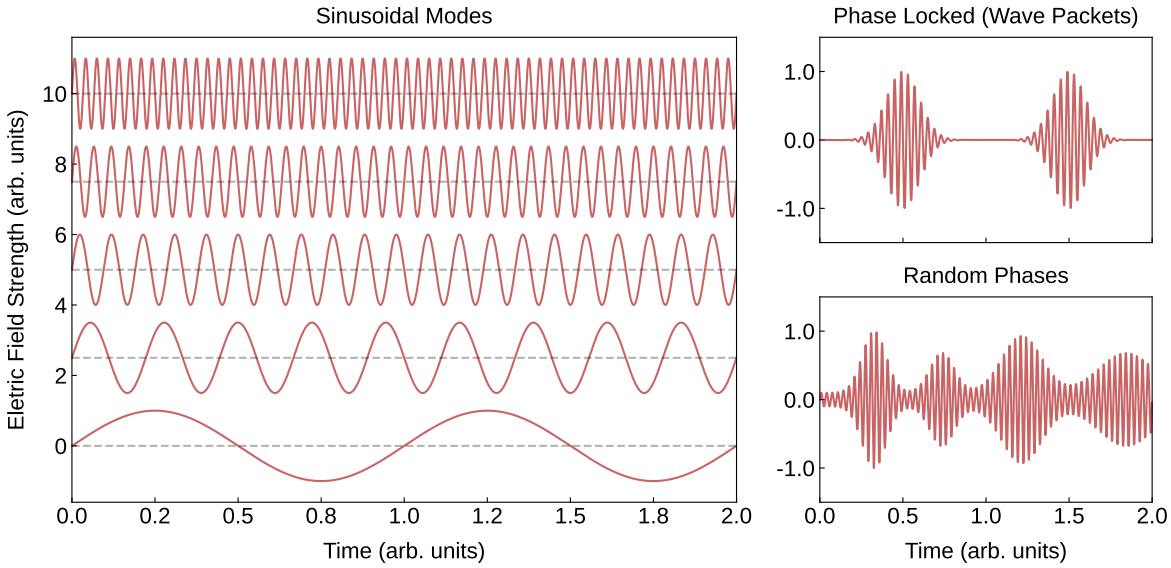

Source: The Author (2025)

[3] The concept of mode locking was introduced in the 1960s (LAMB, 1964), with the first active mode-locking demonstration following just weeks after (HARGROVE; FORK; POLLACK, 1964).

A crucial relationship links pulse duration to the number of phase-locked longitudinal modes: achieving shorter pulses requires synchronizing a broader range of resonant frequencies. If N modes separated by $\Delta\nu$ are phase-locked, the total SML bandwidth is $N\Delta\nu$, and a broader bandwidth produces a shorter pulse. In reality, the pulse duration also depends on the exact amplitude and phase relationships among the modes, i.e., the shape of the pulse. For a Gaussian-shaped pulse, the time-bandwidth product is (WEINER, 2011)

$$\Delta t\Delta\nu = \frac{2\ln 2}{\pi} \approx 0.441. \tag{4.1}$$

[4]So, the minimum pulse duration is

$$\Delta t = \frac{0.441}{N\Delta\nu}. \tag{4.2}$$

Here, Δt denotes the intensity Full Width at Half Maximum (FWHM), and the bandwidth $\Delta\nu$ is measured as the FWHM of the positive-frequency portion of the power spectrum. Both elements focus only on the central part of the pulse or its spectrum, respectively.

The fundamental principle of all lasers is that the gain must exceed cavity losses. However, generating ultrashort pulses requires an additional element: a mode locker. This component enforces the SML regime (WEINER, 2011). SML can be implemented via two main techniques: passive mode locking and active mode locking. Active mode locking involves the use of an external driving signal to periodically alter the characteristics of the light inside the laser cavity, typically affecting the amplitude or phase. In fiber lasers, the main active mode lockers are acoustic-optic modulators and electro-optic modulators. These devices are situated within the cavity of the laser and are activated by an electrical signal with a frequency that is exactly tuned to either the longitudinal mode spacing of the cavity or one of its harmonics (PASCHOTTA, 2006). Passive mode lockers, on the other hand, use intra-cavity elements whose transmission or reflection depends on the instantaneous light intensity. A Saturable Absorber (SA) is the most common example: its absorption decreases as incident intensity rises (WEINER, 2011). At low intensity the SA introduces loss, but when a pulse peak passes through, the absorber saturates and becomes more transparent. This preferential transmission of high-intensity fluctuations initiates and shortens pulses. Passive mode-locking is capable of generating shorter pulses by synchronizing loss modulation with the laser pulses (IPPEN; SHANK; DIENES, 1972). Semiconductor saturable-absorber mirrors (SESAMs) are an example of passive mode-locking

[4]In the case of a sech^2 pulse, the time-bandwidth product is approximately 0.315.

devices (KELLER et al., 1996). Other SAs include thin films of carbon nanotubes (SET et al., 2004) or nonlinear crystals (MALYAREVICH et al., 1998).

Alternatively, one can reproduce the same effect using nonlinear phase-modulation (GORDON; FISCHER, 2003), i.e., artificial SAs. Nonlinear Polarization Rotation (NPR) is a common passive mode-locking method that simulates a saturable absorber by using intensity-dependent changes in polarization[5]. NPR provides the mode-locking mechanism in our fiber-laser system.

When an intense optical pulse propagates through a non–polarization-maintaining fiber, the medium's nonlinear response induces an intensity-dependent change in the polarization state. This is usually not exactly a rotation of a linear polarization direction, but rather the change to some elliptical polarization state.

Figure 15 – Depiction of the NPR effect. As the pulse propagates along the fiber's z-axis, its elliptical polarization state rotates by an amount that grows with intensity. In the illustration, line thickness increases with z, so thin lines indicates light at the start of the fiber. In the left panel, a high-intensity signal undergoes a large rotation; in the right panel, a low-intensity signal rotates only slightly. The x and y axes correspond to the fiber's principal axes. For each position z, the local polarization ellipse is drawn, and a magnified vector indicating the combined semi-major and semi-minor axes shows the net rotation. A color map encodes the cumulative rotation relative to the initial alignment at $z = 0$.

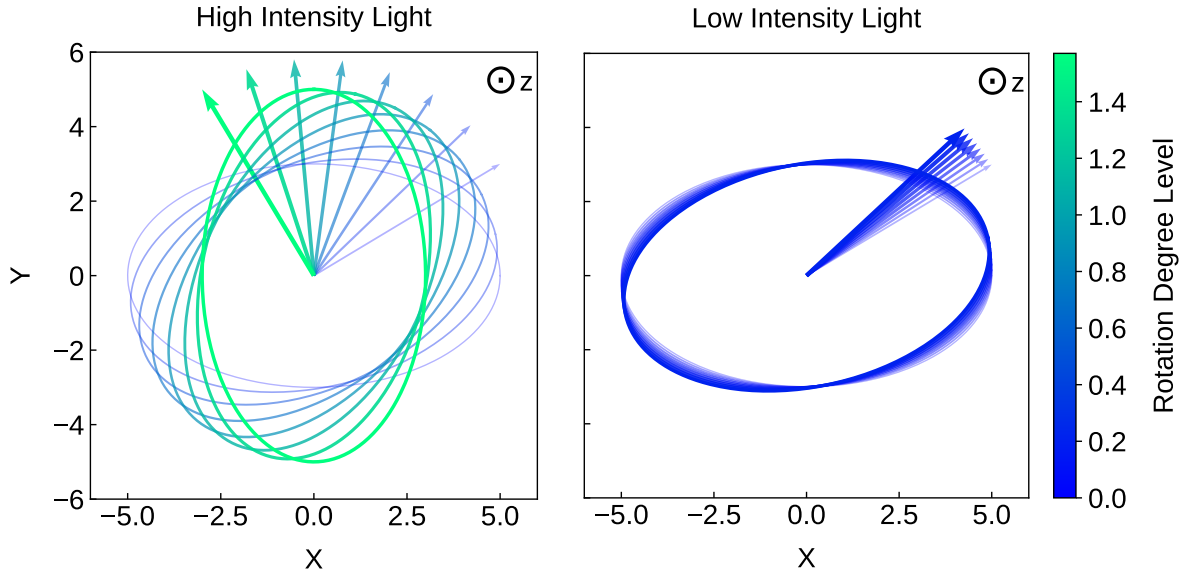

Source: The Author (2025)

Fig. 15 illustrates this phenomenon. At low intensities, the fiber preserves polarization and losses remain linear; at high intensities, the pulse acquires additional phase shifts inside the fiber. By placing polarizers at appropriate orientations, high-intensity pulses suffer lower loss

[5]The initial successful experiment demonstrating this was conducted using a fiber laser, as reported by Fermann et al. (1993).

and are preferentially amplified. Mode locking begins with random intensity fluctuations in the continuous-wave regime, where all modes propagate with low intensity and the system's transmission remains linear. Occasionally, a fluctuation produces a peak intense enough to trigger NPR: its polarization state rotates more strongly and, after the polarizer, experiences lower loss than the background. This preferential amplification allows the peak to grow on each round trip. As the pulse intensity increases, its center (acquiring the largest polarization rotation) suffers the least loss, while its wings incur higher loss. After many cavity round trips, these dynamics sculpt a stable ultrashort pulse whose shape and duration are set by the cavity parameters. Fig. 16 shows the essential elements for locking the modes via NPR.

Figure 16 – Schematic of the basic optical components used to achieve a mode-locked state in a fiber laser through NPR.

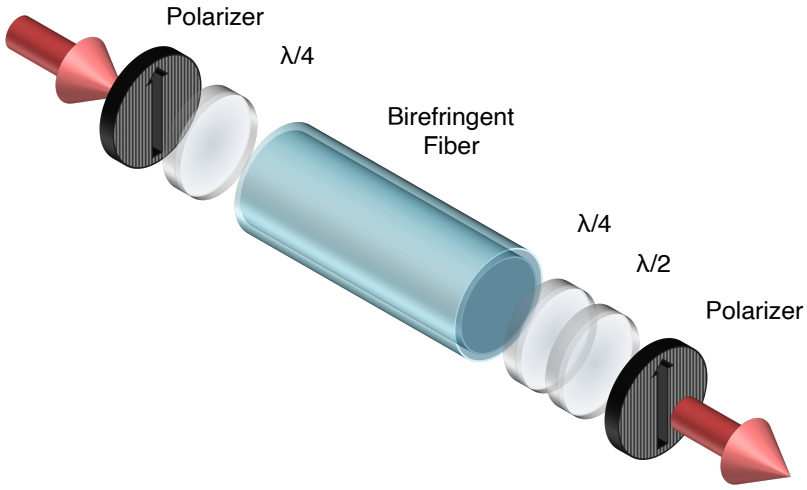

Source: The Author (2025)

For our setup, we control intra-cavity polarization with three waveplates. Before the fiber, a quarter waveplate ($\lambda/4$) sets the input ellipticity, determining how much the pulse's polarization will rotate during propagation. After the beam exits the fiber, a second $\lambda/4$ and a half waveplate ($\lambda/2$) undo part of that rotation to adjust the output coupling. Because the polarizer transmits only one polarization direction, transmission depends on the instantaneous intensity: stronger pulses align better with the polarizer and experience lower loss, thus emulating a saturable absorber.

4.1.3 Key nonlinear responses in the mode-locking process

The phenomenon underpinning NPR in mode-locked lasers is the optical Kerr effect, where the material's refractive index is altered by the electric field of the light wave only. The self-induced change in refractive index Δn is given by

$$\Delta n = n_2 I(t). \tag{4.3}$$

Here, n_2 denotes the nonlinear refractive index, while $I(t)$ indicates the time-dependent intensity of the pulse[6]. The parameter n_2 is associated with the medium's third-order susceptibility $\chi^{(3)}$, and the pulse intensity is given by

$$I(t) = \frac{|a(t)|^2}{A_{\text{eff}}}, \tag{4.4}$$

where $a(t)$ represents the amplitude of the electromagnetic field, and A_{eff} is the effective beam area in the medium. Because n_2 is typically very small[7], the Kerr effect becomes appreciable only for the high intensities provided by laser pulses. The intensity-dependent refractive index from the optical Kerr effect gives rise to two key nonlinear phenomena: Self-Phase Modulation (SPM) and Cross-Phase Modulation (XPM). In SPM, a pulse's own intensity induces a time-varying phase shift, broadening its spectrum. Meanwhile, in XPM, the intensity of one polarization component imposes a phase shift on the orthogonal component. The combination of SPM and XPM produces an intensity-dependent change in the pulse's polarization state, which underlies NPR.

As a pulse propagates, the Kerr effect makes its refractive index, and hence its phase shift, depend on local intensity. The pulse peak, being most intense, acquires the largest phase shift, while its wings are subject to smaller shifts. This uneven phase accumulation across the pulse generates a time-dependent frequency modulation, known as chirp[8]: the leading edge and trailing edge pick up different instantaneous frequencies. Essentially, it means that different frequency components within the pulse arrive at different times. As a result, new frequency

[6] Eq. 4.3 can alternatively be formulated as $n = n_0 + n_2 I$, with n_0 referring to the linear refractive index (WEINER, 2011).

[7] For silica glass the value is around $2.22 \cdot 10^{-16}\ cm^2/W$ (SCHIEK, 2023).

[8] The extent of chirp can be quantified through the time-bandwidth product as expressed in Eq. 4.1, where the specified values may correspond to chirp-free pulse profiles. A higher $\Delta\nu\Delta t$ value sometimes signifies the presence of chirp, although it is not always the case (WEINER, 2011).

components are created and the pulse spectrum broadens. This phenomenon is referred to as SPM.

The propagation of a pulse through the medium along z can be written in terms of the normalized envelope $U(z,\tau)$ as (AGRAWAL, 2007)

$$\frac{\partial U}{\partial z} = i\gamma P_0 \mathrm{e}^{-\alpha z} |U|^2 U, \tag{4.5}$$

where P_0 is the peak power, α accounts for fiber losses, and γ is a nonlinear coefficient related to the refractive index n_2, expressed as

$$\gamma = \frac{\omega_0 n_2}{c A_{\mathsf{eff}}}, \tag{4.6}$$

with c is the speed of light and ω_0 is the carrier frequency. The amplitude $U(z,\tau)$ of the pulse envelope depends on a dimensionless retarded time τ, i.e., is associated with a reference frame traveling with the pulse at the group velocity v_g, with normalization provided by the input pulse duration T_0. Therefore,

$$\tau = \frac{t - z/v_g}{T_0}. \tag{4.7}$$

Since $|U|^2$ remains unchanged during the propagation, Eq. 4.5 can be easily integrated[9] to give

$$U(L,\tau) = U(0,\tau) \exp\left[i \frac{\gamma P_0 |U(0,\tau)|^2 \left(1 - \mathrm{e}^{-\alpha L}\right)}{\alpha} \right]. \tag{4.8}$$

The resulting nonlinear phase shift ϕ_{NL} is

$$\phi_{\mathsf{NL}}(L,\tau) = |U(0,\tau)|^2 \left(\frac{L_{\mathsf{eff}}}{L_{\mathsf{NL}}} \right), \tag{4.9}$$

where

$$L_{NL} = (\gamma P_0)^{-1} \quad \text{, and} \quad L_{\mathsf{eff}} = \frac{[1 - \exp(-\alpha L)]}{\alpha}. \tag{4.10}$$

[9] We use the relations

$$\int \frac{dx}{x} = \ln(x) + C \quad \text{and} \quad \int a\mathrm{e}^{-bx} dx = -\frac{a\mathrm{e}^{-bx}}{b} + C,$$

and set the integration limits $[0, L]$, where L is the total propagation path.

L_{NL} and L_{eff} are the nonlinear length and effective length, respectively. The maximum phase shift ϕ_{max} occurs at the center of the pulse at $\tau = 0$. If we normalize U such that $|U(0,0)| = 1$, we obtain

$$\phi_{\text{max}} = \frac{L_{\text{eff}}}{L_{\text{NL}}}. \tag{4.11}$$

Spectral changes induced by SPM arise because the nonlinear phase shift ϕ_{NL} varies in time. A temporally changing phase indicates that the instantaneous optical frequency deviates from the central frequency ω_0 throughout the pulse (AGRAWAL, 2007). The instantaneous frequency ω_{inst} is essentially minus the derivative with respect to time of the overall phase (WEINER, 2011)

$$\omega_{\text{inst}}(\tau) = -\frac{d\phi}{d\tau} = -\frac{d}{d\tau}\left[\omega_0\tau + \phi_{\text{NL}}(\tau)\right] = -\omega_0 - \frac{d\phi_{\text{NL}}}{d\tau}. \tag{4.12}$$

Hence, the frequency deviation from the carrier $\delta\omega(\tau) = \omega_{\text{inst}}(\tau) - \omega_0$ is

$$\delta\omega(\tau) = -\frac{d\phi_{\text{NL}}}{d\tau} = -\left(\frac{L_{\text{eff}}}{L_{\text{NL}}}\right)\frac{\partial}{\partial\tau}\left|U(0,\tau)\right|^2. \tag{4.13}$$

Figure 17 – Simulation of the SPM for a Gaussian input $\exp[-t^2/T_0]$. The propagation distance z is normalized to $z_0 = (\pi/2)L_d$, where L_d is the total distance.

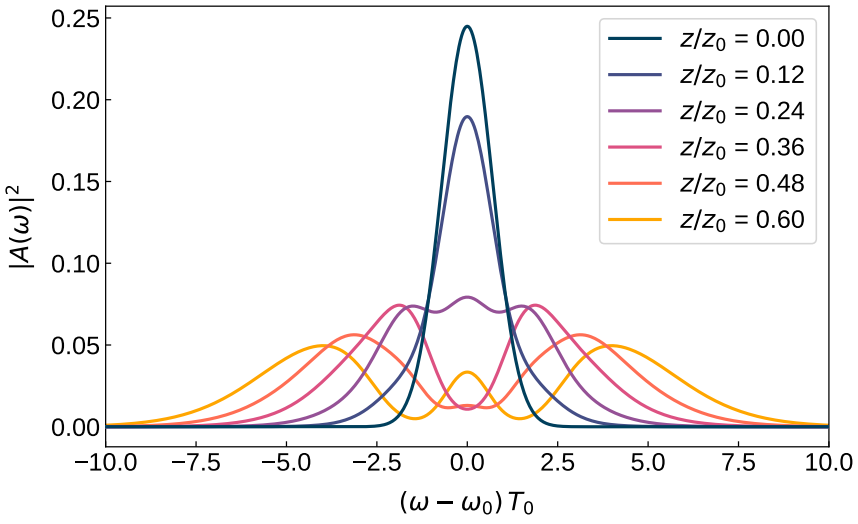

Source: The Author (2025)

New frequency components emerge around the pulse's central frequency. The chirp effect caused by SPM magnifies as it travels further. Thus, as the pulse progresses through the

fiber, additional frequency components are persistently produced. Using a Python script, we are able to simulate the SPM on a Gaussian pulse, as illustrated in Fig. 17. Each plotted line represents a distinct position along the propagation path. In this scenario, the parameters are set as $\gamma P_0 = 5\pi/\text{km}$, $\alpha = 2 \cdot 10^{-3}/km$, with a $T_0 = 5$ ps pulse spanning a distance of 0.5 km. The approximation for the maximum number of peaks M observed in the spectrum broadened by SPM is represented by the relation

$$\phi_{\text{max}} \approx \left(M - \frac{1}{2}\right)\pi. \tag{4.14}$$

When multiple optical fields at different wavelengths propagate together in a fiber, they interact via the Kerr nonlinearity. This interaction manifests both as phase modulation, where the fields influence each other's phase without direct energy exchange, and as four-wave mixing, where energy can be redistributed among different frequency components. Cross-Phase Modulation (XPM) is the process by which the intensity of one field (or one polarization component) induces a phase shift on another. In NPR, XPM causes an intensity-dependent phase shift of a given polarization by its orthogonal partner, driving the evolution of the overall polarization state. Considering the field envelope as $A(z,t) = A_1(z,t) + A_2(z,t)$, Eq. 4.5 leads to the derived set of coupled equations (AGRAWAL, 2007)

$$\begin{cases} \frac{\partial A_1}{\partial t} = i\gamma\left(|A_1|^2 + 2\,|A_2|^2\right)A_1. \\ \frac{\partial A_2}{\partial t} = i\gamma\left(2\,|A_1|^2 + |A_2|^2\right)A_2. \end{cases} \tag{4.15}$$

Solving these coupled equations, a task beyond the scope of this study, shows that the nonlinear relative phase is (CAMPOS, 2020)

$$\Delta\phi_{\text{NL}} = \frac{2\gamma L}{3}\left(|A_1|^2 - |A_2|^2\right) \tag{4.16}$$

The above expression shows that only elliptically polarized light undergoes NPR, as detailed by (CAMPOS, 2020). XPM always accompanies SPM when two or more optical fields propagate together in a fiber. Physically, XPM arises because the refractive index experienced by one beam in a nonlinear medium depends not only on its own intensity but also on the intensities of other copropagating beams (AGRAWAL, 2007).

4.1.4 Dispersion and Balancing

Another key effect for pulses in nonlinear media is dispersion, which describes how the phase velocity of light depends on frequency. A pulse consists of many frequency components, so its envelope travels at the group velocity v_g. Group Velocity Dispersion (GVD) measures how v_g varies with frequency: when GVD is nonzero, different frequencies complete the cavity round trip in slightly different times, causing spectral broadening. After traversing a dispersive segment of length L, the pulse acquires an additional spectral phase

$$\phi(\omega) = -\beta(\omega)L, \tag{4.17}$$

where $\beta(\omega)$ is the propagation constant

$$\beta(\omega) = \frac{\omega n(\omega)}{c}. \tag{4.18}$$

Expanding $\beta(\omega)$ around the carrier frequency ω_0 to second order gives

$$\phi(\omega) = -\left[\beta(\omega_0) + \left.\frac{\partial\beta}{\partial\omega}\right|_{\omega_0}(\omega-\omega_0) + \frac{1}{2}\left.\frac{\partial^2\beta}{\partial\omega^2}\right|_{\omega_0}(\omega-\omega_0)^2\right]L,$$

$$\phi(\omega) = -\left(\beta_0 + \beta_1\widetilde{\omega} + \frac{\beta_2}{2}\widetilde{\omega}^2\right)L, \tag{4.19}$$

with $\beta_n = \partial^n\beta/\partial\omega^n$ and $\widetilde{\omega} = \omega - \omega_0$. Here we identify β_1 as $(v_g)^{-1}$ and β_2 is the GVD parameter. The dependence of β_1 and

$$\beta_2$$

on ω is crucial because it governs how different frequency components of a broadband pulse accumulate phase at different rates. If $\beta(\omega)$ were constant, then both β_1 and β_2 would vanish, implying that all spectral components acquire the same phase delay. In this case, the pulse envelope experiences only a global phase shift without any change in its temporal shape. The resulting frequency-dependent delay of the pulse envelope is

$$\xi(\omega) = -\frac{d\phi(\omega)}{d\omega} = \beta_1 L + \beta_2\widetilde{\omega}L, \tag{4.20}$$

showing that different spectral components arrive at different times, which stretches or compresses the pulse depending on the sign of β_2. For $\beta_2 > 0$, normal dispersion occurs,

whereby higher frequencies (or shorter wavelengths) propagate more slowly, shifting toward the back of the pulse and resulting in an up-chirp, i.e., frequency increases over time. Conversely, when $\beta_2 < 0$, we encounter anomalous dispersion, where higher frequencies travel more rapidly, tending toward the front of the pulse, thus causing a down-chirp with a frequency reduction over time.

As we have seen, either SPM or normal GVD acting alone on an ultrashort pulse leads to a frequency up-chirp. However, new qualitative features emerge when GVD and SPM act together. When a high-peak-power pulse enters a dispersive medium, SPM initially imprints a positive (up-chirp) leading edge and a negative (down-chirp) trailing edge on the pulse. If the dispersion is normal, the red-shifted trailing edge slows down relative to the blue-shifted leading edge, causing additional temporal broadening of the pulse. Conversely, in anomalous dispersion, the blue-shifted frequencies advance, and the red-shifted ones lag, effectively compensating for the chirp induced by SPM. This interplay can lead to pulse compression, or even to the formation of fundamental solitons (CAMPOS, 2020) when SPM and GVD exactly balance one another. Optical components capable of inducing angular dispersion, such as grating pairs in our context or prism arrangements, are used to manage GVD. The relationship between angular and temporal dispersion can be found in Weiner (2011).

The combined action of GVD and SPM is described by the Nonlinear Schrödinger Equation (NLSE). Its detailed derivation can be found in (AGRAWAL, 2007; WEINER, 2011; CAMPOS, 2020). For the slowly varying pulse envelope $A(z, \tau)$, the NLSE expression takes the form of

$$\frac{\partial A}{\partial z} + i\frac{\beta_2}{2T_0^2}\frac{\partial^2 A}{\partial \tau^2} - i\gamma \left|A\right|^2 A = 0. \tag{4.21}$$

This expression is the lossless limit of the full propagation equation, i.e., $\alpha = 0$. One can include cavity losses by adding a linear attenuation term $(\alpha/2)A$ to the left-hand side of Eq. 4.21.

In summary, the central mechanism of passive mode-locking through NPR involves a complex interaction between nonlinearity and dispersion. Ultrashort pulses perpetually alter their spectral and temporal characteristics by incorporating SPM and XPM. Concurrently, the polarizing components select higher intensity peaks, thus ensuring a stable sequence of pulses. At the same time, GVD adjusts or sometimes enhances the nonlinear phase shift. The intricate equilibrium of nonlinear phase shifts, polarization-induced loss, and chromatic dispersion ultimately shapes the pulse's duration, energy, and stability within the laser.

4.2 THE QUASI MODE-LOCKED PHASE

A statistical formulation of the passive mode-locking regime was introduced in the early 2000s, where an effective "Hamiltonian" was proposed. Gordon and Fischer (2002) rigorously demonstrated that passive mode locking can be viewed as a thermodynamic first-order phase transition within the space of mode amplitudes, with noise acting as temperature and saturable absorption as the ordering interaction. However, their work did not include the nonlinear effects discussed in Subsection 4.1.3. This neglected feature was later addressed when they extended their model to include GVD and Kerr nonlinearity within the same statistical mechanics framework (GORDON; FISCHER, 2003). Their objective was to demonstrate that, despite these key physical influences, the development of stable pulses still aligns with a discrete transition in an effective "temperature" (characterized by noise intensity). Through both analytical (soliton regime) and numerical (general case) analyses, they illustrated that pulse generation is sustained as a first-order transition, influenced by the interaction between noise and saturable absorption.

A different approach within the context of RSB was later explored by Leuzzi et al. (2009), and has since been extended in several works (ANTENUCCI et al., 2015; ANTENUCCI et al., 2016; ANTENUCCI, 2016). As discussed in Chapter 3, the SML phase, in this framework, is analogous to the ferromagnetic phase in spin models. This phase emerges at low disorder R_j and high pumping power. Antenucci, Berganza and Leuzzi (2015) provided the first statistical-mechanical treatment of real multimode, ultrashort, mode-locked lasers in closed cavities, explicitly accounting for topological disorder. While Gordon and Fischer's model relies on mean-field theory using Fokker–Planck and Langevin equations, the work of Antenucci, Berganza and Leuzzi (2015) adopts a Hamiltonian-based formulation with interactions. This approach offers new insights into laser dynamics by considering nonlinear interactions among modes and by moving beyond mean-field approximations. Specifically, it accounts for frequency-dependent couplings and topological disorder, such as incomplete mode overlap due to cavity imperfections.

Earlier studies assumed a fully connected (narrowband) mean-field approximation in which all mode pairs interact equally. In contrast, Antenucci, Berganza and Leuzzi (2015) now explicitly enforce a Frequency Matching Condition (FMC) for any quadruplet of modes $\{k_1, k_2, k_3, k_4\}$, i.e.,

$$|\nu_{k_1} - \nu_{k_2} + \nu_{k_3} - \nu_{k_4}| \leq \gamma, \tag{4.22}$$

where γ is the gain bandwidth. Since the first approaches (GORDON; FISCHER, 2002), statistical mechanical treatments have mostly relied on, as already mentioned, the narrowband approximations, where the mode spacing $\delta\nu$ is smaller than γ, where modes fall within a narrow frequency band $\Delta\nu$. In contrast, the newer approach introduces frequency-dependent mode populations governed by a gain profile $g(\nu)$ and incorporates nontrivial FMC constraints. The results reveal that, depending on system properties, cavity geometry, and the balance between gain and nonlinearity, the laser can exhibit different thermodynamic-like phases. The Hamiltonian is expressed as (ANTENUCCI, 2016)

$$\mathcal{H} = -\sum_{k=1}^{N} g_k |a_k|^2 - \frac{\Gamma}{2} \sum_{\{k_1,k_2,k_3,k_4\}} a_{k_1} a_{k_2}^* a_{k_3} a_{k_4}^*, \tag{4.23}$$

where $g_k = g(\nu_k)$ is the net gain profile, and Γ is the Self-Amplitude Modulation (SAM)[10]. g_k and Γ are selected as real numbers, with the dispersion and Kerr-lens effect[11] being disregarded. The model also includes a global power constraint, such as Eq. 3.7. This results in a stochastic competition for gain among the coupled optical modes, and consequently introduces disorder in the system. Thus, even in a perfectly ordered mode-locked laser (no material disorder), the intrinsic frustration from enforcing both a fixed total power and a nonlinear four-wave coupling among many modes engenders a glassy phase-locked regime.

Our group (ALVES et al., 2024) reported the first experimental evidence of a glassy phase in a Yb-doped MLFL, appearing before the onset of the SML. This phase, called Quasi-Mode-Locking (QML), emerges between the replica-symmetric CW and SML regimes and is fully characterized by the POP (see Section 3.3). It is worth noting that the Hamiltonian in Eq.4.23 does not capture the full dynamics of the QML regime. A more complete description follows by mixing the FMC with Eq.3.6 and writing the Hamiltonian as

$$\mathcal{H} = -\sum_{k_1,k_2} g^{(2)}_{k_1,k_2} a_{k_1} a_{k_2}^* + \sum_{\{k_1,k_2,k_3,k_4\}} g^{(4)}_{k_1,k_2,k_3,k_4} a_{k_1} a_{k_2}^* a_{k_3} a_{k_4}^*. \tag{4.24}$$

[10] It is important to note that, even though not explicitly stated earlier, SAM refers to the intensity-dependent loss within the laser cavity. This functions similarly to a fast saturable absorber, meaning that higher instantaneous pulse intensities result in reduced losses. This phenomenon arises as a direct effect of SPM, in which the phase shift is transformed by the cavity's intracavity optics into a rapid amplitude modulation. This modulation effectively facilitates the transmission of the pulse peak while discriminating against its wings (WEINER, 2011).

[11] This phenomenon is not the optical Kerr effect as described in 4.1.3.

Here $g^{(2)}_{k_1,k_2} = g(\nu_{k_1}, \nu_{k_2})$ encodes the linear gain and loss between modes k_1 and k_2, while $g^{(4)}_{k_1,k_2,k_3,k_4}$ arises from the Kerr nonlinearity and is proportional to the third-order susceptibility $\chi^{(3)}$. Although first-principles calculation of these quadratic and quartic couplings is impractical, they are usually modeled as Gaussian random variables, as in earlier magnetic–photonic analogies (ANGELANI et al., 2006a; LEUZZI et al., 2009; ANTENUCCI et al., 2015). FMC is enforced in to ensure nontrivial, competing mode interactions. This full Hamiltonian thus embraces both gain competition and nonlinear mixing, providing a somewhat foundation for RSB phenomenon in the QML phase.

Before achieving SML operation, competition for gain among modes strengthens as the variance of their coupling distribution increases. This enhancement produces frustrated, partially synchronized oscillations of nontrivially correlated modes. For each initial configuration (replica) in this phase, the mode couplings converge to one of infinitely many metastable states. This coexistence of a vast ensemble of coupling arrangements is captured by the Parisi overlap parameter q (or experimentally, by the IFO). Fig. 18 presents three examples of the overlap distribution $P(q)$ for a total of 3000 replicas. In the QML phase, $P(q)$ is bimodal, indicating two preferred values of the Parisi overlap. This behavior closely parallels the overlap distribution observed in the RL phase above threshold (see Fig. 12). In both CW and SML regimes, $P(q)$ takes a Gaussian form centered at $q = 0$, as expected for these phases.

Figure 18 – Overlap distribution $P(q)$ across three distinct regimes within a Yb-doped MLFL: (a) CW; (b) QML; and (c) SML. The sequence of graphs from left to right corresponds to an upward pumping rate.

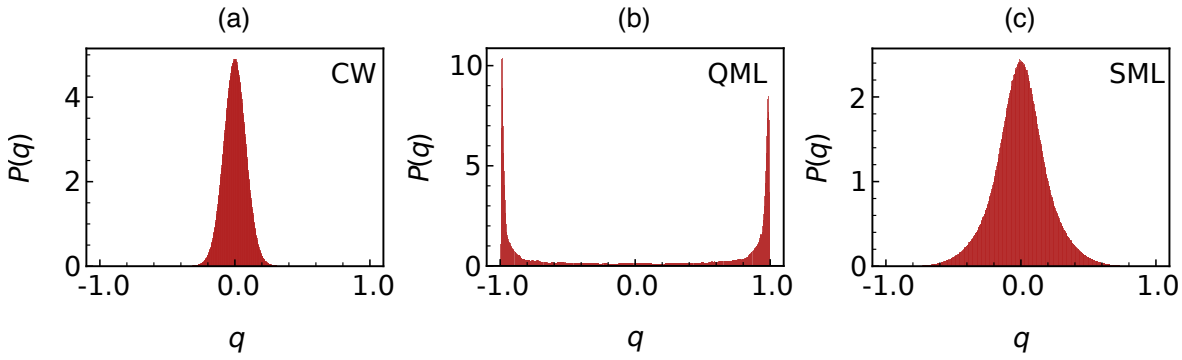

Source: Adapted from ALVES et al. (2024)

We may also examine the transitions between photonic phases by looking at the value $|q_{\text{max}}|$. As shown in Fig. 19, the transition from QML to SML appears as a sudden jump in $|q_{\text{max}}|$. In the glassy QML regime, the laser does not emit ultrashort pulses and fails to achieve phase coherence. Instead, many longitudinal modes engage in a randomly frustrated

race for gain, leading to a nontrivial structure in the overlap matrix $Q_{\alpha\beta}$. Once the SML regime is reached, energy concentrates into a stable pulse that spans many modes oscillating coherently. Their intensities equalize, gain competition vanishes, and $Q_{\alpha\beta} = 0$. By contrast, the CW-QML transition produces a "smoothly" increasing curve of $|q_{\max}|$ versus $\mathcal{P}$ (or current, in our case). As the pump rises, nonlinear effects activate more modes. Because the total gain is finite, each additional mode must compete/cooperate with the existing ones. This growing interaction drives up $|q_{\max}|$ continuously until enough energy accumulates in a developing pulse to overcome the competition. At that point, as already mentioned, a stable pulse forms and the system undergoes the abrupt transition into the SML regime.

Figure 19 – Absolute value of $|q_{\max}|$ as a function of the input current (equivalent as pumping power. plotted against input current (proportional to pump power). The sharp increase near $400\ mA$ marks the transition from the QML regime to the SML regime.

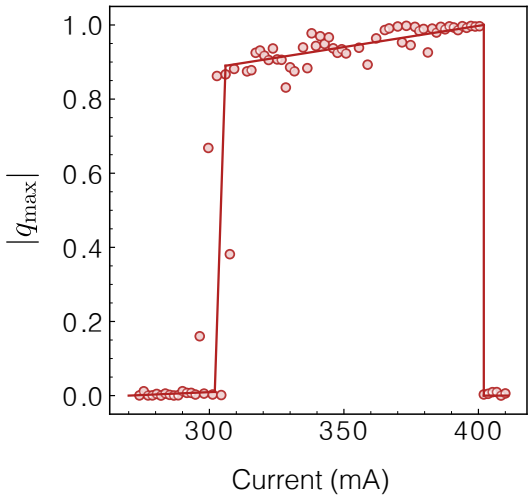

Source: Adapted from ALVES et al. (2024)

To fully understand the mode interactions in the QML phase, we now turn our attention to the PCC, which quantifies the correlations across the modes in the spectrum. Here, we focus exclusively on the QML regime. For a more complete analysis of the system across all regimes, see the letter published on the subject (ALVES et al., 2024) and the master's thesis of Alves (2023).

Fig. 20 shows the PCC heatmap for a point in the QML regime. The striking feature is the coexistence of positive and negative correlation strips among a set of modes. Due to the symmetry of the PCC, analysis can focus solely on the upper (or lower) portion limited by the main diagonal, which represents mode self-correlations. From Fig. 20, we observe that the spectrum is organized into two main mode bands. Within each band, modes are positively

Figure 20 – Pearson correlation matrix ρ in the QML regime. The PCC forms an $N \times N$ symmetric matrix, where N is the number of spectral bins. Diagonal entries are unity (self-correlation); off-diagonals show pairwise correlations between wavelengths.

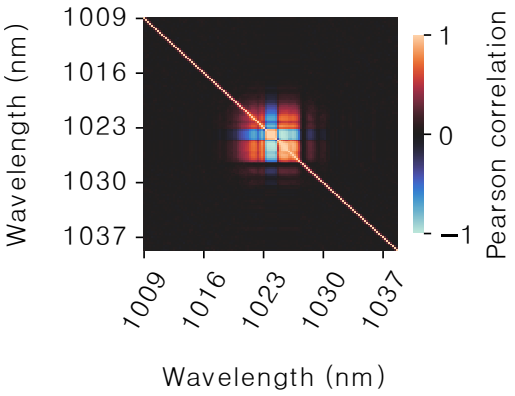

Source: Adapted from ALVES et al. (2024)

correlated with their nearest neighbors. However, these bands are negatively correlated with one another. For example, the modes near 1023 nm exhibits strong positive correlation with nearby modes, but shifts to negative correlation with modes around 1025 nm. This indicates that when one group of modes gains energy (increases in intensity), the other loses.

Since the frustrated gain competition induces the modes to be split into two anticorrelated groups, the resulting spectrum naturally exhibits two intensity peaks separated by a valley. Fig. 21 represents a plot of the spectrum in the QML region.

Figure 21 – Typical spectra for the QML regime. The peaks in the plot correspond to competing sets of modes around $\lambda_1 = 1024.4\ nm$ and $\lambda_2 = 1025.6\ nm$.

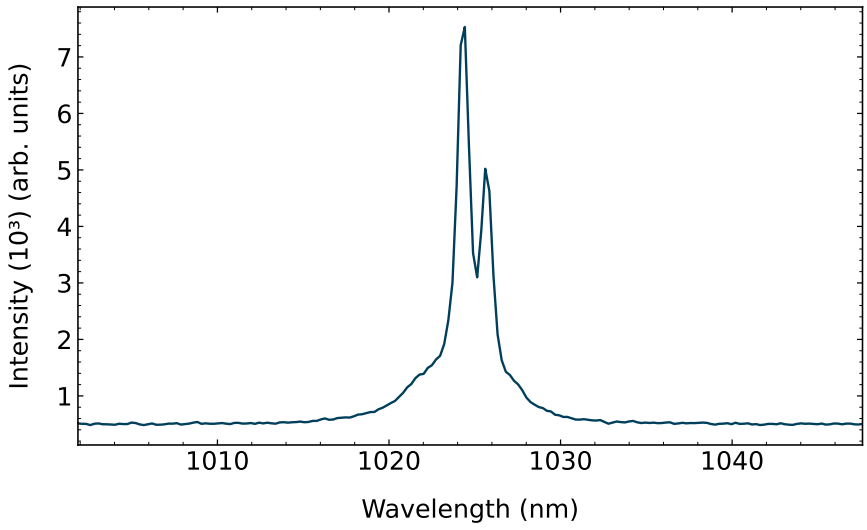

Source: The Author (2025)

It is worth noting that the number of peaks is not necessarily always two. Different cavity

configurations and pumping powers can yield a varying numbers of peaks. In this work, most spectra exhibited only two peaks[12].

While collecting replicas at a fixed current, the intensity peaks fluctuate competitively around their mean values. This type of dynamics, beyond what the POP shows, helps identify the QML regime.

A natural question that arises from this is: what kind of distribution do these peak fluctuations have? In disordered media, a power-law Lévy distribution has been widely used. A Lévy distribution is a continuous probability distribution characterized by heavy right skewed tails and infinite variance. It is often used to model random processes, such as Brownian motion (KLAFTER; SHLESINGER; ZUMOFEN, 1996) and animal foraging (EDWARDS et al., 2007). Lévy statistics also found applications in optics (BARTHELEMY; BERTOLOTTI; WIERSMA, 2008), more specifically, in RLs (GOMES et al., 2021; GOMES et al., 2023). They serve as indicators of the lasing threshold (UPPU; MUJUMDAR, 2014; RAPOSO; GOMES, 2015), characterize fluctuation correlations (MERRILL; CAO; DUFRESNE, 2016), and have been applied to the study of random fiber-laser dynamics (LI et al., 2019). More importantly, Lévy behavior has also been found alongside the RSB phenomena in RLs (GOMES et al., 2016b; ARAÚJO; GOMES; RAPOSO, 2017; LIMA et al., 2017), linking them with the photonic glassy regime. Thus, we might expect the fluctuations of the peaks in Fig.21 to follow a Lévy-type distribution. However, this criterion is not entirely met. Fig.22 shows the histograms of these peak intensities. The histograms are constructed by fixing a wavelength and recording its intensity value for every replica taken in the system at a fixed current. For the experiment under consideration, we obtained 3000 intensity values. The intensity array is then normalized as

$$I_{\text{norm}} = \frac{I - I_{\text{min}}}{I_{\text{max}} - I_{\text{min}}}, \tag{4.25}$$

where I is the measured intensity, and I_{min} and I_{max} are the minimum and maximum intensity values of the array at that current. This normalization rescales the intensity to the interval $[0, 1]$, where 0.5 corresponds to the mean intensity for the given wavelength.

Although the second peak displays characteristics typically associated with a Lévy distribution, the presence of a mirrored distribution from the first peak changes the overall interpretation. Both histograms fall into the category of L-shaped distributions, a broader classification for these distributions with a steep rise followed by a long decay, or vice versa (BRADLEY, 1982).

[12] The number of peaks also depends on the optical spectrometer resolution. Closely spaced modes may appear as a single peak, so each observed "peak" actually represents a set of unresolved modes.

Figure 22 – Normalized intensity histograms for $\lambda_1 = 1024.4$ nm and $\lambda_2 = 1025.6$ nm, centered around their respective mean intensities for a current value inside the QML phase.

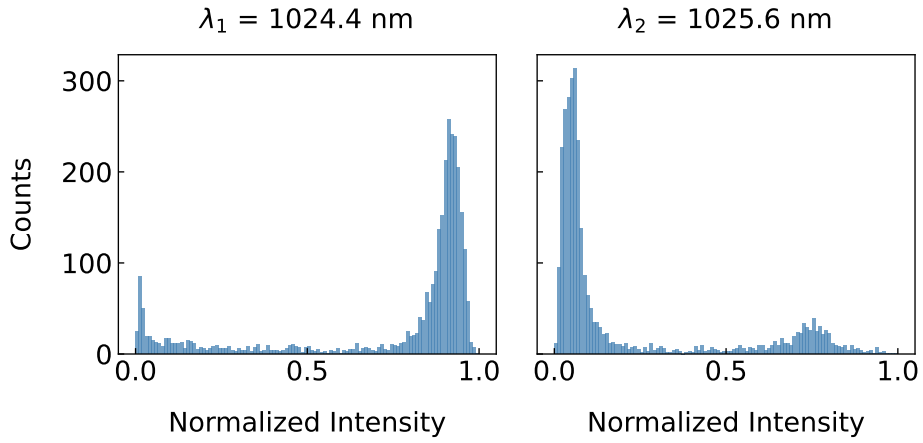

Source: The Author (2025)

One could argue that a left L-shaped distribution could be termed a left-tailed Lévy distribution, but given the lack of information in the literature and for consistency with historical terminology associated with Lévy distributions, we adopt the L-shaped label here[13]. Regardless of what we call these distributions, they encode two key phenomena. The first, which we will examine later, is the presence of rare events. In Fig. 22, despite the peak selected, most replicas cluster around a particular extreme of intensity relative to their mean, indicating that the system spends the majority of its time near that value. However, it occasionally visits other intensity levels, spending far less time there. These flights are rare, but not negligible. Similar behavior is observed, for example, in optical rogue waves (ONORATO et al., 2013), where rare events emerge from otherwise stable dynamics.

Second, the mirrored shape of the two peak distributions provides complementary evidence of the frustrated mode competition. When the first peak spends most of its time at high intensities, the second one remains low; as soon as the first goes into its low-intensity regions, the second rises. This pattern persists across the entire QML regime and contrasts with the CW and SML phases, where the same modes display uncorrelated Gaussian fluctuations. This overall behavior is illustrated by the heatmap in Fig. 23. Each column in the heatmap of Fig.23 corresponds to a top view of a histogram constructed in the same way as those shown in Fig.22.

Because in the QML phase the intensity histograms exhibit sharp peaks—i.e., the counts are

[13] One could also classify these distributions as J-shaped (CHOSH, 1978), which are characterized by a subtle concavity in the probability profile.

Figure 23 – Heatmap of the intensity distribution as a function of input current. Red dashed lines indicate regime boundaries: the left line marks the CW-QML transition, and the right line marks the QML-SML transition. The top plot is for $\lambda_1 = 1024.4$ nm and the bottom for $\lambda_2 = 1025.6$ nm

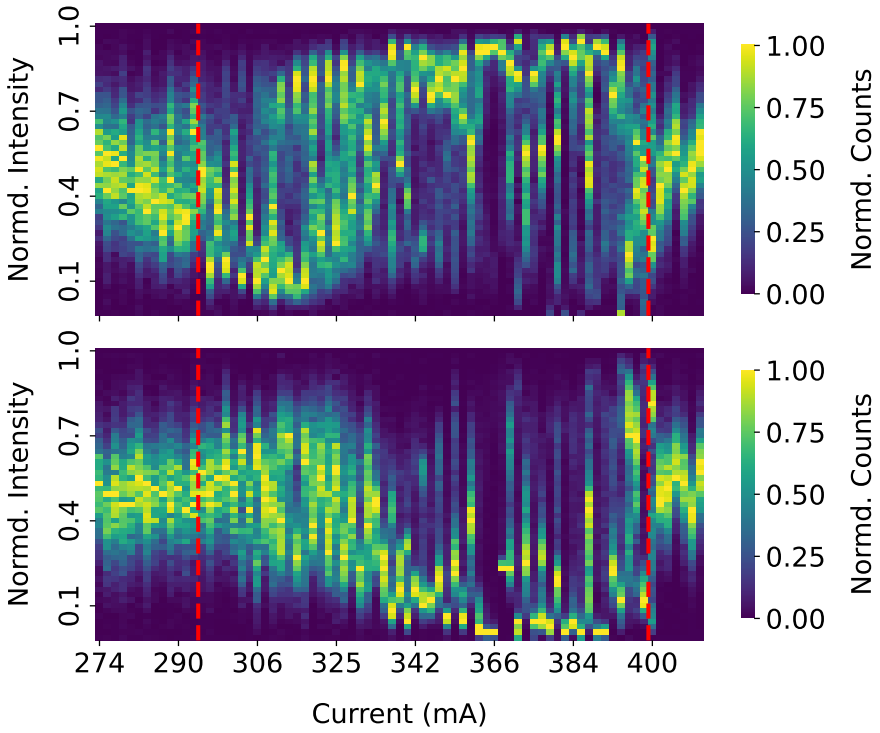

Source: The Author (2025)

concentrated in a very narrow intensity region—the colormap tends to obscure the more evenly distributed features. In practice, this makes visualization difficult due to the large discrepancy between the maximum count value of some histograms and the rest. To address this issue, we apply the same normalization procedure used for the intensity (Eq. 4.25), but now to the bin counts, rescaling them into the unit interval.

The QML region corresponds to the central portion of the heatmap, which is delimited by the red dashed lines. As the system crosses into the SML regime (right side), the intensity distribution changes abruptly from an L-shaped profile to a Gaussian distribution. By contrast, in the CW–QML boundary (left side), the histograms often exhibit a mixture of L-shaped and Gaussian distributions. This is because, in this lower-current regime, as already mentioned, optical nonlinearities are weak, and mode competition is only beginning to emerge, so the fluctuation statistics reflect both linear and upcoming nonlinear dynamics.

One final important concept to address is the idea of a replica in our system. As introduced in chapter 2, a replica corresponds to a single configuration of the system. In photonics, this translates to a single pulse of light. To be more precise, we must consider both the

repetition rate of the laser (f_{rep}) and the integration time of the optical spectrometer (t_{acq}). In RLs, the typical condition is that $f_{\text{rep}} \leq 1/t_{\text{acq}}$[14]. For instance, the experiments reported by Ghofraniha et al. (2015) and Gomes et al. (2016b) used a Q-switched Nd:YAG laser operating at $f_{\text{rep}} = 10$ Hz, while the spectrometers had integration times of 100 ms, effectively capturing single pulses per replica. However, in our case, the situation is quite different. Our Yb MLFL operates with a repetition rate of approximately 120 MHz, while the spectrometer's integration time is 9 ms (with 3.8 ms being the minimum allowed by the device). This implies that each data array corresponds to an average over roughly 10^6 pulses. Despite this, RSB still appears clearly in our system. Fig. 24 shows how the distribution $P(q)$ behaves with different integration times for the QML region. The figure clearly shows that varying the integration time does not affect the result: the bimodal shape of $P(q)$ remains unchanged, indicating the robustness of the result.

Figure 24 – Distribution of $P(q)$ for three different integration times. All plots correspond to the same current value and were constructed using the same number of data acquisitions (3000).

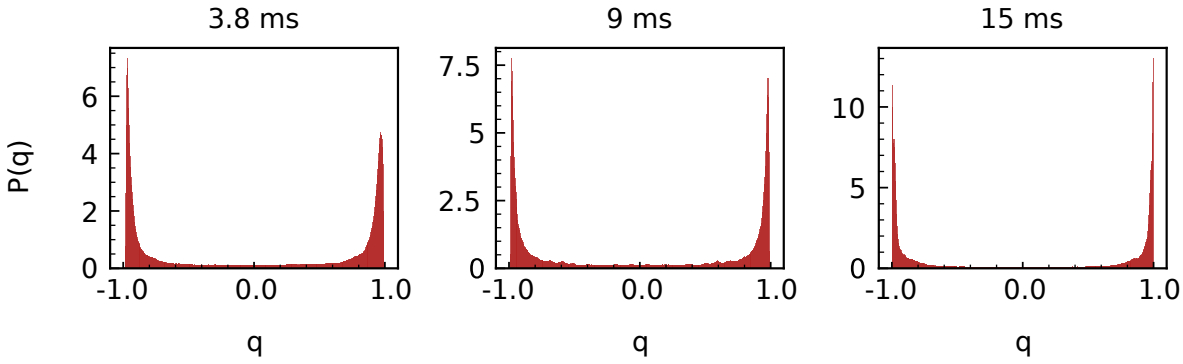

Source: Adapted from ALVES et al. (2024)

As a matter of fact, one could argue that increasing the integration time should conceal the RSB phenomenon. The premise is that averaging over too many pulses tends to wash out the subtle, correlated fluctuations between modes, which are needed for RSB to emerge. It is worth noting that the POP is highly sensitive. Indeed, recent studies have examined the stability of the pumping source itself to ensure that the RSB does not originate from intrinsic noise in the input (MOURA et al., 2017; ALVES et al., 2024). Therefore, it is logical to expect that averaging over a large number of pulses would suppress the delicate fluctuation patterns. From a statistical point of view, increasing the integration time by a significant factor invokes the Central Limit Theorem on the distributions shown in Fig. 22. In this limit, both peaks

[14] The number of pulses captured per measurement N_o is given by $N_o = f_{\text{rep}} t_{\text{acq}}$.

would tend toward Gaussian distributions centered around the mean intensity (e.g., near 0.5), and the energy fluctuations would be averaged out. As a result, the overlap parameter q would vanish, and no RSB signature would be detected. However, no systematic study has deeply explored this effect so far, and these are, of course, just some ideas and interpretations.

Despite these theoretical considerations, the experimental data presented in Fig. 24 supports the conclusion that, once the RSB phenomenon is present, changing the integration time within reasonable limits does not alter its signature.

5 TURBULENT DYNAMICS

As mentioned at the end of the previous chapter, the fact that RSB is intrinsically linked to intensity fluctuations in lasers has motivated several studies to focus on the statistical properties of these fluctuations. In particular, the presence of a turbulent behavior has been identified, giving rise to a novel area of research where RLs are used to observe statistical signatures of turbulence (GONZÁLEZ et al., 2017). Further studies have explored intermittency (MACÊDO et al., 2019), as well as the coexistence and interplay between turbulence and RSB in RLs (GONZÁLEZ et al., 2018; GOMES et al., 2021; GOMES et al., 2022; CORONEL et al., 2022b). Given that the intensity fluctuations in the Yb MLFL also exhibit nontrivial characteristics, it is natural to explore whether similar turbulent effects are present in our system, especially since several indicators point in that direction.

In this chapter, we presented a theoretical overview of turbulence and its statistical signatures in nonlinear photonic systems. We also introduced the statistical tools employed in our analysis, with particular emphasis on PCA, which provides a complementary perspective to more traditional approaches. Although these studies were originally motivated by results in RL, we did not focus on reproducing those derivations here. Instead, the aim was to consolidate the theoretical and methodological background necessary for the analysis of our own system. For readers interested in further details on turbulence in random lasers, the references cited at throughout this chapter provide comprehensive coverage.

5.1 BACKGROUND ON TURBULENCE

Turbulence is one of the most intriguing phenomena, not only in physics, but in nature as a whole. It manifests as chaotic, unpredictable fluid motion, appearing in countless contexts: from cigarette smoke and gusty winds to airplanes, river flows, and much more. It affects a wide range of systems, from vehicle aerodynamics and sediment transport to weather patterns. Turbulence is also found in planetary atmospheres, the solar corona, Earth's outer core, and even in the large-scale structure of galaxies (LESIEUR, 2008). However, despite its universality, turbulence is one of the most complex subjects to describe. As Horace Lamb, one of the most influential physicists of the 20th century in the field of hydrodynamics, once said:

> I am an old man now, and when I die and go to Heaven there are two matters on which I hope for enlightenment. One is quantum electrodynamics, and

> the other is the turbulent motion of fluids. And about the former I am really rather optimistic. (GOLDSTEIN, 1969, p. 23).

Indeed, the complexity of turbulent behavior has fascinated humanity for centuries. Evidence of this can be found in the studies of Leonardo da Vinci and in paintings, such as Vincent van Gogh's Starry Night, whose swirling patterns have recently been shown to exhibit remarkable statistical accuracy in representing turbulence (MA et al., 2024).

Let us consider a simplified historical approach to the subject. We begin with Leonhard Euler, who in the 1750s attempted to describe the motion of fluids while designing water fountains (L'VOV; PROCACCIA, 1998). He wrote Newton's equation of motion for a fluid of density ρ as (here we are neglecting external forces, such as gravity)

$$\frac{D\mathbf{u}}{Dt} \equiv \frac{\partial \mathbf{u}}{\partial t} + \mathbf{u} \cdot \nabla \mathbf{u} = -\frac{1}{\rho}\nabla p. \tag{5.1}$$

where $\mathbf{u} = \mathbf{u}(\mathbf{r}, t)$ and $p = p(\mathbf{r}, t)$ are the velocity and pressure fields, and D/Dt is the material derivative[1]. However, Euler's equation produces unrealistic velocity predictions for certain gradients of pressure. The crucial element missing in his equation is the viscous dissipation, which accounts for the internal friction between adjacent fluid elements. This was addressed during the first half of the 19th century, where the works of Claude-Louis Navier (NAVIER; PROVINCIALE; TOPOGRAFICO, 1839) and George Gabriel Stokes (STOKES, 1842) properly introduced this viscous term, yielding the well-known Navier-Stokes Equation (NSE)

$$\frac{D\mathbf{u}}{Dt} = -\frac{1}{\rho}\nabla p + \nu \nabla^2 \mathbf{u}. \tag{5.2}$$

Here, ν is the kinematic viscosity. Eq. 5.2 describes essentially a Newtonian fluid, meaning that the internal stress of the fluid is proportional to the shear rate. The NSE thus serves as the foundational model for incompressible Newtonian fluids. It successfully captures the behavior of common fluids such as water and air under normal conditions (BENZI; TOSCHI, 2023). Despite this, direct attempts to evaluate the solutions of this equation for natural flows can lead to discrepancies between predictions and experiments. This problem was addressed by Osborne Reynolds, who expressed the importance of non-dimensionalization of the NSE (REYNOLDS,

[1] The material derivative describes how a physical quantity, such as velocity, changes for a particle moving along with the fluid's flow (BIRD; STEWART; LIGHTFOOT, 2006)

1894). For this end, we consider the initial velocity U_0 of the fluid and a characteristic length scale[2] L. We then perform the following substitutions

$$\mathbf{u}^* \to \frac{\mathbf{u}}{U_0}, \quad \nabla^* \to L\nabla, \quad \mathbf{x}^* \to \frac{\mathbf{x}}{L}, \quad t^* \to \frac{tU_0}{L}, \quad \frac{p}{\rho} \to \frac{p}{\rho U_0^2}. \tag{5.3}$$

After some (arguably tedious) manipulations, one arrives at the dimensionless form of the NSE

$$\frac{\partial \mathbf{u}^*}{\partial t^*} + \mathbf{u}^* \cdot \nabla^* \mathbf{u}^* = -\nabla^* p^* + \frac{\nu}{U_0 L} \nabla^{*2} \mathbf{u}^*, \tag{5.4}$$

In the above equation, the only nonlinear contribution comes from the convective term $\mathbf{u}^* \cdot \nabla^* \mathbf{u}^*$. The pressure gradient, viscous Laplacian, and time derivative are all linear operators. The nonlinear term scales as U_0^2/L, while the viscous term scales as $\nu U_0/L^2$. Taking their ratio, we define the Reynolds number (Re) as

$$Re = \frac{U_0 L}{\nu}. \tag{5.5}$$

Eq. 5.5 quantifies how dominant the nonlinear effects are compared to viscous dissipation in a given fluid flow. A key consequence of this is that the qualitative behavior of the flow can be described by Re and it changes drastically when varying it. For $Re \ll 1$, viscous effects dominate, and the nonlinear terms can be neglected. In such regimes, NSE can often be solved analytically, and the flow is typically smooth and laminar (ordered flow in parallel layers with no disruption). However, in many natural and practical situations, $Re \gg 1$. In these cases, nonlinearities dominate, and no stable, stationary solutions exist for the equations of motion. Moreover, for this case, the linear regime cannot be used as a basis for any perturbative expansion (BENZI; TOSCHI, 2023). In other words, there is no small-parameter expansion around a known solution that can yield a significant analytical result. In this regime, the flow is highly sensitive to initial conditions, and the velocity field develops intricate, time-dependent vortices, eddies, and chaotic patterns (L'VOV; PROCACCIA, 1998). This regime is what we call turbulence. Another of Reynolds' insights was the fact that, regardless of the specific values of U_0, L, or ν, flows with the same Reynolds number exhibit similar dynamical behavior.

Modern ideas on turbulence are expressed in Lewis Fry Richardson's poem on turbulence:

[2] For example, consider a cylinder of radius L and height H and analyze the behavior of fluid flow around it, L represents this relevant scale (BENZI; TOSCHI, 2023).

> Big whirls have little whirls / That feed on their velocity, / And little whirls have lesser whirls / And so on to viscosity. (RICHARDSON, 1922)

These verses encapsulate the essential idea of turbulence: large-scale forcing injects energy into the system, which is then transferred through a cascade to successively smaller scales via the nonlinear dynamics of the fluid. Eventually, this energy reaches a sufficiently small scale where the energy is dissipated by viscosity and converted into heat. This idea of energy cascading from large to small scales became the foundation for many theoretical models of turbulence, often called cascade models, which aim to describe how this energy transfer works (L'VOV; PROCACCIA, 1998).

Because turbulent flows are so complex and random, it is not practical to track every fractional motion of the fluid. Consequently, it is more efficient to focus on the statistical properties of turbulence. However, even the velocity field statistics are often strongly affected by the specific boundary conditions of the system. A more universal characterization emerges when analyzing the statistics of velocity differences between two points $\mathbf{r}_1$ and $\mathbf{r}_2$ in the flow, viz

$$\delta\mathbf{u}(\mathbf{R}) = \mathbf{u}(\mathbf{r}_2) - \mathbf{u}(\mathbf{r}_1). \tag{5.6}$$

where we set $\mathbf{R} = \mathbf{r}_2 - \mathbf{r}_1$. Usually, instead of analyzing full 3D turbulence, researchers often just look at 1D slices, i.e., we project the velocity difference onto the direction of the separation vector $\mathbf{R}$

$$\delta u(R) = \delta\mathbf{u}(\mathbf{R}) \cdot \frac{\mathbf{R}}{R}. \tag{5.7}$$

With this set of speed increments at hand, we examine the probability distribution of these variations and compute their statistical moments (i.e., the averages of various powers), which are known as structure functions. That is,

$$S_n(R) = \langle \delta u(R)^n \rangle, \quad n \in \mathbb{N}^*. \tag{5.8}$$

Here, $\langle \ldots \rangle$ denotes an ensemble average. These moments give us insight into the shape and behavior of the distribution in the increments of velocities. For example, the first moment ($n = 1$) is the mean, the second ($n = 2$) is related to the variance (spread), the third ($n = 3$) describes skewness (asymmetry), and the fourth ($n = 4$) captures kurtosis (how heavy the

tails are). For a Gaussian distribution, everything about the statistics is determined up to the second moment, S_2. Higher-order moments do not carry any relevant information to the distribution (L'VOV; PROCACCIA, 1998). However, systems with highly non-Gaussian statistics cannot be solely described by the variance. This means that the higher-order moments, such as S_3 and S_4, carry essential information about the shape of the distribution. Theoretical efforts to understand the universal small-scale structure of turbulence can be broadly categorized into two approaches (L'VOV; PROCACCIA, 1998). The first is based on the NSE. Usually, one recognizes that fluid dynamics is a classical field theory; thus, we need to employ field theoretic techniques to compute statistical properties, although this is significantly difficult and rarely successful. The second approach consists of a wide range of phenomenological models. Despite not being directly derived from the NSEs, these models have provided valuable insights by matching more closely with experimental observations. In the following, we will focus on this second category.

One of the most insightful contributions to the concept of turbulence came from Andrei Kolmogorov in 1941 (K41) (KOLMOGOROV, 1941). He proposed that certain statistical properties of turbulence could be universal, meaning that they are independent of the specific details of the fluid or the flow, as long as Re is significantly large. This idea of universality relies on the concept of an inertial range. The inertial range is a scale region R[3] between the large scale of energy injection L, and the small scale η at which viscosity is significant (often called the Kolmogorov scale). In turbulent flows, where $Re \gg 1$, there exists a wide separation between these two scales, such that (L'VOV; PROCACCIA, 1998)

$$\eta \ll R \ll L. \tag{5.9}$$

In this intermediate regime, the energy cascades without being affected by either the energy input mechanism or the dissipation. Once the fluid is in the stationary state, that is, the statistical elements of the flow do not change in time, the rate of energy injected at the large scale is identical to the rate of energy dissipated at the smallest scale (L'VOV; PROCACCIA, 1998). This constant energy flux ϵ must be the same across all scales in the inertial range.

Kolmogorov's universality assumptions can be stated as (GONZÁLEZ, 2017)

[3] This region is also known as the Taylor microscale (GONZÁLEZ, 2017), named in honor of Geoffrey Taylor, whose earlier work (TAYLOR, 1935) laid important groundwork for the statistical approach to turbulence.

1. At very high, but finite Re, all small-scale statistical properties are uniquely determined by the viscosity ν, the energy dissipation rate per unit mass ϵ, and the scale R

2. In the limit as $Re \to \infty$, all small-scale statistical properties are uniquely determined by ϵ and R.

Since ϵ has dimensions of $[L^2T^{-3}]$ and R is the only available length scale according to the above assumptions, one can combine them to predict how various statistical quantities behave in the inertial range. For example, to estimate the structure functions of Eq. 5.8, dimensional arguments lead to

$$S_n(R) = C(\epsilon R)^{n/3}, \tag{5.10}$$

where C is a universal constant (SREENIVASAN, 1995). In particular, for $n = 2$, we recover what is known as the Kolmogorov $2/3$ law[4] (KOLMOGOROV, 1941)

$$S_2(R) = C(\epsilon R)^{2/3}, \tag{5.11}$$

A rather non-trivial issue in the study of turbulence is determining which statistical quantities, beyond the structure functions, are also relevant for characterizing the flow (BENZI; TOSCHI, 2023). The main idea is that we are dealing with a random, time-evolving velocity field. So, much like the approach taken in spin glass theory, it is natural to examine correlation functions. In particular, we are interested in correlations of the fluctuations in the energy dissipation rate $\epsilon(\mathbf{r}, t)$ relative to its mean value. We can define the deviation as

$$\delta\epsilon(\mathbf{r}, t) = \epsilon(\mathbf{r}, t) - \langle\epsilon\rangle\,, \tag{5.12}$$

and study how these fluctuations correlate over space using the correlation function $K_{\epsilon\epsilon}(R)$[5][6]

$$K_{\epsilon\epsilon}(R) = \langle\delta\epsilon(\mathbf{r} + \mathbf{R}, t)\delta\epsilon(\mathbf{r}, t)\rangle\,. \tag{5.13}$$

[4] We can also examine a Fourier representation of the energy spectrum, which leads to the well-known $-5/3$ power law (see (GONZÁLEZ, 2017))

[5] Note the similarity to Eq. 2.14.

[6] Strictly speaking, Eq. 5.13 defines a covariance function, since it is the ensemble average of the product of fluctuations without normalization. However, in turbulence literature, it is commonly referred to as a correlation function. The normalized version, bounded between -1 and 1, is obtained by dividing by $\langle\delta\epsilon^2(\mathbf{r}, t)\rangle$.

If the energy dissipation is uncorrelated between different points, Eq. 5.13 vanishes for all $R \neq 0$. Using Kolmogorov's dimensional reasoning, we obtain that (L'VOV; PROCACCIA, 1998)

$$K_{\epsilon\epsilon}(R) \sim \nu^2 \epsilon^{-4/3} R^{-8/3}, \tag{5.14}$$

meaning that the correlation decays as a power law in R proportional to $R^{-8/3}$. Indeed, experiments have demonstrated that many statistical quantities of turbulent flows exhibit a power-law dependence on R. Specifically, both the correlation functions and structure functions follow the scaling

$$K_{\epsilon\epsilon}(R) \sim R^{\mu} \quad \text{and} \quad S_n \sim R^{\zeta_n}, \tag{5.15}$$

However, there is a significant discrepancy between the exponents predicted by K41 and those observed in experiments. For instance, we have $\mu \approx 0.2$ (SREENIVASAN; KAILASNATH, 1993) and ζ_n deviating from $n/3$ as n increases (BENZI et al., 1993). One reason for this inconsistency lies in the assumption that only R and ϵ are relevant within the inertial range. In reality, both the large-scale length L and the small-scale η continue to influence the statistics even in this intermediate range. As a result, structure functions take a corrected form (L'VOV; PROCACCIA, 1998)

$$S_n(R) = C(\epsilon R)^{n/3} \left(\frac{L}{R}\right)^{n/3-\zeta_n}, \tag{5.16}$$

This deviation from simple dimensional analysis is known as anomalous scaling. The other reason why K41 is unable to fully describe turbulence is the presence of intermittency, an irregular and violent behavior of energy dissipation at small scales. K41 assumes (based on Taylor's work (TAYLOR, 1935)) that turbulence in the inertial range is statistically homogeneous, isotropic, and self-similar, i.e., turbulence is the same at every point in space, identical in all directions, and follows the same scaling laws across every scale. However, experiments and numerical simulations reveal that energy dissipation is not uniform but is concentrated in intense, localized structures. These include regions exhibiting sharp velocity gradients (shear layers) or zones of high fluid vorticity (vorticity filaments).

The existence of intermittency breaks the assumption of self-similarity and leads to non-Gaussian statistics (heavy tails) at small scales. To address this, Kolmogorov introduced a refined theory in 1962 (K62) (KOLMOGOROV, 1962) that assumes that the local dissipation rate

ϵ_r is not a constant, but a log-normally distributed function. This means that (BALAKRISHNAN; CHEN, 1999)

$$P(\epsilon_r) = \frac{1}{\epsilon_r \sqrt{2\pi\sigma^2}} \exp\left[-\frac{(\ln \epsilon_r - \mu)^2}{2\sigma^2}\right], \tag{5.17}$$

with μ and σ as the mean and standard deviation, respectively. K62 leads to a prediction for the variance σ^2 of $\ln(\epsilon_r)$ as (KOLMOGOROV, 1962)

$$\sigma^2_{\ln \epsilon_r}(\mathbf{x}, t) = A(\mathbf{x}, t) + k' \ln\left(\frac{L}{R}\right), \tag{5.18}$$

where $A(\mathbf{x}, t)$ is a function related to the macroscopic statistics of the flow, and k' is a universal constant known as the intermittency exponent (GONZÁLEZ, 2017). Eq. 5.18 directly controls how variable the dissipation is at scale R. We can see that σ^2 increases as the scale R decreases, meaning that dissipation becomes more intermittent at such smaller scales. K62 also corrects the R dependence exponents with

$$\zeta_n = \frac{n}{3} - \frac{k'}{18} n(n-3), \tag{5.19}$$

which introduces a nonlinear dependence in ζ_n, capturing the observed anomalous scaling of the structure functions. However, as $n \to \infty$, the quadratic term dominates, leading to negative (unphysical) exponents. This problem was observed, for example, in experiments by Anselmet et al. (1984). Moreover, the assumption of a log-normal distribution fails to accurately represent the tails of the probability distribution of the velocity increments, which are heavier than predicted, meaning that extreme events occur more frequently than the model allows.

Despite all of this, Kolmogorov's theory was influential enough to inspire more refined approaches. As a notable example, we have the multifractal model proposed by Parisi and Frisch (1985), which replaces the log-normal assumption with a spectrum $D(h)$ of fractal dimensions[7]. Among other remarkable theoretical frameworks, there is the dynamical model proposed by Salazar and Vasconcelos (2010), which describes energy transfer between contiguous scales using a set of coupled stochastic differential equations. Building upon this,

[7] Benoît Mandelbrot was the first to formally challenge the log-normal hypothesis (MANDELBROT, 1974). He introduced the multifractal idea, arguing that turbulence involves a continuous spectrum of singularities rather than a single Gaussian process.

the H-theory developed by Macêdo et al. (2017) generalizes the model and addresses several unresolved issues. In our analysis, we adopted and implemented this latter framework.

5.1.1 The H-theory dynamical model

The H-theory is a dynamical stochastic model based on Langevin equations with hierarchically separated time scales. It generalizes the Salazar–Vasconcelos model (SALAZAR; VASCONCELOS, 2010) and establishes a connection between the field of superstatistics — a branch of statistical physics dedicated to the study of non-linear and non-equilibrium systems — and stochastic processes (GONZÁLEZ, 2017). The main idea in the model is that even if a signal x (like wind speed or the intensity of a laser) may appear to be random and unpredictable, it can follow simple local rules influenced by slower, hidden processes. Instead of modeling the signal as a single complex entity, we can decompose it into mainly two components:

- A fast process: The observable signal x fluctuates rapidly, which can resembles a Gaussian noise over short timescales.
- A slow background process: The variance of these fluctuations is governed by a hidden variable ϵ, which evolves on a slower timescale.

In superstatistics, ϵ is just assumed to follow some distribution, but in H-Theory, we assume that ϵ itself is the result of multiple slower hidden processes, each influencing the next, like a chain of effects. The theory in fact determines the number N of relevant time scales. N basically tells us how many layers of hidden random processes affect the observed signal x. For example, in the previous section on turbulence, we said that large eddies break into smaller ones, which is a process naturally described by these multiple timescales. When $N = 0$, the system behaves like a simple Gaussian noise. For $N = 1$, there is only one background fluctuation, resulting in a distribution with heavier tails. When $N > 1$, multiple hierarchical layers produce increasingly complex, heavy-tailed, non-Gaussian statistics. Distributions with heavy tails often emerge from a composition of well-separated stochastic processes, each reaching local equilibrium at its own timescale. Solving the model in its stationary state yields the overall probability distribution that governs the long-term behavior of the signal.

Let us try to paint a simple picture of the theory. As commented before, on short timescales, x behaves like a Gaussian process with fixed variance ϵ, i.e., $P(x|\epsilon)$. However, ϵ fluctuates,

following some unknown probability distribution $f(\epsilon)$. So the full distribution of x is a weighted average over all possible variances (GONZÁLEZ, 2017)

$$P(x) = \int d\epsilon P(x|\epsilon) f(\epsilon). \tag{5.20}$$

This type of description matters because a single Gaussian cannot capture extreme events. However, if one combines many Gaussian curves with different variances, one can get heavy tails distribution. This is the starting point of superstatistics, and H-Theory takes it further by deriving $f(\epsilon)$ from dynamical equations, rather than just fitting it from some data (GONZÁLEZ, 2017). To this end, we start with a Langevin equation that describes how x evolves over time

$$dx = -\zeta x dt + \sqrt{2\zeta\epsilon_N} dV, \tag{5.21}$$

where ζ is a positive constant, dV is a Wiener process (also called Brownian motion or white noise), which represents random fluctuations, and ϵ_N[8] is a random variable that, by the time we observe the system, has settled into a local equilibrium and no longer changes significantly over time. The first term on the right-hand side of the Langevin equation (Eq. 5.21) corresponds to the dissipation (or drift). This term removes energy from the system and pulls the variable x back toward equilibrium over time. The second term is the stochastic component (noise), determining the strength and influence of random fluctuations.

We can also describe how each background variable ϵ_i evolves over time by a Langevin equation, which takes the general form of (GONZÁLEZ, 2017)

$$d\epsilon_i = F_i(\epsilon_0, \ldots, \epsilon_N, t)dt + G_i(\epsilon_0, \ldots, \epsilon_N, t)dW_i. \tag{5.22}$$

Here, ϵ_i is the i-th background variable in the hierarchy that is influenced by even slower processes ϵ_{i-1} (with well-separated time scales). dW_i a Wiener process that is independent for each i (a single layer has its own randomness). F_i and G_i are general functions that could depend on time t and on all background variables.

To determine the specific form of F_i and G_i, H-theory employs the following constraints, motivated by the cascade model of classical turbulence:

[8] ϵ_N is the last background variable in the hierarchy of $\epsilon_0, \epsilon_1, \ldots, \epsilon_N$

1. Temporal Translation Symmetry: The rules governing the system are time-invariant, i.e., the dynamics are assumed to be stationary and do not depend on time. Mathematically

$$\frac{\partial F_i}{\partial t} = \frac{\partial G_i}{\partial t} = 0. \tag{5.23}$$

2. Local Interactions: Each variable ϵ_i is only influenced by its immediate neighbor in the hierarchy. This reflects the idea of locality in turbulence, i.e., the energy is transferred between adjacent scales, not across distant ones. So,

$$F_i(\epsilon_0, \ldots, \epsilon_N) = F_i(\epsilon_{i-1}, \epsilon_i),$$
$$G_i(\epsilon_0, \ldots, \epsilon_N) = G_i(\epsilon_{i-1}, \epsilon_i). \tag{5.24}$$

3. Scale Invariance: The dynamics of the system has no preferred scale. If all energies are multiplied by a factor λ, the form of the equations remains unchanged. Then

$$F_i(\lambda\epsilon_{i-1}, \lambda\epsilon_i) = \lambda F_i(\epsilon_{i-1}, \epsilon_i),$$
$$G_i(\lambda\epsilon_{i-1}, \lambda\epsilon_i) = \lambda G_i(\epsilon_{i-1}, \epsilon_i). \tag{5.25}$$

4. Stationary Condition: If two consecutive layers in the hierarchy are equal, then there's no net change — the system is in equilibrium at that scale. This ensures that the system can relax into a steady state, where the average flow of energy (or variance) between scales becomes zero when the levels match. In mathematical terms

$$\epsilon_i = \epsilon_{i-1} \Rightarrow \left\langle \frac{d\epsilon_i}{dt} \right\rangle = 0. \tag{5.26}$$

5. Unidirectional Flux: This ensures that each ϵ_i remains positive over time. This is obvious since the variance cannot be negative. Therefore,

$$\text{If } \epsilon_i(t=0) \geq 0 \Rightarrow \text{Prob}(\epsilon_i < 0) = 0. \tag{5.27}$$

The most general forms of F_i and G_i that fulfill all the above conditions were derived by González (2017) and are given by

$$F_i(\epsilon_0, \ldots, \epsilon_N, t) = -\gamma_i(\epsilon_i - \epsilon_{i-1}),$$
$$G_i(\epsilon_0, \ldots, \epsilon_N, t) = \kappa_i \epsilon_i^{\alpha} \epsilon_{i-1}^{1-\alpha}, \tag{5.28}$$

where γ_i, κ_i, and α are positive constants. Inserting Eq. 5.28 into Eq. 5.22 leads to

$$d\epsilon_i = -\gamma_i(\epsilon_i - \epsilon_{i-1})dt + \kappa_i \epsilon_i^{\alpha} \epsilon_{i-1}^{1-\alpha} dW_i. \tag{5.29}$$

The exponent α plays an important role in determining the statistical behavior of ϵ_i. Only two values ($\alpha = 1$ or $\alpha = 1/2$) lead to physically meaningful and solvable analytic expressions for the corresponding Fokker-Planck equation (GONZÁLEZ, 2017). When $\alpha = 1$, the stationary distribution of ϵ_i has the form of an Inverse Gamma distribution, often observed in systems with heavier tails. On the other hand, when $\alpha = 1/2$, the solution becomes a Gamma distribution, which describes systems with lighter, stretched exponential tails.

5.1.2 Solving the model and numerical approach

Naturally, the next step here would be to solve the full multiscale stochastic model (Eqs.5.21 and 5.29) and derive a closed-form expression for the stationary distribution $P(x)$ (Eq. 5.20). In H-theory, both $P(x)$ and the background variance distribution $f(\epsilon)$ admit exact solutions in terms of Meijer G-functions[9] (or, in more complex situations, Fox H-functions[10]). These special functions emerge naturally from the nested integrations over each Langevin equation. However, in our system, analysis showed that only a single background scale is relevant ($N = 1$), and that the distribution $f(\epsilon)$ fits well in an Inverse Gamma distribution. This result simplifies the hierarchy to the first level, so the solutions of our problem ease to a much simpler form. It is worth noting that we also observe regimes without turbulence, corresponding to $N = 0$ (no multiscale cascade with purely Gaussian statistics). In light of this, we present here only the $N = 1$ and $\alpha = 1$ results of the multiscale approach. For a full derivation of the multiscale model and its Meijer G or Fox H solutions, the reader is referred to González's thesis (GONZÁLEZ, 2017) and to the original work on turbulence in random lasers (GONZÁLEZ et al., 2017).

One should bear in mind that determining the correct value of N is not a trivial task. The standard procedure involves fitting the general N-dependent Meijer G-function to the data and systematically varying N (and other relevant parameters). The optimal number of scales is then selected based on which value yields the best agreement to the data. This agreement

[9] A very general class of function designed to embrace most known special functions, such as Gamma and Bessel functions, as a specific case.
[10] Generalization of the Meijer G-function.

is typically confirmed by minimizing the error via the least squares method. A similar fitting procedure is applied to $f(\epsilon)$, testing whether a gamma or inverse-gamma distribution provides a better description of the data.

Setting the dynamics at a single scale ($\epsilon_N = \epsilon_1 = \epsilon$) leads the stochastic equations to take the form

$$dx = -\zeta x dt + \sqrt{2\zeta\epsilon} dV, \tag{5.30}$$

$$d\epsilon = -\gamma(\epsilon - \epsilon_0)dt + \kappa g(\epsilon) dW; \quad g(\epsilon) = \epsilon^{\alpha}\epsilon_0^{1-\alpha}. \tag{5.31}$$

By solving the associated Fokker-Planck equations in the stationary limit ($t \to \infty$) and setting $\alpha = 1$, we obtain the conditional probability distribution $P(x|\epsilon)$

$$P(x|\epsilon) = \frac{1}{\sqrt{2\pi\epsilon}} \exp\left(-\frac{x^2}{2\epsilon}\right), \tag{5.32}$$

and the background distribution

$$f(\epsilon) = \frac{(\beta\epsilon_0)^{\beta+1}}{\Gamma(\beta+1)} \epsilon^{-\beta-2} \exp\left(-\frac{\beta\epsilon_0}{\epsilon}\right); \quad \epsilon > 0. \tag{5.33}$$

Here, Γ is the gamma function, and $\beta = 2\gamma/\kappa^2$, which is always greater than zero. The parameter β is adjusted to fit the data and determines the shape of the distribution. With these expressions, we can derive the full probability distribution $P(x)$. Using Eq. 5.20 and the equations above

$$P(x) = \int d\epsilon \left[\frac{1}{\sqrt{2\pi\epsilon}} \exp\left(-\frac{x^2}{2\epsilon}\right)\right] \left[\frac{(\beta\epsilon_0)^{\beta+1}}{\Gamma(\beta+1)} \epsilon^{-\beta-2} \exp\left(-\frac{\beta\epsilon_0}{\epsilon}\right)\right],$$

$$P(x) = \frac{(\beta\epsilon_0)^{\beta+1}}{\sqrt{2\pi}\Gamma(\beta+1)} \int_0^{\infty} d\epsilon \frac{\epsilon^{-\beta-2}}{\sqrt{\epsilon}} \exp\left(-\frac{x^2}{2\epsilon} - \frac{\beta\epsilon_0}{\epsilon}\right),$$

$$P(x) = \frac{(\beta\epsilon_0)^{\beta+1}}{\sqrt{2\pi}\Gamma(\beta+1)} \int_0^{\infty} d\epsilon \epsilon^{-(\beta+\frac{5}{2})} \exp\left[-\frac{1}{\epsilon}\left(\frac{x^2+2\beta\epsilon_0}{2}\right)\right]. \tag{5.34}$$

Let us simplify the integration process by defining the constants:

$$A = \frac{(\beta\epsilon_0)^{\beta+1}}{\sqrt{2\pi}\Gamma(\beta+1)}, \qquad B = \left(\frac{x^2+2\beta\epsilon_0}{2}\right). \tag{5.35}$$

With these, Eq. 5.34 becomes

$$P(x) = A\int_0^\infty d\epsilon \epsilon^{-\left(\beta+\frac{5}{2}\right)} \exp\left(-\frac{B}{\epsilon}\right). \tag{5.36}$$

This integral is easily solved using the substitution

$$\epsilon = \frac{B}{u} \Longrightarrow d\epsilon = -\frac{B}{u^2}du, \tag{5.37}$$

with the limits changing accordingly

$$\begin{cases} \epsilon \to 0 \Rightarrow u \to \infty \\ \epsilon \to \infty \Rightarrow u \to 0 \end{cases}.$$

Substituting into the integral, we obtain

$$P(x) = -A\int_\infty^0 du \frac{B}{u^2}\left(\frac{B}{u}\right)^{-\left(\beta+\frac{5}{2}\right)} \mathsf{e}^{-u},$$

$$P(x) = AB^{-\left(\beta+\frac{3}{2}\right)}\int_0^\infty du u^{\beta+\frac{1}{2}}\mathsf{e}^{-u}. \tag{5.38}$$

We now identify the integral as the Gamma function

$$\Gamma(z+n+1) = \int_0^\infty dt t^{z+n}\mathsf{e}^{-t}, \tag{5.39}$$

so that

$$P(x) = AB^{-\left(\beta+\frac{3}{2}\right)}\Gamma\left(\beta+\frac{3}{2}\right). \tag{5.40}$$

Substituting back the original expressions for A and B and reorganizing the constants, we get

$$P(x) = \frac{(\beta\epsilon_0)^{\beta+1}}{\sqrt{2\pi}\Gamma(\beta+1)}\left(\frac{x^2+2\beta\epsilon_0}{2}\right)^{-\left(\beta+\frac{3}{2}\right)}\Gamma\left(\beta+\frac{3}{2}\right),$$

$$P(x) = \frac{1}{\sqrt{2\pi}}\frac{\Gamma(\beta+3/2)}{\Gamma(\beta+1)}\left(\beta\epsilon_0\right)^{\beta+1}\left(\beta\epsilon_0\right)^{-\beta-\frac{3}{2}}\left(\frac{x^2}{2\beta\epsilon_0}+1\right)^{-\left(\beta+\frac{3}{2}\right)},$$

$$P(x) = \frac{1}{\sqrt{2\pi\beta\epsilon_0}} \frac{\Gamma(\beta + 3/2)}{\Gamma(\beta + 1)} \left(1 + \frac{x^2}{2\beta\epsilon_0}\right)^{-\left(\beta+\frac{3}{2}\right)} . \tag{5.41}$$

This final expression gives the analytical form of the probability distribution $P(x)$ for our signal, under the use of an inverse-gamma background with a single scale ($N = 1$). When working with experimental data series, the parameter ϵ_0 is chosen such that the background distribution has a fixed mean $\langle\epsilon\rangle = \epsilon_0 = 1$, so that ϵ_0 is not a free parameter and β is the only value to be fit. Alternatively, $P(x)$ can be written in terms of the so-called q-Gaussian distribution, which is a generalization of the Gaussian distribution. The q-Gaussian has the form (VASCONCELOS et al., 2024)

$$P(x) = \sqrt{\frac{q-1}{\pi(5-3q)\epsilon_0}} \frac{\Gamma\left(\frac{1}{q-1}\right)}{\Gamma\left(\frac{1}{q-1} - \frac{1}{2}\right)} \exp_q\left[-\frac{x^2}{(5-3q)\epsilon_0}\right], \tag{5.42}$$

where

$$q = 1 + \frac{2}{2\beta + 3}, \tag{5.43}$$

and

$$\exp_q(x) \equiv [1 + (1-q)x]^{\frac{1}{1-q}} . \tag{5.44}$$

To verify the compound hypothesis in Eq. 5.20, González (2017) introduced a numerical method to extract the background distribution directly from the signal's time series[11]. The idea is very straightforward: if we can reconstruct $f_N(\epsilon_N)$ from data, we can test the validity of the theory by comparing the reconstructed distribution with the one predicted by the model. So, the goal is to identify the background fluctuation series $\epsilon(t)$ which, when mixed with Gaussian noise, reproduces the observed $P(x)$. But how exactly can we determine this background series?

As already mentioned, the moments are the statistical identifiers of a distribution. If the data appears non-Gaussian, it is because the variance is fluctuating. While we do not directly observe the background variance distribution $f(\epsilon)$, we can measure the moments of the signal x, which — fortunately — are mathematically related to the moments of the hidden background ϵ via

[11] This is the method chosen for our analysis.

$$\left\langle x^{2p} \right\rangle = \langle \epsilon^p \rangle \prod_{k=1}^{p} (2p-1). \tag{5.45}$$

From this relation, we see that the first and second moments of ϵ are

$$p = 1 \Rightarrow \langle \epsilon \rangle = \left\langle x^2 \right\rangle, \tag{5.46}$$

$$p = 2 \Rightarrow \left\langle \epsilon^2 \right\rangle = \frac{\langle x^4 \rangle}{3}. \tag{5.47}$$

We also can define the central moment (moment about the mean) of the signal as

$$\mu_n(x) = \left\langle (x - \langle x \rangle)^2 \right\rangle. \tag{5.48}$$

We are particularly interested in the variance and kurtosis of the signal, which correspond to the first two moments of the background series. These are related to the central moments by

$$\sigma^2(x) = \mu_2(x), \tag{5.49}$$

$$\kappa(x) = \frac{\mu_4(x)}{[\mu_2(x)]^2}. \tag{5.50}$$

To simplify, we set the signal x to have zero mean ($\langle x \rangle = 0$), which causes $\mu_n(x) = \langle x^n \rangle$. Additionally, we also set the signal to have unit variance, so $\sigma^2(x) = \mu_2(x) = \langle x^2 \rangle = 1$. The kurtosis simply becomes $\kappa(x) = \langle x^4 \rangle$. With these simplifications, and using Eqs. 5.46 to 5.50, we can derive the variance of the background series ϵ as

$$\sigma^2(\epsilon) = \left\langle (\epsilon - \langle \epsilon \rangle)^2 \right\rangle,$$

$$\sigma^2(\epsilon) = \left\langle (\epsilon - 1)^2 \right\rangle,$$

$$\sigma^2(\epsilon) = \left\langle \epsilon^2 \right\rangle - 1,$$

$$\sigma^2(\epsilon) = \frac{\kappa(x) - 3}{3} = \frac{\gamma_2(x)}{3}. \tag{5.51}$$

Eq.5.51 shows that we can use the kurtosis of the signal to detect signs of turbulence. If $\kappa = 3$, then $\sigma^2(\epsilon) = 0$, implying no background fluctuation and purely Gaussian statistics.

However, if $\kappa > 3$, then $\sigma^2(\epsilon) > 0$, indicating that the variance fluctuates, which leads to heavy-tailed distributions composed of Gaussian curves with different variances. Conversely, if $\kappa < 3$, the variance fluctuations are suppressed relative to a Gaussian, leading to light-tailed, platykurtic distributions with a flatter peak than a standard Gaussian. With this in mind, we aim to construct a background series whose variance matches the theoretical value given by Eq.5.51.

The method for constructing $\epsilon(t)$ is described as follows:

1. Construct the fluctuations series: We construct the fluctuation series (similar to Eq. 5.6) by calculating the difference between points separated by an interval τ. In general, the signal is defined as

$$x(t) = u(t+\tau) - u(t); \quad \tau \in \mathbb{N}^*. \tag{5.52}$$

   Since the time t is a discrete variable here, it refers to the ordered sequence of data acquisition $\{t_0, t_S\}$ (S being the total number of samples). Thus, τ represents the number of steps between consecutive samples: $\tau = 1$ corresponds to the first neighbor, $\tau = 2$ to the second, and so on. We will restrict our analysis to $\tau = 1$, as it has been shown that for larger values of τ, the system tends to return to a Gaussian distribution (GONZÁLEZ, 2017; GONZÁLEZ et al., 2018).

2. Normalize the signal: We apply the same simplification used earlier (zero mean and unit variance[12]). This is done by computing

$$\tilde{x}(t) = \frac{x(t) - \langle x(t) \rangle}{\sigma(x(t))}. \tag{5.53}$$

3. Compute local variance: We subdivide the signal into intervals of size M and compute the variance within each interval

$$\epsilon_M(t) = \frac{1}{M} \sum_{j=0}^{M-1} \left[x(t - j\delta t) - \langle x_M(t) \rangle \right]^2. \tag{5.54}$$

   where $t = 1, 2, \ldots, S$ and $\langle x_M(t) \rangle$ is the local mean over M elements of the data series

$$\langle x_M(t) \rangle = \frac{1}{M} \sum_{j=0}^{M-1} x(t - j\delta t). \tag{5.55}$$

   This process generates a new time series using a technique known as the running average. The initial value of M is chosen based on the result from Eq. 5.51.

Figure 25 – Flowchart of the numerical procedure used to reconstruct the background variable ϵ_M and compute the probability distribution $P(x)$ from empirical data. Alternatively, one can also use a loop to iterate over different values of M to determine which value provides the best result, rather than applying the variance as a criterion.

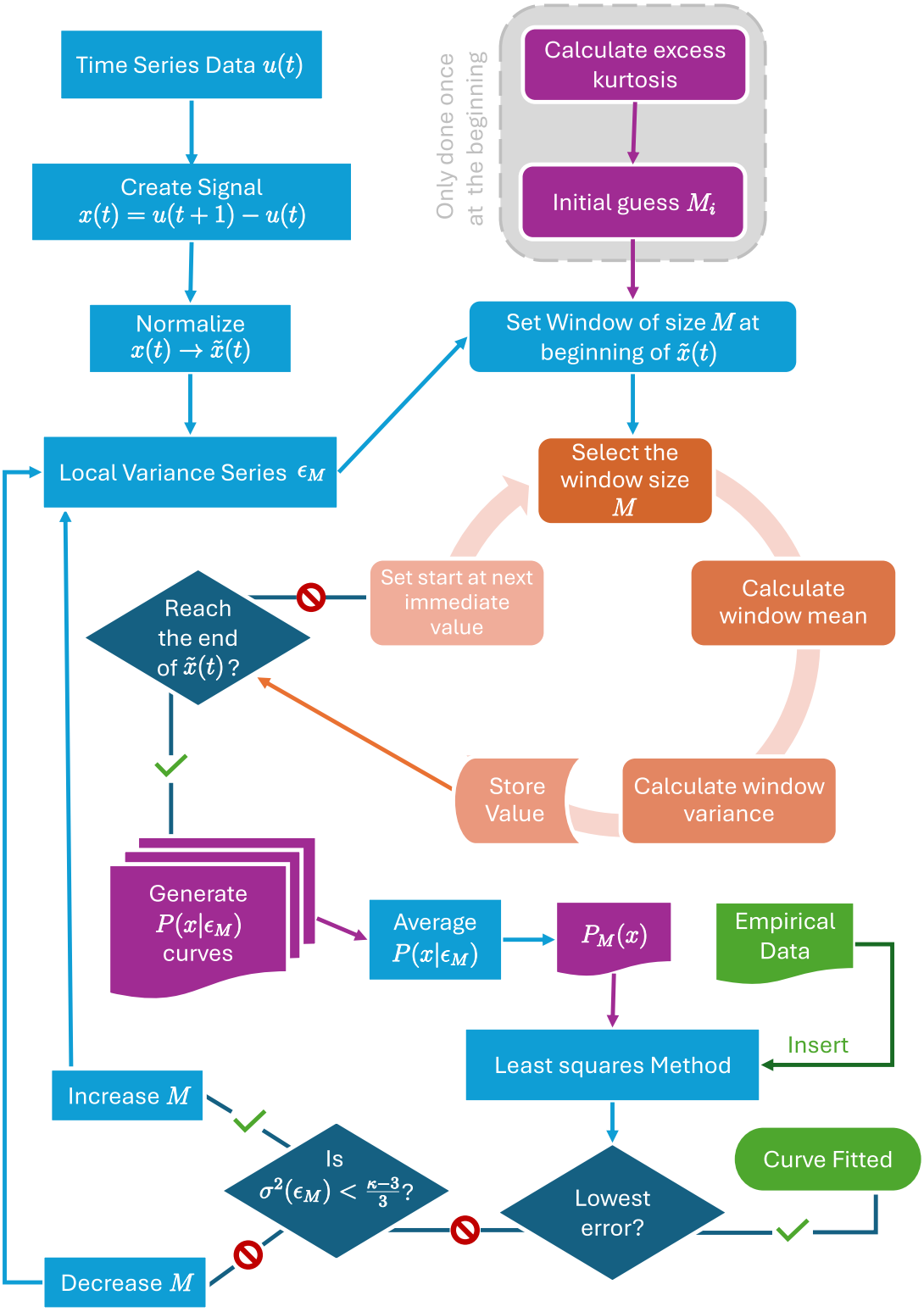

Source: The Author (2025)

In hold of this background series, we now numerically compound it with the Gaussian kernel (Eq.5.32), as suggested by Eq.5.20, for various values of M. In other words, we use

$$P(x|\epsilon_M) = \frac{1}{\sqrt{2\pi\epsilon_M}} \exp\left(-\frac{x^2}{2\epsilon_M}\right) \tag{5.56}$$

to generate a curve of $P(x|\epsilon_M)$ for each value of ϵ_M. We then take the average of all these curves. The resulting distribution is $P(x)$, which is than compared with the empirical one using the least squares method. Since the initial value of M comes from an ideal mathematical relation, we adjust M (increasing or decreasing it from the initial guess) to minimize the fitting error. We can also guide this adjustment using $\sigma^2(\epsilon_M)$: if $\sigma^2(\epsilon_M)$ is smaller than the theoretical value from Eq. 5.41, we increase M; if it is greater, we decrease M.

This gives us a reliable method to compute $P(x)$ and compare it with the theoretical fit given by Eq. 5.41. Fig. 25 presents a flowchart outlining all the numerical steps described above. It is also important to emphasize that, once the reconstructed background series ϵ_M is obtained, its distribution should match well with Eq. 5.33, using the parameters previously determined.

5.2 MULTIVARIATE ANALYSIS FOR THE SIGNAL

Now that we have established a solid theoretical framework to describe the turbulent dynamics of our system, a practical question arises: how can we determine the signal series $x(t)$ for our analysis?

In the previous chapter, we investigated the dynamics of the peaks in the spectrum to identify the L-shaped distributions, which were indicative of unusual dynamics. Therefore, it is natural to consider if those same peaks can reveal signatures of turbulent dynamics. However, we are faced with a critical limitation: turbulence analysis requires significantly more data (at least two orders of magnitude more) than what was used in the RSB study (GONZÁLEZ et al., 2017). Consequently, we cannot reuse the previously available dataset and we must obtain new data within the QML region. With the acquisition of new data, we find that the positions of the peaks are not constant, as they initially appeared to be. Instead, peaks fluctuate within a narrow window of wavelengths (or frequencies). This window is constrained by the spectral width of the SML regime. Since the SML spectrum is broader than the QML spectrum, and

[12] Note that normalizing the standard deviation σ also normalizes the variance, since $\sigma(x) = \sqrt{\text{Var}(x)}$.

the frequencies present in the QML regime are precisely those that compose the mode-locking (see Sec. 4.2), the possible peak positions in QML are effectively a subset of the SML spectrum bandwidth.

The heatmap in Fig. 26 illustrates the average spectrum at different pump powers in the QML region. We can clearly see that the peaks 'wiggle' across wavelengths as the pumping is varied. It is also clear that the number of peaks is not constant, and it differs from two for different pumping powers.

Figure 26 – Heatmap of the averaged spectrum in the QML region. Each row represents a top-view projection of the averaged spectrum, obtained by averaging over 150,000 individual spectra for each pumping value.

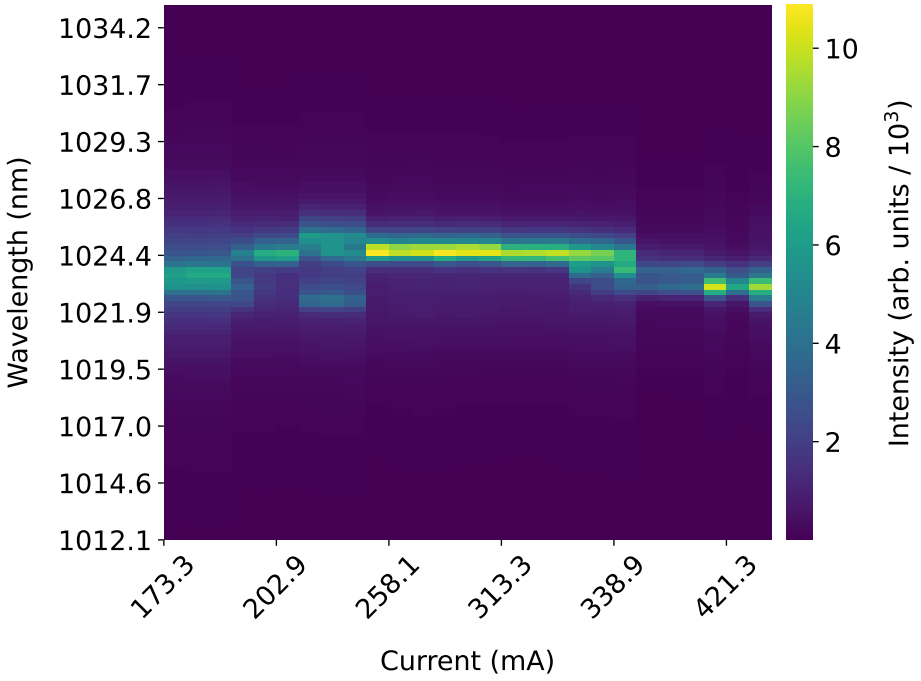

Source: The Author (2025)

This variability can be attributed to the cavity configuration, particularly the angles of the polarization waveplates, which are mainly the variable elements in our setup. Since multiple waveplate configurations can still achieve mode-locking operation (CAMPOS, 2020), different realizations of the QML regime are possible, each exhibiting its own peak structure.

We could consider identifying the most frequently occurring peaks across the entire region and fixing to those, or perhaps simply choosing the global maximum of each spectrum. However, this approach presents a new complication.

As shown in Fig. 27, the moments of the signal (variance and kurtosis) indicate that the peak dynamics fluctuate between Gaussian and non-Gaussian behavior throughout the region.

Figure 27 – Variance (σ^2) and kurtosis excess ($\gamma_2 = \kappa - 3$) of the intensity difference time series for the two most frequent peaks and for the global maximum, across different values of the pumping current. The QML region spawns approximately from 180 mV to 477 mV, with the CW and SML regimes lying before and after this range, respectively. The wavelengths of the two most frequent peaks are $\lambda_1 = 1022.9$ nm and $\lambda_2 = 1024.4$ nm.

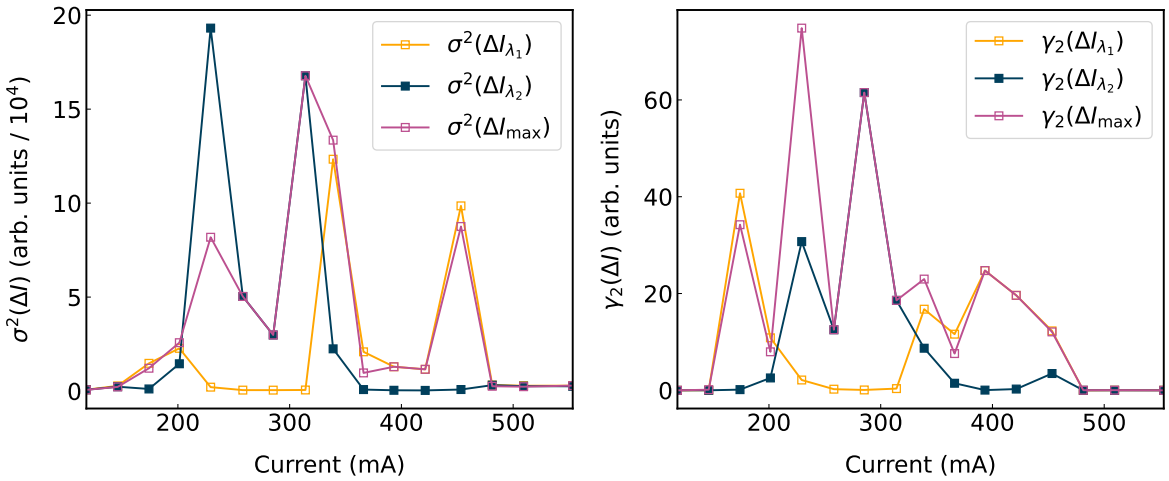

Source: The Author (2025)

That is, since the number of peaks is not constant, the two most frequent peaks may not correspond to competing modes at a given pumping value. Thus, selecting the most frequent peaks does not necessarily capture the competing dynamics as done in previous analyses. Similarly, selecting only the maximum peak consistently excludes the dynamics of the other modes. At different parts, the maximum may follow one peak, the other, or neither of them.

The key to constructing the signal lies in recognizing that the system's dynamics are not confined to a single peak — or even just a set of peaks. The spectrum is composed of multiple points, each contributing to the overall behavior of the system. Selecting only one of them fails to capture the full picture, revealing only a partial and possibly misleading view of the dynamics.

A simple analogy to illustrate this situation can be done with the help of Fig. 28. Consider you have an apple, an ink stamp pad, and a piece of paper. If you press the bottom of the apple against the ink pad and then onto the paper, you obtain the image shown in Fig. 28a. Next, suppose you slice the apple horizontally, press the exposed surface into the pad, and stamp again. The result would be Fig. 28b. Finally, instead of a horizontal cut, suppose you make a vertical cut and repeat the stamping process, producing Fig. 28c. Now, you present these three stamped images in sequence to a random person (who did not see what you did) and ask them to identify the object from the images. They would most likely only recognize

Figure 28 – Representation of apple stamps on paper with (a) the bottom of the apple, (b) a horizontal cross-section, and (c) a vertical cross-section.

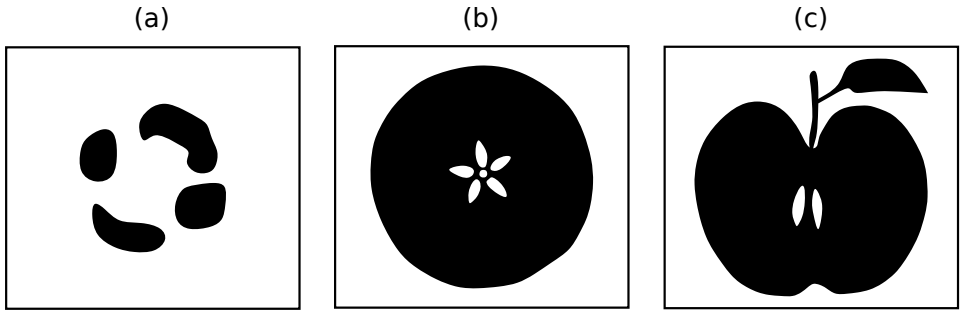

Source: The Author (2025)

the object as an apple upon seeing the third image. Despite all three stamps originating from the same object, the third picture is the one that has the most familiar shape.

This analogy encapsulates our challenge. By selecting a single mode, we are effectively looking at a poor imprint of the full system, one that lacks the features needed to reveal its complete structure. As a result, we cannot properly interpret the statistical signatures observed in Fig. 27. Therefore, what we need is the equivalent of the "best cut" of the apple, a representation that carries the richest information about the full turbulent dynamics. In other words, we must perform a multivariate analysis to extract a representative signal $x(t)$.

Multivariate analysis involves the statistical treatment of datasets in which each observation consists of multiple variables or features — in our case, a spectrum with many sets of modes. This approach is important when the dynamics come from the interplay between these variables. The primary goal is to understand the relationships between these variables and how they interact with each other. Among the available techniques, the most suitable for our system is Principal Component Analysis (PCA). PCA reduces the dimensionality of the dataset by transforming it into a new set of orthogonal variables (principal components) that capture most of the information in the data.

5.2.1 Principal Component Analysis (PCA)

Suppose we are performing an experiment, such as analyzing the flow of a fluid in a pipe. We divide the pipe into sections δ_i, and for each section, we measure the velocity squared and the pressure of the fluid - since we have learned a bit of fluid dynamics, we know that there can be a quadratic dependence of the velocity on the pressure. We then organize all the

collected data into a table like the one below.

Table 1 – Fictional data collected from an experiment analyzing the flow of a fluid in a pipe.

Pipe section	δ_1	δ_2	...	δ_n
$v^2(\mathrm{m}^2/\mathrm{s}^2)$	329.16	161.85	...	3.9
Pressure (PSI)	39.13	40.99	...	59.69

Source: The Author (2025)

To analyze this data, the most straightforward approach is to create a plot where the axes represent velocity squared and pressure. Each point on the graph corresponds to a different section of the pipe. We may obtain something similar to what is represented in Fig. 29, where we are able to identify some patterns, allowing us to identify regions of the pipe with similar properties or even possibly deduce empirical relationships between the variables.

Figure 29 – Graphical representation of velocity squared versus pressure plane of fictional data from an experiment analyzing fluid flow in a pipe. The heatmap indicate the section of the pipe.

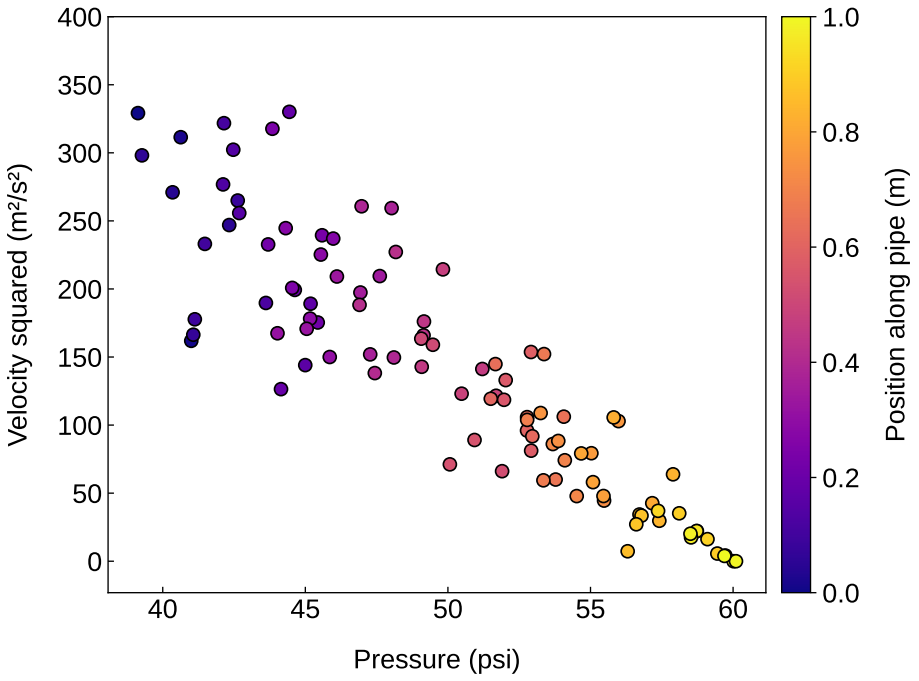

Source: The Author (2025)

However, being meticulous experimentalists, we decide to expand the scope of our measurements. Now, for each section of the pipe, we also record temperature, density, cross-sectional area, flow rate, and so on. Our experimental table now contains m rows, each one corresponding to a different type of measurement. With just two variables, it was simple to visualize

the data in a two-dimensional plot, but now, a graphical representation would require an m-dimensional space, which is impossible to visualize. Moreover, since we do not know the correct path to take, it is not clear which of the measured variables are the most relevant, making it difficult to discard any of them.

This type of challenge is common in experiments across all fields, and it is precisely here that PCA becomes useful. PCA constructs a new coordinate system (new axes) that allows us to re-express the data. The goal is to project the original dataset onto a new basis that filters out the noise and highlights hidden patterns and structure (SHLENS, 2014). In other words, we want to reduce the variables without losing information. We will now give an intuitive overview of PCA, followed later by a more formal mathematical description.

Figure 30 – Illustration of the basic steps of PCA: (1) normalize the data to have zero mean; (2) fit a line through the data points; (3) project each point onto the line and maximize the projected distances from the origin; (4) define the first principal component and its eigenvector; (5) find the second principal component orthogonal to the first; (6) project data onto the new axes to reveal patterns and effectuate analysis.

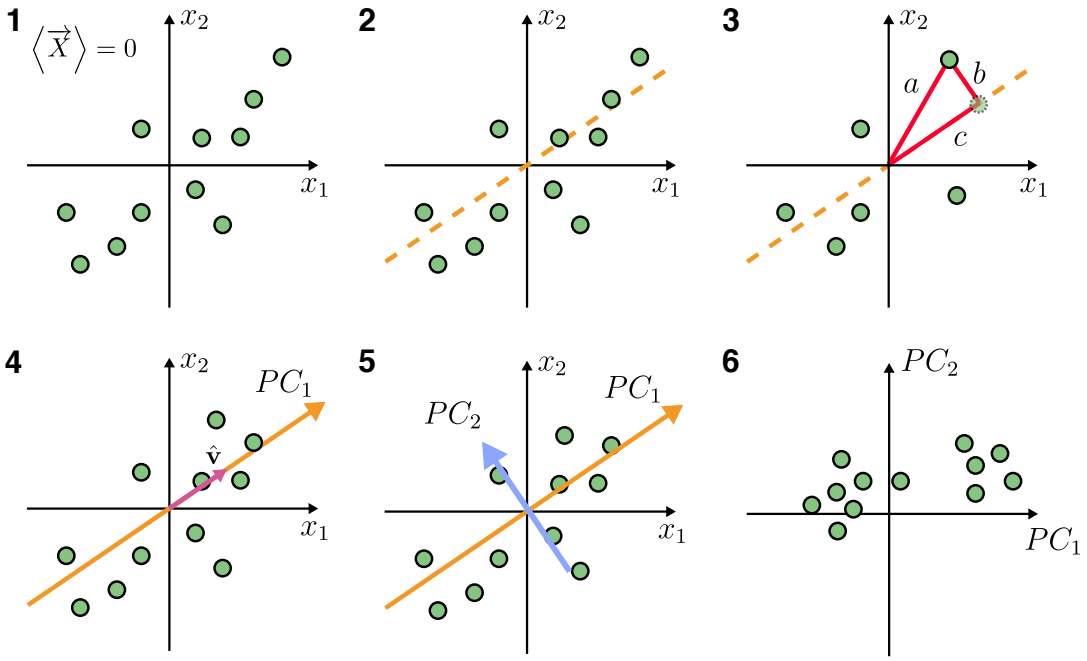

Source: The Author (2025)

Fig. 30 provides a visual representation of the basic steps involved in PCA. Let us begin with the simplest case, involving only two variables, just like in the introduction of this subsection. In this case, a single measurement i of our data matrix $\mathbf{X}$ can be represented as a column vector

$$X_i = \begin{bmatrix} x_{1i} \\ x_{2i} \end{bmatrix}. \tag{5.57}$$

This allows us to plot the data in a two-dimensional plane where the axes correspond to measurement types x_1 and x_2 (Fig. 29).

We now present a step-by-step explanation of how PCA works, using Fig. 30 as a visual guide. The first step in PCA (#1 in Fig. 30) is to normalize the data so that it has zero mean. This is done by calculating the average of each row (i.e., each variable) and subtracting it from the dataset. As a result, the cloud of points becomes centered around the origin. Once the data is centered, the next step (#2 in Fig. 30) is to fit a line that passes through the points and the origin. Naturally, we may ask: how do we determine the best line? In PCA, this is done by projecting each data point onto a random candidate line and selecting by rotation the one for which the sum of the squared projection lengths is maximized.

To better understand this, consider a data point at a fixed distance a from the origin (#3 in Fig. 30). If we project this point onto a line, the projection forms a right triangle with the origin. In this triangle, the perpendicular distance from the point to the line is b, and the length of the projection along the line is c. From the Pythagorean theorem, we have $c = \sqrt{a^2 - b^2}$. Since a is constant for each point, maximizing the projection is finding the maximum value of c, which is equivalent to minimizing b. Thus, the best-fitting line is the one that maximizes the total projected distances

$$\arg\max \left(\sum_i c_i^2 \right). \tag{5.58}$$

In other words, we are maximizing the total projected variance. This direction of maximum variance corresponds to what we call the first Principal Component (PC), or PC1[13]. PC1 is, in fact, a linear combination of the original variables x_1 and x_2, and its slope s indicates the relative contribution of each variable. We can express this direction as a vector

$$\mathbf{v} = \begin{bmatrix} 1 \\ s \end{bmatrix}, \tag{5.59}$$

which, upon normalization, we obtain

[13] Determining the principal component is like choosing the best angle to slice the apple in our stamp analogy. PC1 shows the direction that captures the most information — just as the vertical cut gives the clearest representation of the apple's shape.

$$\frac{\mathbf{v}}{\|\mathbf{v}\|} = \widehat{\mathbf{v}} = \frac{1}{\sqrt{1+s^2}} \begin{bmatrix} 1 \\ s \end{bmatrix}. \tag{5.60}$$

This normalized vector is known as the singular vector or eigenvector associated with PC1 (#4 in Fig. 30). Its components are often referred to as the loadings. These loadings quantify how much each original variable contributes to the PC. Once identified PC1, we proceed to determine the second PC (PC2) (#5 in Fig. 30). We determine PC2 in a way that it must be orthogonal to PC1. This orthogonality condition ensures that PC2 captures a different aspect of the data, independent of the first. Also, no further optimization is required to find this second axis, since its direction is uniquely determined once PC1 is known. Just like the first component, PC2 also has an associated singular vector with its own loadings. Together, these two vectors form a new basis for the data space.

At this point, we can now re-express our data by projecting it onto the new basis formed by PC1 and PC2 (#6 in Fig. 30). The coordinates of the data points in this rotated basis are known as the scores. These scores represent the same observations, but now described in terms of their alignment with the principal components rather than the original variables. Projecting the data in this way allows us to identify structures that may have been hidden in the original coordinate system, such as clusters, trends, or outliers. In particular, clusters of points in this space suggest that these observations share similar characteristics across the original variables.

For the case when we have more than two variables (e.g., m variables) the procedure generalizes. We find PC1 with the hyperplane which maximizes the variance, and then determine $(m-1)$ PCs, all hyperplanes orthogonal to each other, and each associated with a singular vector and a corresponding eigenvalue. However, we said earlier that PCA is a dimensional reduction technique, so how can we start with m variables and finish with the same amount? The key insight of PCA is that not all components are equally important. The PCs are ranked by the amount of variance they explain in the data. PC1 explains the most variance, followed by PC2, then PC3, and so on. This ranking allows us to reduce the dimension effectively. Although we end up with m components, in practice we often retain only the first few ones because they capture most of the variance (and hence most of the information) in the data. This makes PCA particularly valuable for visualization and noise reduction.

To evaluate how many components we have to keep, we use a scree plot, where the x-axis shows the component index (PC1, PC2, etc.), and the y-axis displays the amount of

variance explained. We can also look at the cumulative variance plot, which shows the total variance explained by the first k components. A common rule of selection is to retain enough components to explain at least 70% of the total variance (JOLLIFFE; CADIMA, 2016). Let us apply PCA in our toy experiment of the flow of a fluid in a pipe. We represent the pressure and the velocity squared as p and v^2, respectively. The first and second singular vectors are

$$\begin{bmatrix} v_1 \\ v_2 \end{bmatrix} = \begin{bmatrix} -0.0588 & 0.9983 \\ 0.9983 & 0.0588 \end{bmatrix} \begin{bmatrix} p \\ v^2 \end{bmatrix}. \tag{5.61}$$

PC1 is almost entirely aligned with the velocity (or velocity squared, to be more precise), with a loading of 0.9983, while the pressure contributes very little (-0.0588). This means PC1 captures the majority of the variation in the velocity. As for PC2, it captures the remaining variation, mostly from the pressure (loading 0.9983). PCA effectively rotates the coordinate system to align with directions of maximum variance. In this case, since the velocity dominates the variation, PC1 aligns with it.

We can confirm this by looking at the bar graph and score plot in Fig. 31. The bar graph (Fig. 31a) shows that PC1 accounts for over 99.9% of the total variance, meaning the dataset can be basically represented one-dimensionally. The scores (Fig. 31b) are spread almost entirely along the PC1 axis, indicating that the velocity is the dominant factor.

Figure 31 – PCA for the fictional fluid flow experiment, where (a) shows the scree plot of the variance explained by each PC, and (b) displays the PCA scores, colored by pipe section indicator.

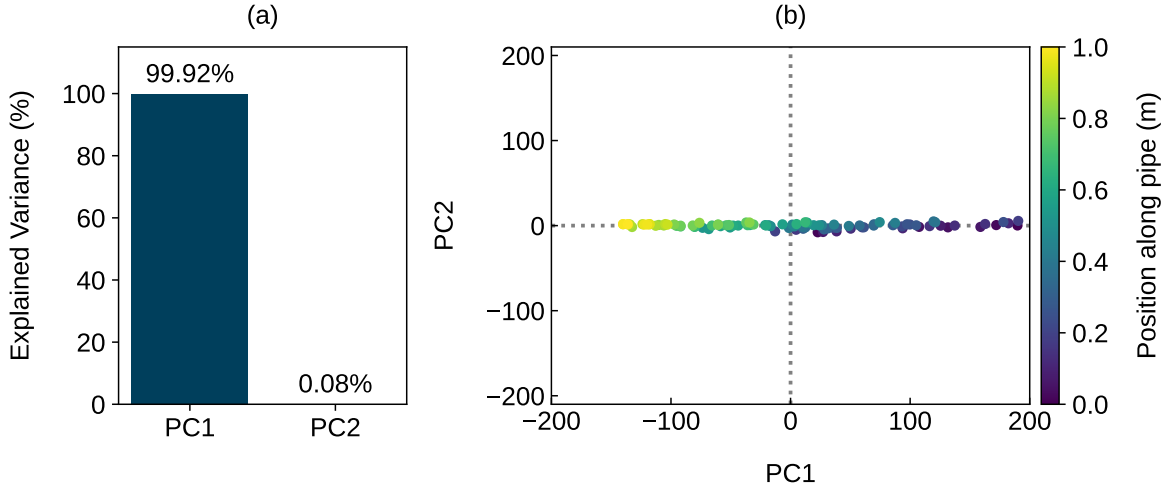

Source: The Author (2025)

Physically, this suggests the system is governed by changes in kinetic energy (related to v^2) rather than by independent pressure fluctuations. This is consistent with Bernoulli's principle,

where an increase in velocity corresponds to a pressure drop[14]. The alignment of PCA scores along Principal Component (PC)1 confirms that pressure adds little new information beyond what velocity already captures.

In summary, PCA transforms the original dataset into a new coordinate system where the axes are uncorrelated and ordered by how much they capture the variability of the data. This transformation simplifies the analysis and allows us to retrieve the dynamics of a system.

5.2.2 Mathematical Formulation and Implementation of PCA

We now take a more technical approach, as PCA relies on straightforward linear algebra concepts. Any experiment X involving m different measured quantities can be expressed as an m-dimensional column vector (SHLENS, 2014)

$$X = \begin{bmatrix} x_1 \\ x_2 \\ \vdots \\ x_m \end{bmatrix} \tag{5.62}$$

.

If we repeat the experiment n times, we obtain a matrix $\mathbf{X} \in \mathbb{R}^{m \times n}$, where the element x_{ij} is the value of the i-th measurement type in the j-th trial. From linear algebra, we know that each column vector of $\mathbf{X}$ lies in a vector space that is spanned by an orthonormal basis. Thus, each sample can be written as a linear combination of this set of unit-length, mutually orthogonal basis vectors. We represent our base as a $m \times m$ matrix

$$\mathbf{B} = \begin{bmatrix} 1 & 0 & \dots & 0 \\ 0 & 1 & \dots & 0 \\ \vdots & \vdots & \ddots & \vdots \\ 0 & 0 & \dots & 1 \end{bmatrix}_{m \times m} = \mathbf{I}. \tag{5.63}$$

However, this base is often based on convenience, and might not reflect the true structure or dynamics of the system. What PCA does is to find a better basis — new directions — that

[14] Bernoulli's principle for incompressible flow is given by

$$p = \rho \left(K - \frac{v^2}{2} \right),$$

where ρ is the fluid density and K is a constant.

align with the true dynamics of the system.

Let $\mathbf{P} \in \mathbb{R}^{m \times n}$ be a linear transformation matrix such that, when applied to the data matrix $\mathbf{X} \in \mathbb{R}^{m \times n}$, it produces the transformed data matrix $\mathbf{Y} \in \mathbb{R}^{m \times n}$. So,

$$\mathbf{Y} = \mathbf{PX}. \tag{5.64}$$

The rows of $\mathbf{P}$ are a set of new basis vectors for expressing the columns of $\mathbf{X}$ (SHLENS, 2014). We can verify this by making $\mathbf{p}_i$ to be the row vector of $\mathbf{P}$ and $\mathbf{x}_j$ the column vector of $\mathbf{X}$. So, Eq. 5.64 can be written as

$$\mathbf{Y} = \begin{bmatrix} \mathbf{p}_1 \\ \vdots \\ \mathbf{p}_i \\ \vdots \\ \mathbf{p}_m \end{bmatrix} \cdot \begin{bmatrix} \mathbf{x}_1 & \dots & \mathbf{x}_j & \dots & \mathbf{x}_n \end{bmatrix},$$

$$\mathbf{Y} = \begin{bmatrix} \mathbf{p}_1 \cdot \mathbf{x}_1 & \dots & \mathbf{p}_1 \cdot \mathbf{x}_j & \dots & \mathbf{p}_1 \cdot \mathbf{x}_n \\ \vdots & \ddots & \vdots & \ddots & \vdots \\ \mathbf{p}_i \cdot \mathbf{x}_1 & \cdots & \mathbf{p}_i \cdot \mathbf{x}_j & \cdots & \mathbf{p}_i \cdot \mathbf{x}_n \\ \vdots & \ddots & \vdots & \ddots & \vdots \\ \mathbf{p}_m \cdot \mathbf{x}_1 & \cdots & \mathbf{p}_m \cdot \mathbf{x}_j & \cdots & \mathbf{p}_m \cdot \mathbf{x}_n \end{bmatrix}. \tag{5.65}$$

We can see each element in the column vector $\mathbf{y}_j$ is composed of the dot product of $\mathbf{x}_i$ with a corresponding row in $\mathbf{P}$ ($\mathbf{y}_j = \mathbf{P}\mathbf{x}_j$). In other words, we are projecting the elements onto the rows of $\mathbf{P}$.Therefore, as already stated, the rows of $\mathbf{P}$, $\{\mathbf{p}_1, \dots, \mathbf{p}_m\}$ form the new basis vectors[15]. The key question that remains is: how do we construct $\mathbf{P}$?

In real-world data, noise is unavoidable and typically arises from imperfect measurements, external disturbances, or even as an unavoidable consequence of the fundamental laws of natrue, such as in quantum mechanics. When analyzing such systems, we often refer to the signal-to-noise ratio (SNR), which quantifies how good the signal is relative to the background. We define the SNR as the ratio of the variance of the signal to the variance of the noise[16]

$$SNR = \frac{\sigma^2_{\text{signal}}}{\sigma^2_{\text{noise}}}. \tag{5.66}$$

[15] We can also interpret $\mathbf{P}$ as a rotation and stretch operation that transforms $\mathbf{X}$ into $\mathbf{Y}$.

[16] This definition applies to random variables. However, in physics and chemistry, the SNR is typically defined as the ratio of signal power to noise power (INFANTE et al., 2021).

A high SNR indicates an efficient measurement, while a low SNR indicates a very noisy one. PCA assumes that the directions of highest variance in the data correspond to the directions containing the most meaningful structure, which is the signal. Noise, in contrast, is typically random, lower in variance, and tends to spread equally in all directions (Gaussian distribution) (SHLENS, 2014). In essence, PCA identifies a new basis that maximizes the SNR by aligning the new axes with the directions of greatest variance.

Another thing we need to have in mind is that we need to deal with redundancy in the data. Often, multiple variables end up capturing the same underlying information. For example, if two sensors are recording the same physical quantity, their outputs will be strongly correlated. In these situations, knowing one variable provides nearly the same information as knowing the other. This redundancy increases the dimensionality of the dataset and makes the structure harder to interpret. PCA helps reduce this dimensionality by identifying and removing these redundant directions, leaving only the axes that capture the essential variance in the data. But how do we mathematically measure variance and redundancy? This is where the covariance matrix comes in. The covariance matrix not only quantifies how much each variable varies individually (its variance), but also how much two variables change together (their covariance).

Let $\mathbf{a}$ and $\mathbf{b}$ be two zero-mean row vectors of size n, such that

$$\mathbf{a} = \begin{bmatrix} a_1 & a_2 & \dots & a_n \end{bmatrix}, \tag{5.67}$$

$$\mathbf{b} = \begin{bmatrix} b_1 & b_2 & \dots & b_n \end{bmatrix}. \tag{5.68}$$

Then, the covariance between them is given by (SHLENS, 2014)

$$\text{Cov}(\mathbf{a}, \mathbf{b}) = \sigma^2_{\mathbf{ab}} \equiv \frac{1}{n}\mathbf{a}\mathbf{b}^T, \tag{5.69}$$

where T represents the transpose of the vector[17][18]. We can generalize this for our data matrix $\mathbf{X}$ and generate the covariance matrix $\mathbf{C_X}$ (SHLENS, 2014).

[17] For vectors $\mathbf{x}$ and $\mathbf{y}$ with non-zero mean, the covariance is defined as

$$\text{Cov}(\mathbf{x}, \mathbf{y}) = \frac{1}{n}\sum_{i=1}^{n} (x_i - \langle x \rangle)(y_i - \langle y \rangle).$$

[18] If we are working with a sample rather than the full group, the factor $1/n$ is replaced by $1/(n-1)$, which corrects for bias in the estimation of the group covariance.

$$\mathbf{C_X} = \frac{1}{n}\mathbf{X}\mathbf{X}^T = \frac{1}{n}\begin{bmatrix} \sigma^2_{\mathbf{x}_1\mathbf{x}_1} & \sigma^2_{\mathbf{x}_1\mathbf{x}_2} & \cdots & \sigma^2_{\mathbf{x}_1\mathbf{x}_m} \\ \sigma^2_{\mathbf{x}_2\mathbf{x}_1} & \sigma^2_{\mathbf{x}_2\mathbf{x}_2} & \cdots & \vdots \\ \vdots & \vdots & \ddots & \vdots \\ \sigma^2_{\mathbf{x}_m\mathbf{x}_1} & \cdots & \cdots & \sigma^2_{\mathbf{x}_m\mathbf{x}_m} \end{bmatrix}, \tag{5.70}$$

where $\mathbf{C_X} \in \mathbb{R}^{m\times m}$. The main diagonal of $\mathbf{C_X}$ contains the variances of the measurement types, and the off-diagonal terms are the covariances between them. Similarly, we can define a covariance matrix for $\mathbf{Y}$, denoted $\mathbf{C_Y}$. Our goal is to find a transformation matrix $\mathbf{P}$ such that $\mathbf{C_Y}$ is diagonal, meaning all off-diagonal elements vanish, and the diagonal elements are ordered in descending variance.

Because $\mathbf{C_Y}$ is symmetric, the matrix $\mathbf{P}$ can be chosen to have orthonormal columns. Once $\mathbf{p}_1$ is found, all remaining basis vectors are orthogonal to it and to each other. The resulting ordered set of vectors $\{\mathbf{p}_1, \ldots, \mathbf{p}_m\}$ are the PC described in subsection 5.2.1.

We can summarize the aspects of PCA as follows:

1. **Linearity:** Let $\mathbf{p}_k \in \mathbb{R}^m$ be the weight vector for the k-th PC in the m-dimensional variable space. Each PC score $y_{k(i)}$ is a linear combination of the original variables row vector $\mathbf{x}_{(i)}$:

$$y_{k(i)} = \mathbf{p}_k \cdot \mathbf{x}_{(i)}, \quad \forall\ i = 1, 2, \ldots, n; \quad k = 1, 2, \ldots, m. \tag{5.71}$$

2. **Large-variance:** Principal components are ordered so that the first captures the greatest variance. The first weight vector $\mathbf{p}_1$ is obtained by solving

$$\mathbf{p}_1 = \arg\max_{\|\mathbf{p}\|=1} \left\{ \sum_{i=1}^{n} \left(\mathbf{x}_{(i)} \cdot \mathbf{p} \right)^2 \right\}. \tag{5.72}$$

   The constraint $\|\mathbf{p}\| = 1$ enforces unit length.

3. **Orthogonality:** Different principal components are uncorrelated and their weight vectors are orthonormal:

$$\mathbf{p}_i \cdot \mathbf{p}_j = \delta_{ij}. \tag{5.73}$$

We can solve PCA using eigenvector decomposition. Before proceeding, let us recall two useful matrix properties: (1) For two matrices $\mathbf{A}$ and $\mathbf{B}$, $(\mathbf{AB})^T = \mathbf{B}^T\mathbf{A}^T$; (2) The inverse of an orthogonal matrix equals its transpose, $\mathbf{A}^{-1} = \mathbf{A}^T$.

Starting from Eqs. 5.64 and 5.70, we have (SHLENS, 2014)

$$\mathbf{C_Y} = \frac{1}{n}\mathbf{Y}\mathbf{Y}^T,$$

$$\mathbf{C_Y} = \frac{1}{n}\left(\mathbf{P}\mathbf{X}\right)\left(\mathbf{P}\mathbf{X}\right)^T,$$

$$\mathbf{C_Y} = \frac{1}{n}\mathbf{P}\mathbf{X}\mathbf{X}^T\mathbf{P}^T,$$

$$\mathbf{C_Y} = \mathbf{P}\left(\frac{1}{n}\mathbf{X}\mathbf{X}^T\right)\mathbf{P}^T,$$

$$\mathbf{C_Y} = \mathbf{P}\mathbf{C_X}\mathbf{P}^T. \tag{5.74}$$

From linear algebra, any symmetric matrix $\mathbf{A}$ can be diagonalized by an orthogonal matrix of its eigenvectors. Therefore, there exists an orthogonal matrix $\mathbf{V}$ such that

$$\mathbf{A} = \mathbf{V}\mathbf{D}\mathbf{V}^T, \tag{5.75}$$

where $\mathbf{D}$ is a diagonal matrix whose entries are the eigenvalues $\lambda_1, \lambda_2, \ldots, \lambda_m$ of $\mathbf{A}$, and $\mathbf{V}$ is an orthogonal matrix whose columns are the orthonormal eigenvectors of $\mathbf{A}$. Each eigenvalue is sorted in decreasing order, $\lambda_1 \geq \lambda_2, \cdots \geq \lambda_m \geq 0$, and represents the variance captured along its corresponding eigenvector. The final step is to define each row $\mathbf{p}_i$ of $\mathbf{P}$ as an eigenvector of $\mathbf{C_X}$. That is, $\mathbf{V} = \mathbf{P}^T \rightarrow \mathbf{V}^T = \left(\mathbf{P}^T\right)^T = \mathbf{P}$. From Eq. 5.74

$$\mathbf{C_Y} = \mathbf{P}\left(\mathbf{P}^T\mathbf{D}\mathbf{P}\right)\mathbf{P}^T,$$

$$\mathbf{C_Y} = \left(\mathbf{P}\mathbf{P}^T\right)\mathbf{D}\left(\mathbf{P}\mathbf{P}^T\right),$$

$$\mathbf{C_Y} = \left(\mathbf{P}\mathbf{P}^{-1}\right)\mathbf{D}\left(\mathbf{P}\mathbf{P}^{-1}\right),$$

$$\mathbf{C_Y} = \mathbf{D}. \tag{5.76}$$

It is no surprise that choosing $\mathbf{P}$ as the matrix of eigenvectors of $\mathbf{C_X}$ diagonalizes $\mathbf{C_Y}$, since this is precisely the goal of PCA. From this, we conclude:

- The PCs of $\mathbf{X}$ (rows of $\mathbf{P}$) are the eigenvectors of the covariance matrix $\mathbf{C_X}$.
- The k-th diagonal element of the covariance matrix $\mathbf{C_Y}$ contains the variance of X along de eigenvector $\mathbf{p}_k$.

Thus, the basic steps of PCA are:

1. Subtract the mean of each measurement type from the dataset $\mathbf{X}$, centering the data.
2. Calculate the eigenvectors and eigenvalues of the covariance matrix $\mathbf{C_X}$, constructing the transformation matrix $\mathbf{P}$ from the eigenvectors.
3. Apply $\mathbf{P}$ to $\mathbf{X}$ to obtain the transformed data (scores) $\mathbf{Y}$.

PCA is quite easy to implement in Python using libraries such as scikit-learn (PEDREGOSA et al., 2011). A typical example code snippet is shown below:

Listing 1 – Typical structure of a PCA implementation in Python using the scikit-learn library.

```
import numpy as np
import pandas as pd
from sklearn.decomposition import PCA
import matplotlib.pyplot as plt

def perform_pca_from_csv(csv_path, n_components=None):
    """
    Perform PCA on data from a CSV file using scikit-learn.

    Parameters:
    - csv_path (str): Path to the CSV file (rows = n samples, columns = m
        variables).
    - n_components k (int or None): Number of principal components to keep.
    Returns:
    - singular_vectors (ndarray): Principal axes (m x k).
    - explained_variance (ndarray): Variance explained by each component.
    - scores (ndarray): PCA scores (n x m).
    """

    # Load CSV and keep numeric columns only (remove text columns)
    df = pd.read_csv(csv_path)
    X = df.select_dtypes(include=[np.number]).to_numpy()

    # PCA (mean-centers data)
    pca = PCA(n_components=n_components)
    scores = pca.fit_transform(X)

    # Return singular vectors, explained variances, and scores
    return pca.components_.T, pca.explained_variance_, scores


if __name__ == "__main__":
```

```
33      csv_file = "data.csv"  # Load the data

35      singular_vectors, variances, scores = perform_pca_from_csv(csv_file)

37      # Function to plot/print the results
        plot_results(singular_vectors, variances, scores)
```

Source: The Author (2025)

Despite PCA being a widely used and powerful tool for dimensionality reduction and data analysis, it has some limitations. First, PCA assumes that the relationships among variables are linear. Nonetheless, many complex systems often exhibit nonlinear dependencies that PCA cannot adequately capture (SHLENS, 2014). For example, in our pipe flow experiment, if we were to use velocity v instead of velocity squared v^2, PCA might fail to capture the important patterns. Second, PCA does not handle well with missing data. Incomplete measurements can distort the covariance matrix, leading to inaccurate eigenvectors. This problem is common in large datasets, such as those from meteorological or population studies, where data gaps are frequent. Third, maximizing the variance does not always lead to the formation of clusters or pattern identification (LEVER; KRZYWINSKI; ALTMAN, 2017). Finally, PCA is sensitive to the scale of the variables. Variables with larger variances tend to PCs, which can lead to misleading results. However, in turbulence analysis, this sensitivity can be advantageous since the directions of largest variance often correspond to the most physically significant fluctuations, which we want to identify.

Despite these limitations, PCA remains the cornerstone of multivariate statistical analysis due to its simplicity, computational efficiency, and ability to reveal the dominant patterns in complex datasets. For our purposes, PCA provides a foundational method to extract the signal $x(t)$ and compute its statistical properties.

6 FROM EXPERIMENTATION TO ANALYSIS

In this chapter, we describe in detail the experimental apparatus used in our study and apply the previously introduced statistical methods to the analysis of our data. The main focus is on the statistical properties of intensity distributions observed within the QML phase. However, for completeness and comparison, we also present results for the CW and SML regimes. This broader perspective highlights the unique features of the QML phase while situating it within the overall operational landscape of the laser. The discussion consolidates the experimental evidence and connects it directly to the theoretical framework outlined in the previous chapter.

6.1 EXPERIMENTAL APPARATUS

We now take a break from the theoretical discussion and proceed to the more technical part of this work: the description of the experimental setup. In Chapter 4, we presented the physics behind the Yb MLFL; here, we focus on its components and operation, as well as the methods used for data acquisition.

As stated in Section 4.1, our setup consists of a Yb MLFL assembled as a unidirectional ring cavity[1]. The specific system used was originally constructed by a former master's student[2]. All construction details, including encountered challenges and their respective solutions, are documented in his dissertation (MÉLO, 2017). The schematic of our setup is shown in Fig. 32, and the following description will make reference to the labeled components in that figure. The reader is advised to return to the image often throughout the experimental description to better visualize and understand the process.

We know that the laser can be understood as comprising three main elements (see section 3.1): the pumping source, the gain medium, and the optical feedback mechanism. In addition, two other components are of critical importance for the laser operation: the polarization control system and the intracavity dispersion management. Pumping is provided by a fiber-coupled diode laser (DL) (JDSU S30-7602-720), nominally centered at 976 nm with a linewidth ≈ 2.0 nm and a manufacturer-rated maximum output on the order of 720 to 740 mW. The diode is mounted on a Thorlabs LM1452 base and is both current- and temperature-stabilized using a Thorlabs LDC 240C current controller (A1) and a Thorlabs

[1] The first designs of such systems date back to the late 1990s (CAUTAERTS et al., 1997).
[2] The apparatus is based on the work made by Ilday, Chen and Kärtner (2005)

Figure 32 – Experimental apparatus of the Yb mode-locked fiber laser (MLFL). Intracavity elements: diode laser (DL) with current controller (A1) and temperature controller (A2), wavelength-division multiplexer (WDM), ytterbium-doped fiber (YDF) gain medium, a pair of GRIN collimators (COLL.), quarter-wave plate (QWP), half-wave plate (HWP), a pair of diffraction gratings (DG), reflective mirrors (M1), D-shaped mirror (M2), polarizing beam splitter (PBS), and optical isolator (OI). External components: beamsplitter (BS), photodetector (FD), spectrometer (A3), RF analyzer (A4), oscilloscope (A5), and computer (PC).

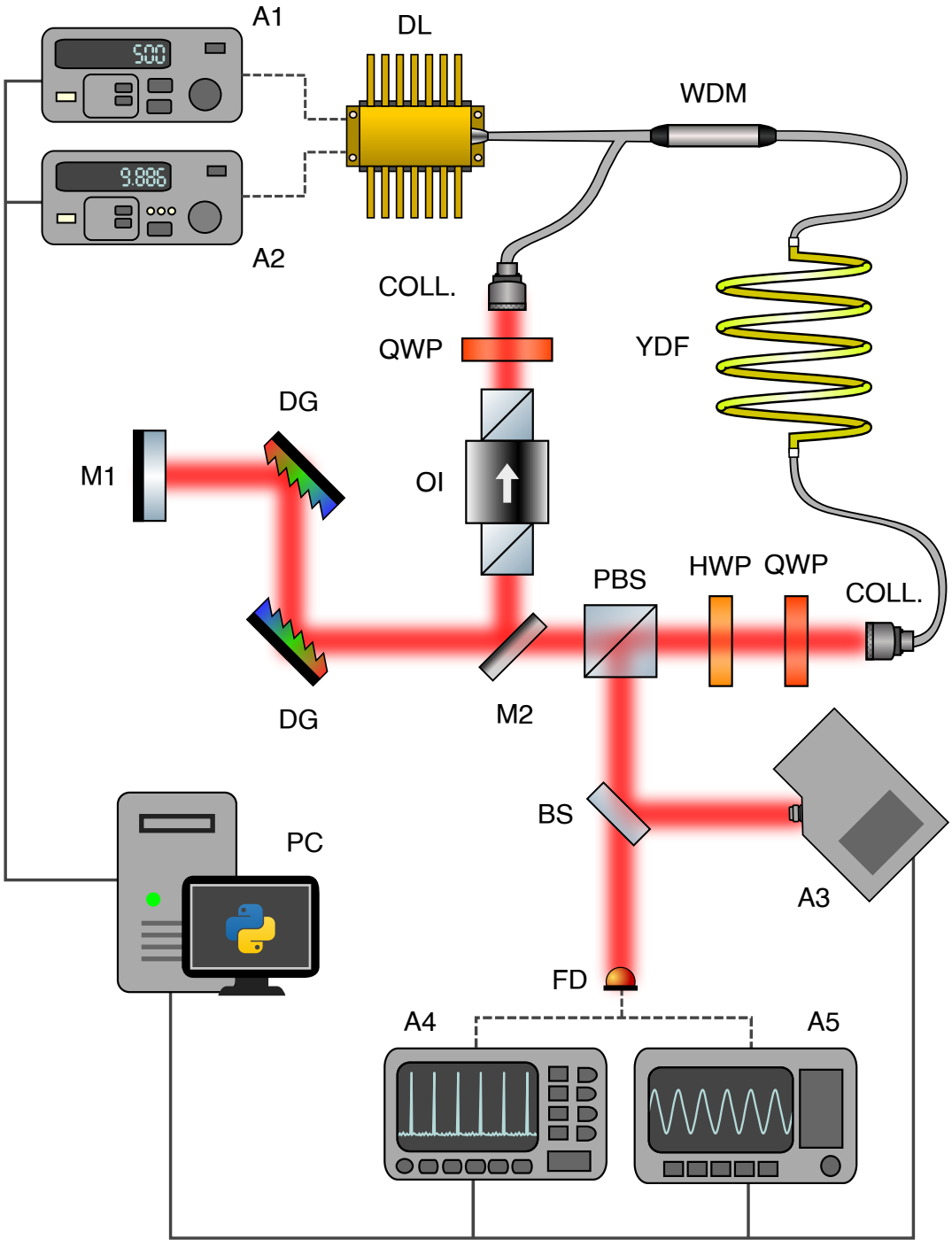

Source: The Author (2025)

TED 200C temperature controller (A2), respectively. During the system construction (MÉLO, 2017) and subsequent investigations of the RSB phenomenon (ALVES, 2023; ALVES et al., 2024), the pump source was characterized in detail. These analyses show a linear dependence of the output power on the diode drive current, which is expected, and can be expressed as

$$P_{\text{pump}} = \left(0.68\frac{\text{mW}}{\text{mA}}\right) I_{\text{pump}} - 9.2 \text{ mW}. \tag{6.1}$$

A fiber Bragg grating in the pumping fiber output provides wavelength-selective feedback, and the pump light is injected into the cavity through an Opinet Wavelength Division Multiplexing (WDM)[3] (FWDM-980T/1064R-250-4-1-NE). The WDM has three ports: Common, Pass, and Reflect. The Pass port, connected to the pump diode, transmits light in the 900–990 nm range with an isolation of about 25 to 26 dB[4]. The Common is a broadband port and connects to the Yb-Doped Fiber (YDF), while the Reflect port, used for re-injecting light into the cavity, operates in the 1025 to 1100 nm band, with an isolation reported between 13 and 17 dB[5]. The measured coupling efficiency from the pump diode through the WDM into the YDF is approximately 89% (CAMPOS, 2020).

The gain medium is a highly doped single-mode CorActive Yb214 fiber with nominal absorption of 1348 dB/m at 976 nm and a total length of $L \approx 22$ cm. Light is collimated into the free-space section by a Thorlabs GRIN 50-1064 collimator (COLL.). In our configuration, two equal collimators are employed: one to couple the light from the fiber into the free-space medium, and another to couple it back from free space into the fiber. The separation between these two collimators is set to approximately 35 cm, which it was determined a re-coupling efficiency of $\approx 35\%$, i.e., the cavity experiences a linear loss of about 65% per round trip. After the beam enters the free-space via the COLL., it passes through polarization elements used for achieving mode-locking by NPR (see subsection 4.1.2. The polarization elements are a quarter-wave plate (QWP) (Casix WPZ1225-1064-L/4) together with a half-wave plate (HWP)[6] (WPZ1225-1064-L/2) located before a polarizing beamsplitter (PBS) (Thorlabs PBS102). Another quarter-wave plate (same model) is placed on the input side of

[3]WDM is a technique that transmits multiple optical signals over a single fiber by using different wavelengths of light for each channel (ISHIO; MINOWA; NOSU, 1984).

[4]For a WDM, isolation refers to how well the component prevents light from on channel to leak to another channel

[5]The connection order of the WDM is reversed from what the manual dictates to prevent unabsorbed pump and cavity light from reaching and potentially damaging the diode laser, as noted by Mélo (2017).

[6]Although we adopt a different notation for the waveplates than the one used in Chapter 4, it is important to note that they refer to the same components.

the free-space section (before re-entering the gain fiber). As already mentioned in the mode-locked section, the QWPs change the polarization of the light between linear and circular (and vice versa), while the HWP rotates the direction of the linear polarization to the right angle for the PBS to work effectively. The PBS exerts the dual role of a polarizer (providing the nonlinear, intensity-dependent loss that emulates a SA) and as the output coupler. Linear transmission and reflection losses of the PBS are negligible when compared to other round-trip losses. We have that transmission loss is around 1%, while reflection is less than 0.5%. The extinction ratio of the transmitted beam is greater than $1000:1$, i.e., the PBS allows more than 1000 times as much light with a specific polarization to pass through compared to its perpendicular polarization counterpart.

In subsection 4.1.4, we discussed the necessity of balancing GVD and SPM, which is essential to achieving pulse compression, consequently, mode-locking operation. Dispersion inside the cavity is managed with a diffraction-grating (DG) pair (Thorlabs GR25-0610, 600 lines/mm) mounted on a translator to vary the separation between the gratings. This translator enables control of the net intracavity GVD. The DG produce an effective second-order dispersion β_2^{eff} (see Eq. 4.20) which depends on the grating geometry given by (MÉLO, 2017)

$$\beta_2^{\text{eff}} = -\frac{\lambda^3}{\pi c^2 \Lambda^2 \cos^2\theta}, \tag{6.2}$$

where

$$\theta = \arcsin\left[\frac{\lambda}{\Lambda} - \sin\theta_i\right]. \tag{6.3}$$

Here, Λ is the grating period (the inverse of the grooves per millimeter), and θ_i is the angle of incidence. Usually, achieving the required dispersion compensation demands two DG pairs arranged in what is known as a Treacy compressor setup (TREACY, 1969). However, in our experiment, the same effect is realized with a single DG pair combined with a high-reflectivity broadband flat mirror (M1) (Thorlabs BB1-E03-10, $R > 99\%$ in 750–1100 nm). For our configuration, we obtain a effective dispersion of $\beta_2^{\text{eff}} \approx -1400$ fs^2/mm[7]. The translator allows us to easily reach the zero-dispersion point, which corresponds to a grating separation of around 2.9 cm. Higher separations make the net dispersion more negative, which strongly affects the operating regime (CAMPOS, 2020).

[7]Side note: the DG pair account for 35% of the linear losses at each roundtrip (CAMPOS, 2020).

Note that M1 may be slightly tilted so that the reflected light is a bit offset and can be easily separated from the incident beam. If this is not the case, a D-shaped mirror (Thorlabs PFD10-03-P01, $R \approx 97\%$ at 1 μm) can be used to direct the light back into the fiber. The final main component of our intracavity is an optical isolator (OI) (Thorlabs IO-5-1030-VLP), which ensures unidirectional operation by preventing competition between counterpropagating signals in the gain medium. In the configuration shown in Fig. 32, the light travels in a clockwise direction. It is worth noting that the OI rotates the polarization of the signal by $45°$. This is one of the reasons we insert a QWP in the optical path. After passing through the OI and the QWP, the beam enters the COLL., is coupled into the Reflect port of the WDM, and completes a round trip in the cavity.

6.1.1 Procedures and data acquisition

Having detailed the internal elements that make the laser operational, we now concentrate on the components regarding the analysis of the system. Our attention is now on the beam coming out from the PBS. The first step is to split the light using a non-polarizing 90/10 beamsplitter (BS). This type of BS is used so that only a small fraction of the light is sent to the most sensitive equipment. The weaker beam is guided to an Ocean Optics HR4000 spectrometer (integration time set at 6 ms, with optical resolution of around 0.24 nm) to record the optical spectra. This is the most relevant instrument for the turbulent dynamics experiment. The remaining light is sent to homemade photodetectors (FDs) based on Fermionics FD150 photodiodes (1 GHz bandwidth). Part of the photodetector signal goes to a Keysight N9340B spectrum analyzer (A4), while the rest is directed to a Keysight/Agilent DSO7104B oscilloscope (A5) (1 GHz bandwidth). It is important to note that, since our focus is on the QML regime, the oscilloscope and spectrum analyzer serve only to confirm that the system is operating in the SML regime; their data are not used in the analysis. This is because, since there is no pulse formation in the QML phase (see Section 4.2), the oscilloscope and analyzer record no useful information (only noise) in this regime. For a systematic control of the experiment, the pumping current controller is driven by a Keysight 33500B function generator. All acquisition and control equipment are connected to a computer (PC), where a Python script ensures full automation of the experiment. Although the pump is driven via a current controller, the automation through the function generator is implemented by sending a DC voltage signal to the controller. A linear relation links the voltage send to the current controler

to the corresponding pump current, expressed by the equation

$$I_{\mathrm{mA}} = \left(0.8\frac{\mathrm{mA}}{\mathrm{mV}}\right) I_{\mathrm{mV}} + 1.3 \text{ mA} \tag{6.4}$$

Before analyzing the QML regime, we must first reach the SML regime. In our experiment, we aim to vary only the pumping current, without changing any other cavity parameters. To this end, the system is preferably operated in a self-starting mode-locking configuration. In such a setup, the laser automatically begins a pulsed operation after a certain pumping threshold, without the need for external interventions, such as tapping optical components or adjusting polarization (as is the case here). There is no definitive recipe for achieving self-starting mode-locking; success often depends on intimate familiarity with the experimental system. Nevertheless, certain techniques can help systematize the process, thereby increasing the likelihood of success. In this work, we adopt the procedure used in our laboratory and implemented in previous studies Mélo (2017), Campos (2020), Alves (2023).

Only a few combinations of waveplates orientations, together with the PBS, produce an intensity-dependent transmission, which is an underlying feature for NPR. A practical procedure to obtain a stable mode-locked state is as follows:

1. Set the laser to a low pumping current (e.g., ~ 100 mA).

2. Rotate the waveplates so that approximately half of the maximum possible output from the cavity is directed out through the PBS. Verify this by placing a power meter (Thorlabs PM100D) in an output branch from the PBS. This 50% level ensures a sufficiently strong measurement signal while keeping enough intracavity power for a stable operation.

3. (Optional) Perform a fine alignment. Carefully adjust the collimators (both vertically and horizontally) to ensure precise beam alignment between all optical components. This reduces losses and improving efficiency.

4. Increase the pumping power to a high level (≈ 700 mW) to strongly invert the gain medium. This enhances the nonlinear effects (Eq. 4.3) and enables potential pulses to overcome intracavity losses and grow to stable mode-locked operation.

5. Adjust the output waveplates (HWP and QWP) to minimize the detected power on the power meter. Annotate the HWP angle at this minimum, which defines the “zero” reference point. This step maximizes intracavity transmission.

6. From the zero reference point, slowly scan the HWP angle away from the minimum. Perform the scan gradually (small and slow angular steps) so that the laser response can be monitored on the oscilloscope. Due to symmetry, only a 180° range needs to be explored. Stop if a mode-locked operation is achieved.

7. If no stable pulse formation is detected, return the HWP to its zero position and slightly rotate the input QWP (located after the OI) by 1 or 2 degrees. This QWP controls the input light's ellipticity and can optimize the NPR effect.

8. Determine the new minimum output position for the output waveplates, which should be close to the previously minimum.

9. Repeat the HWP scanning process (step 6), searching for a stable pulse regime. Continue iterating steps 6–8 until mode-locking is achieved.

This procedure reliably finds a mode-locking operating point even if there are any twists or thermal dilatation in the fiber. Mechanical variations modify birefringence and nonlinear phase accumulation, but actively re-optimizing waveplate settings compensates for such effects. Any modification simply requires identifying a new combination of waveplate angles.

For the turbulence analysis, the experimental procedure is relatively simple: we need to collect 150,000 spectra at each current we want to analyze. However, some care must be taken. Our laser can exhibit a variety of complex dynamical behaviors, such as chaotic dynamics and solitonic pair formation, which have been previously studied in our group (MÉLO et al., 2018; CAMPOS et al., 2020; CAMPOS et al., 2020; CAMPOS; ACIOLI; MIRANDA, 2021). It is also known that our system presents hysteresis, meaning that increasing the pumping current lead to a different optical dynamical phases than the process of decreasing it.

At high pumping levels, exotic dynamical behavior can occur, but our interest lies in the regime preceding mode-locking, rather than preceding any arbitrary phase. Because we cannot control the exact pulsed phase in which the system will operate when performing at this high excitation levels, experiments done by increasing the pumping may depend on chance. Fortunately for us, once a pulsed regime is achieved, hysteresis allows us to decrease the pumping below the mode-locking threshold and still maintain pulsed operation. Furthermore, if we reduce the pumping sufficiently, the last pulsed regime to appear is always the SML regime (MÉLO et al., 2018; CAMPOS et al., 2020; ALVES et al., 2024). This behavior defines a threshold to lose mode-locking $P_{th(u)}$, giving us two relevant current values for our system:

a high pumping threshold $P_{\text{th(l)}}$, at which the system self-starts in a mode-locking regime, and a low pumping threshold $P_{th(u)}$, at which mode-locking is lost. Finally, it is worth noting that, once optimized and finely tuned, the system becomes sensitive to external fluctuations at the thresholds. Abrupt changes in the pumping or external vibrations can trigger or suppress mode-locking when operating near these threshold values.

Therefore, the experiment for turbulence analysis in the QML regime can be performed in two possible ways:

Backward mapping: We follow the standard procedure to achieve pulsed operation. Once the laser enters this regime, we decrease the current to obtain the threshold to lose mode-locking $P_{th(u)}$. Having this value, we increase the current again until pulsed operation resumes at $P_{\text{th(l)}}$. In this configuration, the laser should self-start into mode-locking simply by increasing the current. Then, lower the current again to reach the SML regime, which is just above the $P_{th(u)}$ point but below a level where other regimes might occur. This is typically set to 15–30% above $P_{th(u)}$. We begin data collection from this point, gradually lowering the current at a fixed current step rate. This method essentially maps the system in a backwards manner. This method is the easiest and more reliable.

Bottom-up with external stimulation: For this second approach, we begin as in the first method and find $P_{th(u)}$. Then, instead of increasing the pumping, we reduce the current further and start data collection from low to high pumping. When we are just above $P_{th(u)}$, we introduce an external stimulus, for example, a mechanical vibration or a short "pump scare" (a sudden jump to high current followed by a rapid drop). This can force the system into the SML regime. Although this method is not always effective, it yields the same type of QML–SML transition data as the first approach.

We performed both methods; however, we present here only the results of the first one. This choice is mainly because the first method involved a larger number of steps, resulting in a larger dataset for analysis. Future works could further explore the second method and investigate whether differences could arise from the methods chosen.

It is also important to note that, although the peak power increases when the laser enters the SML regime — since the total energy is compressed into shorter pulses — the average power decreases significantly. Therefore, when analyzing the QML regime, it is important to place absorptive neutral density filters (e.g., Thorlabs NE05A, NE30A, etc.) between the BS

and the spectrometer to avoid saturating the equipment. Data collection is briefly paused at key current values to change filters as necessary.

For systematic data collection performance (and also for convenience) the acquisition process is fully automated using a Python script, which heavily relies on libraries such as PyVISA (GRECCO et al., 2023) and SeaBreeze (AP, 2019). We directly access the instruments to retrieve data without relying on their proprietary software, which makes the process significantly faster. As mentioned earlier, a function generator is used to control the pump current. The implemented Python code for data acquisition is shown in Appendix A.

Basically, our procedure is as follows: we set a specific pumping current, collect 150,000 consecutive spectra, and store them as a DataFrame in an .npy file[8]. The spectrometer range is configured from 980 to 1065 nm, yielding 351 wavelength points. This results in an array of size $351 \times 150,000$, which is later transposed for PCA processing.

For each current value, collection takes approximately 16 minutes. In some cases, we collect multiple datasets at the same current as a precaution against potential saturation, which can occur even with filters due to the presence of abrupt spikes in the QML regime. Once a dataset is recorded, we slowly increase the current to the next measurement point (~ 30 mA higher) in small increments of 1 mA/s. This slow change avoids introducing abrupt perturbations to the system, which could influence its dynamics. Ultimately, we obtain about 35 measurements, which are later filtered down to 16 points: 6 in the CW regime, 3 in the SML regime, and the rest in the QML regime. From these, we present results for only 2 points in CW and SML each, and 4 in QML, to avoid redundancy since the system's behavior is qualitatively similar at each region. The selected points are: one in CW, one just before the CW–QML transition, one just after the CW–QML transition, two in the middle of the QML regime, one just before the QML–SML transition, one immediately after the QML–SML transition, and one deep in the SML regime.

6.2 RESULTS AND DISCUSSION

We now present our results. First, after performing the experiment, we identified the threshold to lose mode-locking at $P_{\text{th(u)}} = 477.3$ mA. For the data presented in the results, we specify the region in terms of $P/P_{\text{th(u)}}$ rather than the input current values. In this context, the

[8] An .npy file is a binary file format used to store NumPy arrays. These files are generated using the NumPy library (HARRIS et al., 2020) in Python and are significantly faster to access compared to text-based formats (e.g., .txt or .csv).

CW regime spans $0 \leq P/P_{\text{th(u)}} \leq 0.35$, the QML regime extends from $0.35 < P/P_{\text{th(u)}} \leq 1.0$, and the SML regime corresponds to $P/P_{\text{th(u)}} > 1.0$.

Figure 33 – Graph of the loadings versus wavelength for the first principal component (left panels) and representative spectra (right panels) in three regimes: (a,b) the CW regime ($P/P_{\text{th(u)}} = 0.30$); (c,d) the QML regime ($P/P_{\text{th(u)}} = 0.70$); and (e,f) the SML regime ($P/P_{\text{th(u)}} = 1.01$).

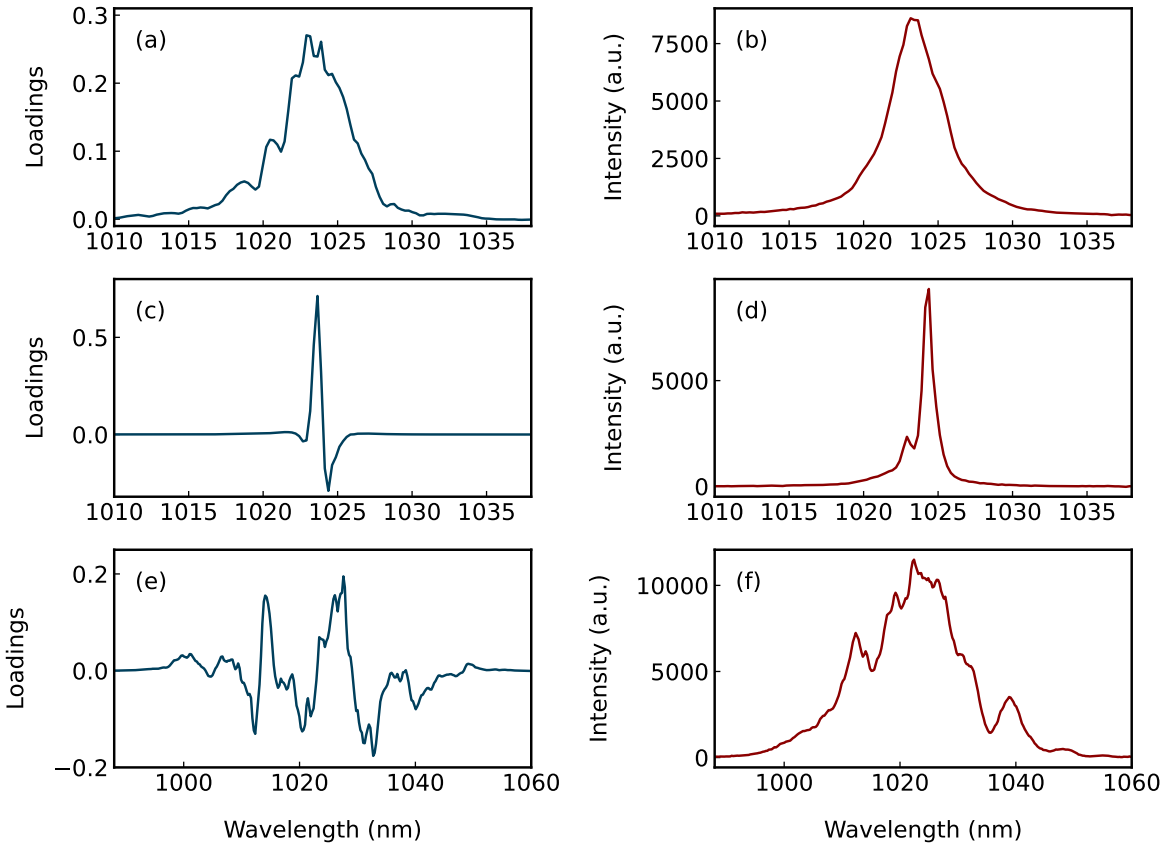

Source: The Author (2025)

For each pumping value, we obtain a data matrix $\mathbf{X} \in \mathbb{R}^{351\times150{,}000}$, where the 351 rows correspond to the wavelength points (variables) and the 150,000 columns of spectrum (realizations). The first step of our analysis is to apply PCA to these matrices.

Fig. 33 shows the loadings of PC1 (left panels) together with representative spectra (right panels) for the three regimes studied. In a PC1 loading plot, each peak or valley corresponds to a wavelength that responds to the dominant experimental variations. Peaks indicate wavelengths whose intensities increase when the main effect in the system — such as gain variation — becomes stronger, while valleys correspond to wavelengths whose intensities decrease under the same conditions. In Fig. 33a, PC1 resembles the average spectrum (Fig. 33b). This occurs because the largest differences between spectra arise from an overall increase or decrease in intensity across all wavelengths, rather than changes in the spectral profile. This indicates that

many wavelengths are strongly correlated, which makes them vary together across measurements. PC1 captures this collective variation. For Fig. 33b, PC1 exhibits one positive and one negative peak, indicating that the dominant variation is an intensity redistribution between two wavelength regions rather than a uniform change across the spectrum. An increase in one region is accompanied by a decrease in the other (Fig. 33d), consistent with the mode competition expected from our prior analysis. The horizontal asymmetry of the plot indicates that only one of the wavelength modes captures most of the dynamics. In contrast to Fig. 33b, Fig. 33c contains multiple peaks and valleys, meaning that the primary variation arises from simultaneous intensity changes across several distinct wavelength regions. In a laser spectrum, this often reflects gain redistribution among different longitudinal modes. PC1 does not only capture the changes in intensity, but now a more complex variation among the modes.

Remember that each PC is a weighted sum of the original variables, so the loadings directly identify which spectral regions contribute most to the captured variation. Thus, Fig. 33 effectively highlights the wavelengths most relevant to describing the largest trends in our spectra. PC1 provides an indication of the correlation structure in the data, but a more direct way to visualize these relationships is by plotting the correlation matrix. Fig. 34 shows the correlation matrix computed from the first 50,000 spectra[9].

Figure 34 – Correlation matrices for the first 50,000 spectra are shown for three regimes: (a) the CW regime ($P/P_{\text{th(u)}} = 0.30$); (b) the QML regime ($P/P_{\text{th(u)}} = 0.70$); and (c) the SML regime ($P/P_{\text{th(u)}} = 1.01$).

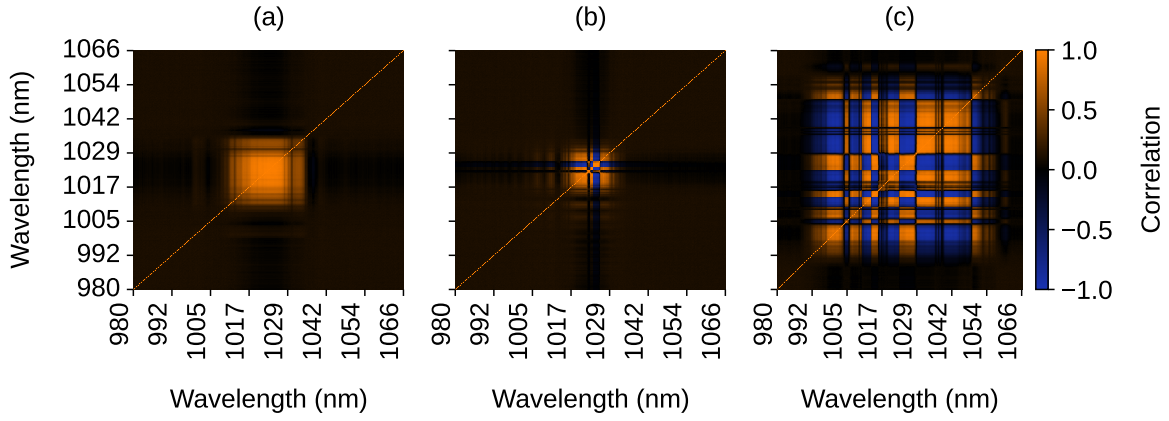

Source: The Author (2025)

In the SML regime (Fig. 34c), the correlation matrix reveals multiple regions of both correlation and anticorrelation, indicating that the wavelength variables are interconnected

[9] Only the first 50,000 spectra are used due to computational memory limitations. The full correlation matrix would contain on the order of 10^{10} points.

and share the intracavity energy. Unlike the SML regime, the QML phase (Fig. 33b) exhibits a thin strip of correlation and anticorrelation, suggesting that the whole energy is interchanged in two sets of modes. PC1 gives us indices of the overall dynamics. However, it is important to note that correlations among wavelengths do not necessarily imply complex fluctuation dynamics; the matrix primarily illustrates how the modes are linked to one another.

After performing PCA, it is important to assess how much information each principal component captures. This is done by examining the singular values of each PC and the cumulative explained variance across components.

Figure 35 – Plot of: (a) Singular values of PCA components. (b) Cumulative variance explained. The analysis is shown for $P/P_{\text{th(u)}} = 0.70$, corresponding to the QML region. For the SML and CW regions, the plots have the same overall aspect, so we show only the QML case (which is the region of interest) to illustrate the shape of the PCA.

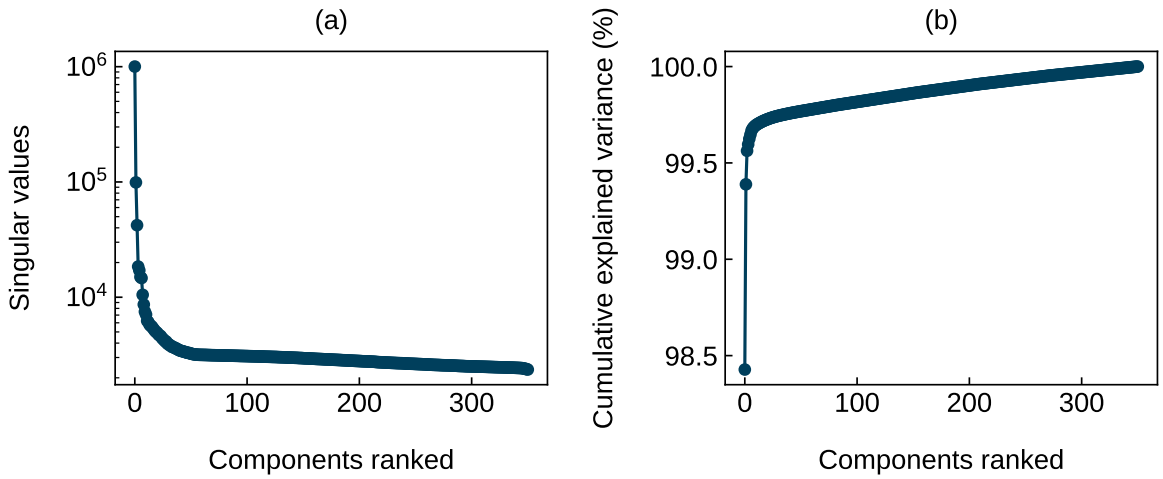

Source: The Author (2025)

Fig. 35 shows that the first PC alone accounts for more than 90% of the total variation in the data. Consequently, selecting the first three PCs is more than sufficient to describe the dynamics of the system in QML regime.

A plot of the variance explained by the first three PCs as a function of current (Fig. 36) confirms this: for nearly all data matrices $\mathbf{X}$ (each corresponding to an experiment at a single current), the first three components capture over 90% of the variance. The only exception occurs at the lowest CW point ($P/P_{\text{th(u)}} \approx 0.25$), where the SNR is very low, reducing the effectiveness of PCA. Even in this case, however, the first three PCs still account for more than 55% of the variance. Increasing the SNR slightly above this lowest CW point restores the explained variance above 90%, demonstrating the robustness and effectiveness of PCA.

Figure 36 – Plot of variance explained by the first three PCs as a function of current.

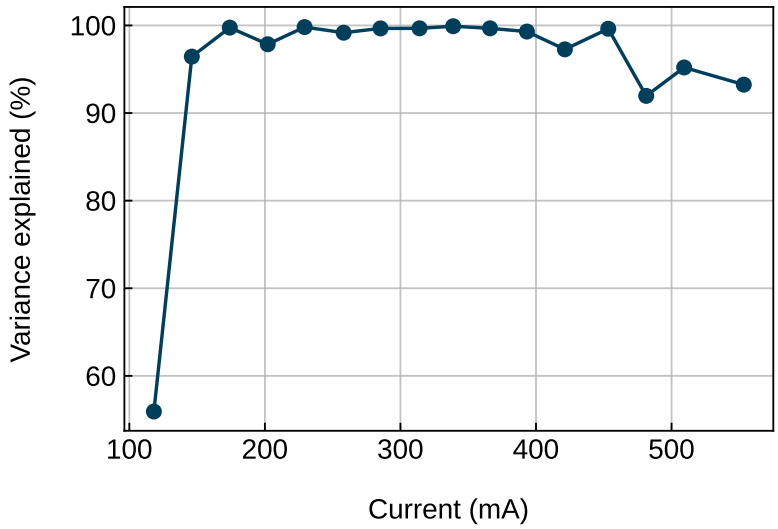

Source: The Author (2025)

Now, we can safely construct the signal used for the turbulence analysis: we project each data **X** onto the first three PCs and sum the resulting scores to form a one-dimensional series

$$u(t) = \sum_{k=1}^{3} \mathbf{p}_k \cdot \mathbf{X}. \tag{6.5}$$

Basically, we are taking the sum term by term of the first three rows of Eq. 5.65. With $u(t)$ in hand, we can now construct the normalized signal series as defined by Eqs.5.52 and 5.53. Fig.37 shows three examples of $\tilde{x}(t)$, one from each regime. Remember that the index t is discrete and enumerates consecutive spectra. A physical time axis can be assigned by using the average acquisition time per spectrum of ≈ 6.3 ms (6.0 ms of integration time in the spectrometer plus 0.3 ms for memory storing), although the absolute scale is not essential for the subsequent statistical analysis.

One motivation for the multivariate analysis was the odd behavior of the excess of kurtosis γ_2 seen when analyzing isolated wavelengths (Fig. 27). When we fixed a single peak along the QML region, the kurtosis initially rises above 3 and then falls back to 3 (or vice versa), indicating that the dominant dynamics were shifting to (or from) another part of the spectrum. By performing PCA and constructing $\tilde{x}(t)$ from Eq. 6.5 for all current values (Fig. 38), we remove this ambiguity: the alternation between Gaussian and non-Gaussian statistics vanishes (which is indicated by the kurtosis), and γ_2 exhibits a stable, positive elevation consistent with intermittent, heavy-tailed fluctuations. We also plot the variance for completeness, but

Figure 37 – temporal series, which is a result of the sum of the projected data of the first three PCs for three different regimes: (a) CW ($P/P_{\text{th(u)}} = 0.30$); (b) QML ($P/P_{\text{th(u)}} = 0.70$); and (c) SML ($P/P_{\text{th(u)}} = 1.01$).

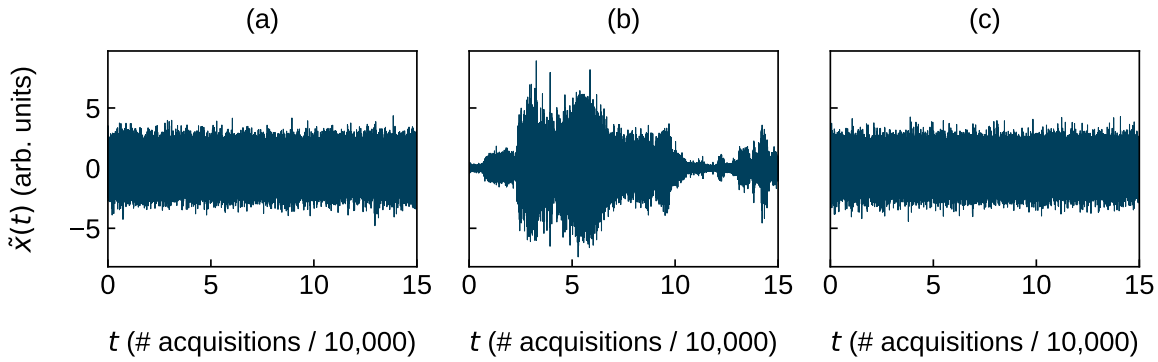

Source: The Author (2025)

Figure 38 – Variance (σ^2) and kurtosis excess ($\gamma_2 = \kappa - 3$) of $\tilde{x}(t)$ across different values of the pumping current, capturing all three regimes: the first two points correspond to the CW phase, while the last three correspond to the SML phase. Middle points are in the QML phase.

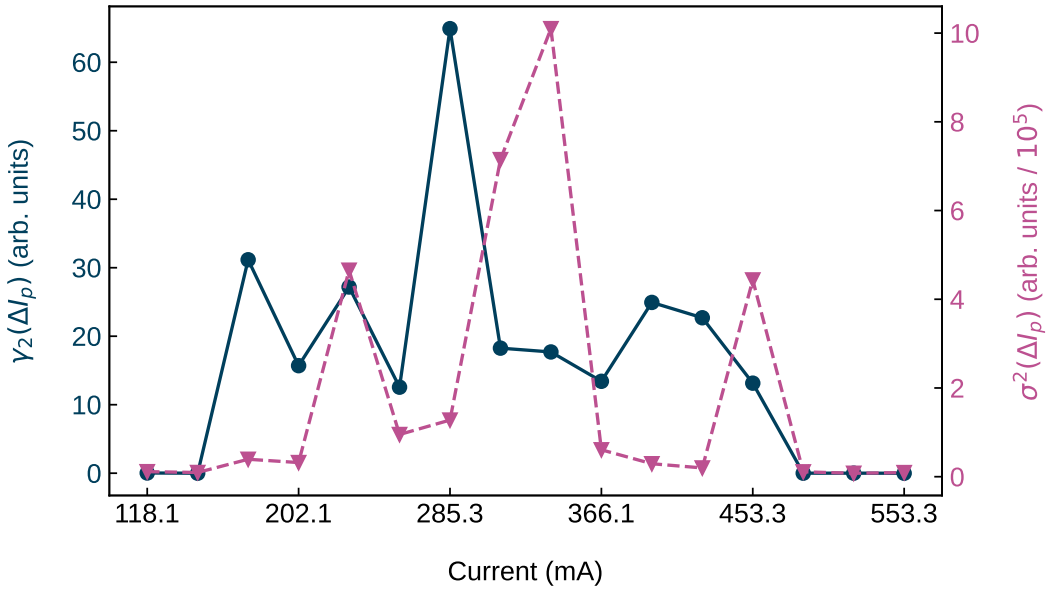

Source: The Author (2025)

recall that the analysis signal $\tilde{x}(t)$ is normalized ($\sigma^2 = 1$) by construction (Eq.5.53). Thus, the variance trend is not very significant on its own; it is primarily informative when accompanied by $\gamma_2 \approx 0$, which flags the CW and SML phases.

We now turn our attention to analyzing the probability distributions $P(x)$ of the increment series $\tilde{x}(t)$, which is the main step for characterizing the statistical nature of the fluctuations in our system. Our main goal is to investigate the presence of heavy-tailed distributions, which

indicate turbulent dynamics. We also want to solidify the Yb MLFL as an additional experimental platform where the H-theory can be applied. As already mentioned in subsection 5.1.2, our analysis suggested that, in the QML regime, we were able to fit the compound probability distribution (Eq. 5.20) for the number of scales corresponded to $N = 1$. Here, we present these results and a more thorough examination of the distributions across different dynamical regimes. To the best of our knowledge, this represents the first observation of a turbulent-like behavior in a laser system of this type.

6.2.1 Non-turbulent CW and SML regimes

We begin showing the results for parameters where turbulence is not expected: the CW and SML phases. The results shown in Fig. 39 indicate that the fluctuations are well described by a simple Gaussian distribution, consistent with linear, uncorrelated dynamics.

Figure 39 – Semi-log plot of the distribution $P(x)$ of the normalized experimental intensity increments $\tilde{x}(t)$ in the non-turbulent regime for (a) CW and (b) SML phases. The markers represent experimental data, while the solid line is the fitting. The curves in the same plot have an offset of 0.05 for distinguishability

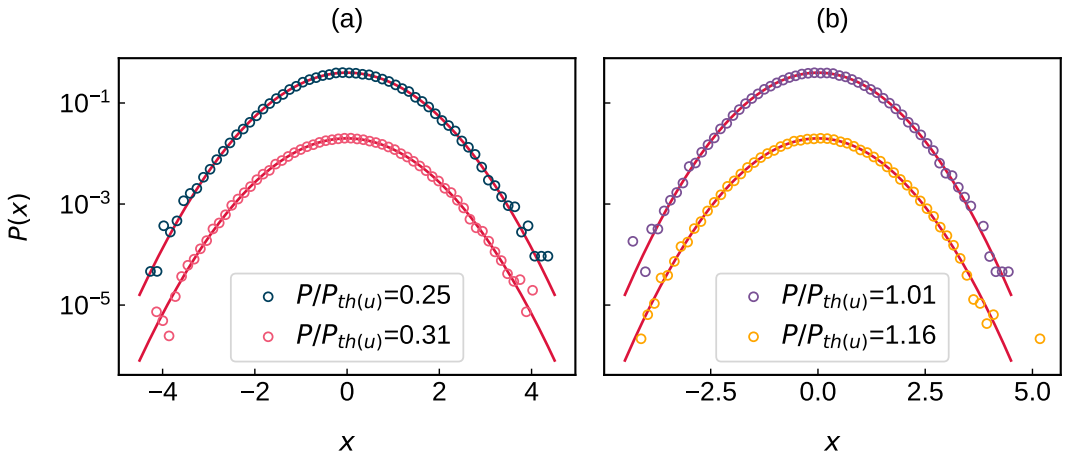

Source: The Author (2025)

Across all points in the CW and SML regime (near and far QML transition), the semi-log plots display the expected parabolic behavior characteristic of Gaussian statistics, with no deviations in the tails. This indicates that in these regions, the system does not exhibit the intermittent, large-amplitude excursions typical of turbulent dynamics. The increments remain symmetrically distributed around the mean, with a well-defined variance.

Within the framework of the H-theory, these results correspond to $N = 0$, which implies

Figure 40 – Background variance series $\epsilon(t)$ and their respective distributions $f(\epsilon)$ are shown for (a,b) CW at $P/P_{\text{th(u)}} = 0.31$ and (c,d) SML at $P/P_{\text{th(u)}} = 1.01$. The series $\epsilon(t)$ were constructed using the method described in subsection 5.1.2, with a window size of $M = 564$. The choice of window size affects only the skewness of plots (b) and (d); this value of M corresponds to zero skewness. Red circles in (b) and (d) represent experimental data, while the dashed vertical lines at $\epsilon = 1$ are the theoretical curves $\delta(\epsilon) = 1$.

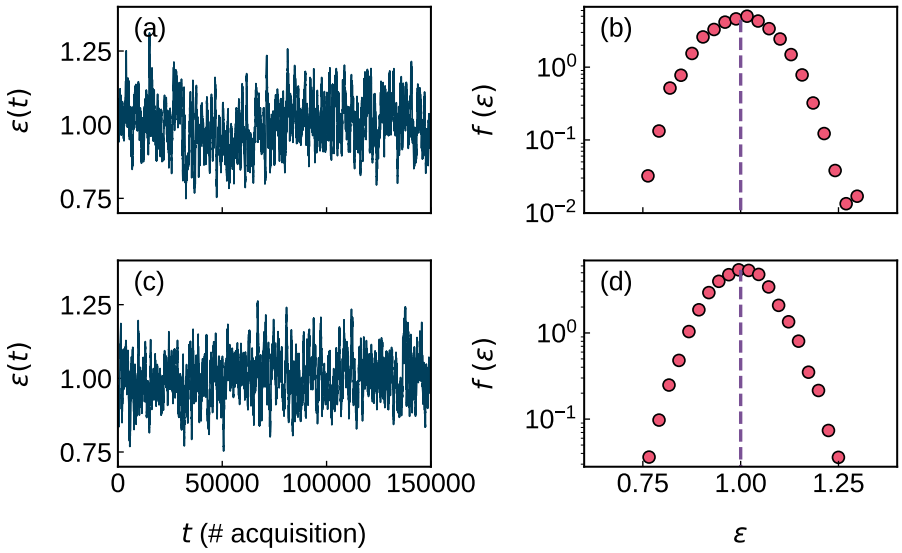

Source: The Author (2025)

the absence of hidden background fluctuations and a fixed Gaussian variance. In terms of Eq. 5.20, this is equivalent to setting $f(\epsilon) = \delta(\epsilon)$, leading to $P(x)$ being a simple Gaussian. Since we are working with a normalized series, the expected variance is ideally $\epsilon = 1$.

To verify this directly from the data, we construct a *background series* $\epsilon(t)$ by estimating the local variance of $x(t)$ within a sliding window of size M. This procedure, illustrated in Fig. 40, enables us to monitor how the instantaneous variance fluctuates around the normalized value. The window size M sets the time resolution of the estimation: small windows capture faster variations but introduce more statistical noise, whereas larger windows suppress noise but may conceal short-lived fluctuations. Although the normalization procedure enforces a global variance close to unity, in practice the value is not exactly one. The small deviations observed do not arise from experimental fluctuations but rather from numerical effects of the normalization and local variance estimation. To mitigate this, a window size of $M = 564$ was chosen, which minimizes skewness while preserving resolution. As shown in Figs. 40b and d, the resulting distribution of $\epsilon(t)$ remains sharply peaked around one, even if it does not form a perfect delta function (dotted line). This confirms that, in these regimes, the effective background fluctuations are constant, consistent with purely Gaussian dynamics.

6.2.2 Turbulent-like QML phase

Now we can ask: how does the background series look like for an arbitrary point in the QML region? Unlike the previous cases, we cannot simply choose an arbitrary window size. Instead, we must carefully follow the procedure outlined in Fig. 25. By doing so, we obtain the background series and its distribution, which are shown in Fig. 41.

Figure 41 – Plot of (a) the background variance series $\epsilon(t)$ and (b) a log-log plot of its corresponding distribution $f(\epsilon)$ for a point in the QML at $P/P_{\text{th(u)}} = 0.71$. Here, the window size is shown without the fitting curve; the usual procedure is first to find the fitting and then determine the appropriate window size.

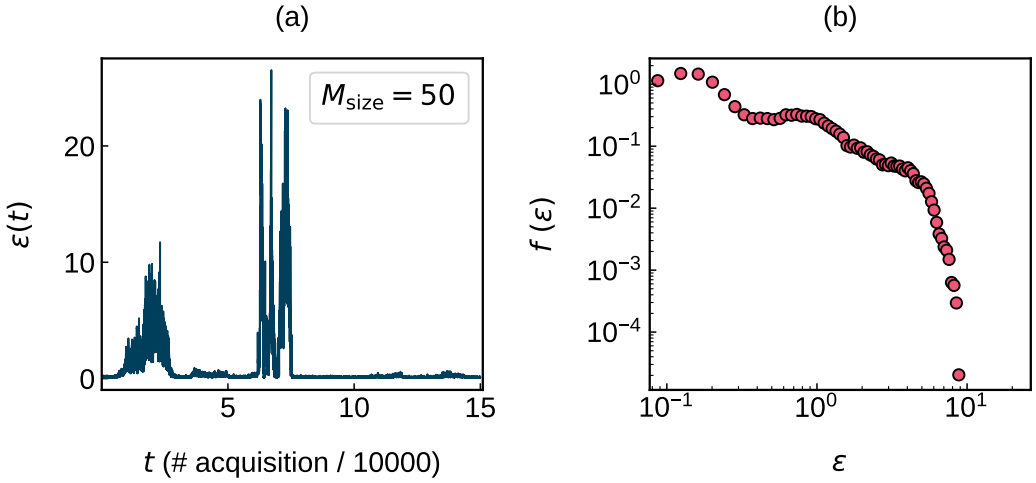

Source: The Author (2025)

From Fig. 41, it is evident that $f(\epsilon)$ exhibits a non-trivial structure, which suggests that $P(x)$ is expected to display heavy tails. Two main observations can be drawn from this background density. First, as discussed in previous sections, the inverse gamma distribution given by Eq.5.33 provides the best fit to the experimental background variance data. Second, the internal structure of $f(\epsilon)$ suggests the presence of clusters of statistically independent samples. This indicates that the background density can be effectively decomposed as a discrete statistical mixture of distributions, reflecting different local fluctuation regimes within the QML dynamics. The mixture is given by (GONZÁLEZ et al., 2017)

$$f(\epsilon) = \sum_{j=1}^{n} w_j f_j(\epsilon), \tag{6.6}$$

where w_j are the statistical weights, which satisfy $\sum_{j=1}^{n} w_j = 1$, and $f_j(\epsilon)$ is a curve obtained from Eq. 5.33. Since $f(\epsilon)$ is a mixture, the resulting probability distribution $P(x)$ is also a

statistical mixture, retaining the same structure as in Eq. 6.6, but now modeled using Eq. 5.41. Through visual inspection and with the aid of computational tools and machine learning techniques, such as scikit-learn (PEDREGOSA et al., 2011) and UMAP (MCINNES; HEALY; MELVILLE, 2018), we identify three distinct mixture components. Consequently, we can express Eq. 6.6 explicitly as

$$f(\epsilon) = w_1 f(\beta, \epsilon_0, \epsilon) + w_2 f(\beta', \epsilon_0', \epsilon) + (1 - w_1 - w_2) f(\beta'', \epsilon_0'', \epsilon), \tag{6.7}$$

$$P(x) = w_1 P(\beta, \epsilon_0, x) + w_2 P(\beta', \epsilon_0', x) + (1 - w_1 - w_2) P(\beta'', \epsilon_0'', x). \tag{6.8}$$

Fig. 42 shows the distributions $P(x)$ alongside $f(\epsilon)$ with their three fitted components. Each of these three components corresponds to one of the statistical mixtures identified in the analysis. Importantly, the fitting parameters for each component are the same for both $P(x)$ and $f(\epsilon)$, and are reported in Table 2.

Table 2 – Inverse-gamma fitting parameters for the mixture components of the probability densities $P(x)$ and $f(\epsilon)$ in a deep QML regime ($P/P_{\text{th(u)}} = 0.71$).

Curve	w (%)	β	ϵ_0
$P_1(x)\|f_1(\epsilon)$	42.7	1.0	0.29
$P_2(x)\|f_2(\epsilon)$	42.7	2.7	1.42
$P_3(x)\|f_3(\epsilon)$	14.6	8.14	0.80

Source: The Author (2025)

The most significant result in Fig. 42, besides the presence of a mixture structure, is the appearance of a heavy tail in $P(x)$, which indicates the existence of turbulent dynamics in the system. Upon closer inspection, it becomes clear that the components $P_2(x)$ and $P_3(x)$ contribute most to the tail enlargement. These components are characterized by a larger value of β, which corresponds to a broader variance distribution in the background series ϵ. The larger the value of β, the more "open" the curve becomes. The presence of these extreme events highlights the intermittent nature of the dynamics, where periods of relatively calm fluctuations are punctuated by bursts of higher intensity.

The parameters are fitted for each identified cluster using Eqs. 5.33 and 5.41 and are optimized via Root Mean Square Error (RMSE). The RMSE measures the differences between values predicted by a model and the values actually observed. It is calculated as

Figure 42 – Plot of (a) the semi-log distribution $P(x)$ and (b) the log-log distribution $f(\epsilon)$ for a point in the QML regime at $P/P_{\text{th(u)}} = 0.71$. The sum of the three fitted distributions is shown later.

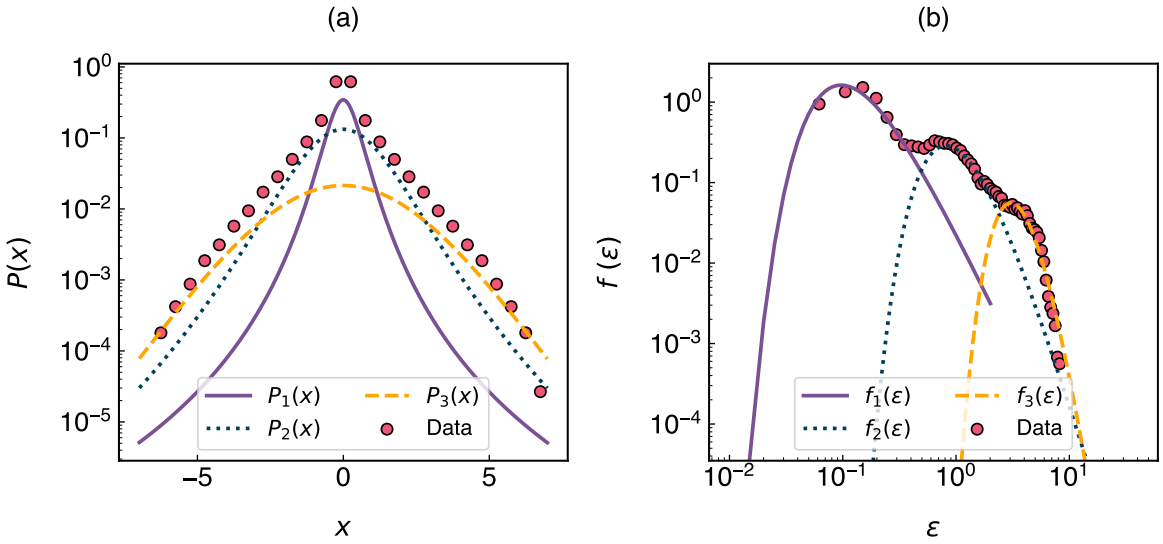

Source: The Author (2025)

$$\text{RMSE} = \sqrt{\frac{1}{n}\sum_{i=1}^{n}(x_i - p_i)^2}, \tag{6.9}$$

where n is the number of samples, x_i is the observed value for sample i, and p_i is the value predicted by the model for sample i. RMSE provides a single number summarizing the magnitude of prediction errors, with larger values indicating greater discrepancies. Because the errors are squared before averaging, RMSE penalizes larger errors more heavily, making it more sensitive to outliers. The optimal parameter values are found by minimizing Eq. 6.9.

All that remains is to verify whether this heavy-tail pattern also appears in other regions of the QML regime and whether the presence of a statistical mixture is a recurring feature. We focus the following discussion on three particular pumping powers: one near the transition from QML-CW, $P/P_{\text{th(u)}} = 0.42$, near the transition QML-SML, $P/P_{\text{th(u)}} = 0.95$, and $P/P_{\text{th(u)}} = 0.77$, well inside the QML region.

Fig. 43 shows $P(x)$ and $f(\epsilon)$ for these pumping powers, along with the previously studied one for completeness. Remarkably, we observe not only the presence of heavy tails in all selected cases, but also the same three-component statistical mixture identified in Fig. 42, demonstrating that this behavior is robust and not an isolated occurrence. For clarity, Fig. 43 presents only the resulting compound probability distributions, omitting the individual mixture components to avoid overcrowding the figure. This observation constitutes a major result of

the present work, providing direct evidence of turbulent dynamics within the QML phase—a phase recently associated with RSB—and, to our knowledge, demonstrating for the first time that it also exhibits turbulent behavior.

Regarding the possible origin of these mixtures, previous studies regarding similar turbulent mixtures have associated each component with an active mode (the dominant element that concentrates most of the energy) and quiet modes, corresponding to background modes that are normally weak but can be intermittently excited through nonlinear coupling (YAMAZAKI; LUECK; OSBORN, 1990; GONZÁLEZ et al., 2017). Although in this work we did not separate the data based on specific physical parameters, it is reasonable to infer that the mixtures may arise from stimulated and spontaneous turbulent emissions occurring under strong nonlinearity and mode competition. Based on fundamental considerations and the evidence presented here, we may propose that during QML a dominant mode governs the system's dynamics, but due to random phase coupling (e.g., polarization interactions of traveling waves inside the fiber), this mode can temporarily transfer a lot of energy to quiescent background modes. This energy exchange is then reflected in the statistical mixture. It is important to emphasize that to verify the validity of the proposed mechanism lies beyond the scope of the present work and will be addressed in future investigations.

Figure 43 – Distribution $P(x)$ of the laser intensity increment series $x(t)$ and the background variance distribution $f(\epsilon)$ within the QML phase for: (a,b) $P/P_{\text{th(u)}} = 0.42$; (c,d) $P/P_{\text{th(u)}} = 0.71$; (e,f) $P/P_{\text{th(u)}} = 0.77$; (g,h) $P/P_{\text{th(u)}} = 0.95$. The blue circles correspond to the experimental data, while the red lines represent the fits obtained using the dynamical hierarchical model for $N = \alpha = 1$. Both $f(\epsilon)$ and, consequently, $P(x)$ exhibit a mixture of three statistically independent components, as indicated by the presence of three prominent hills in $f(\epsilon)$.

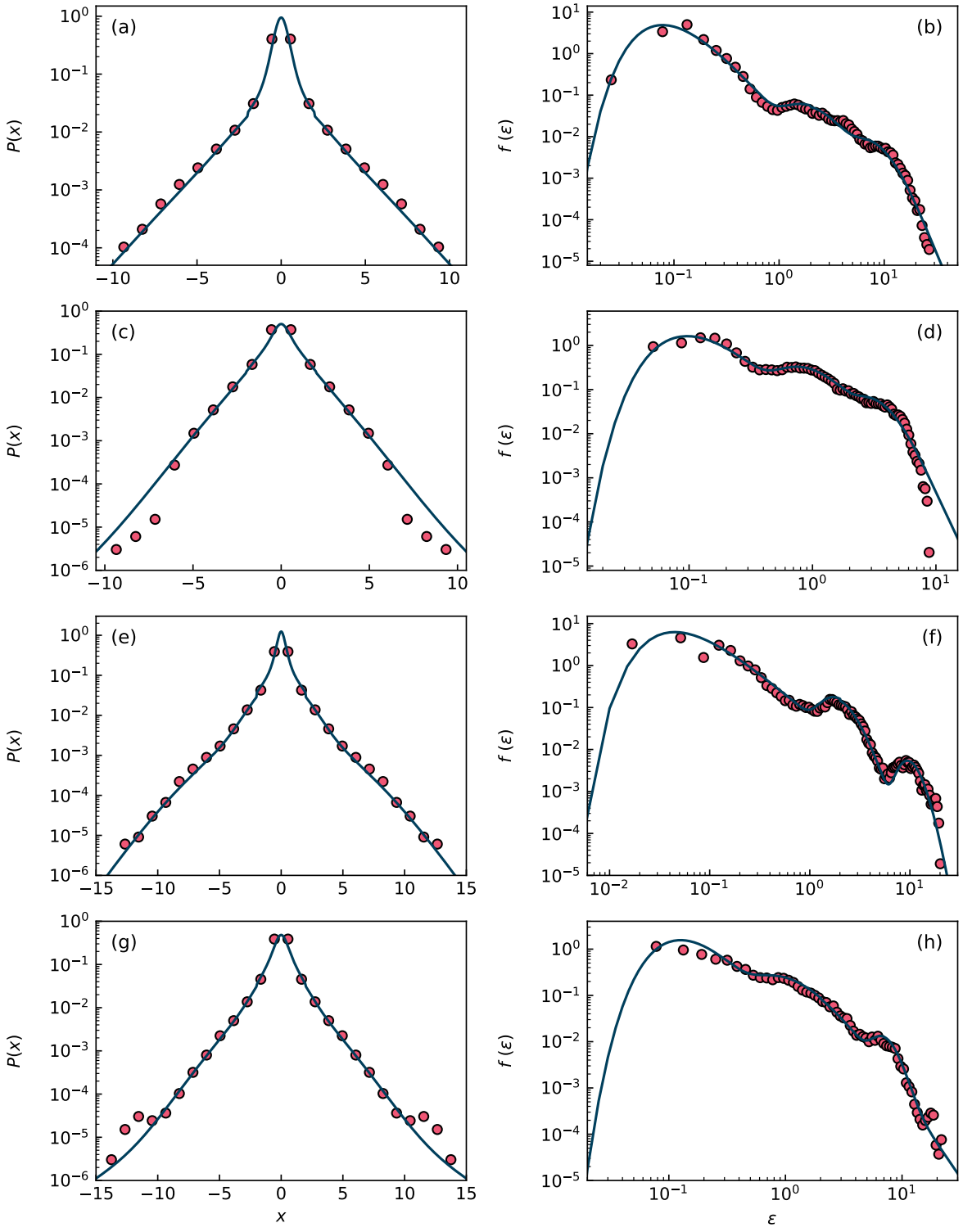

Source: The Author (2025)

7 CONCLUSION AND FUTURE PERSPECTIVES

In this dissertation, we investigated in detail the Quasi-Mode-Locking (QML) phase, focusing on its statistical properties. We first reviewed the theoretical basis of spin glasses and their mapping to random lasers, where Replica Symmetry Breaking (RSB) was initially predicted and experimentally observed (ANGELANI et al., 2006a; GHOFRANIHA et al., 2015). Building upon this analogy, we provided novel experimental evidence of a glassy phase preceding self-mode-locking in a mode-locked fiber laser (ALVES et al., 2024), which we termed QML, and which was first characterized by RSB in the intensity fluctuations. Furthermore, we extended the analysis to turbulence, employing statistical frameworks such as H-theory (GONZÁLEZ, 2017; MACÊDO et al., 2017), and demonstrated that heavy-tailed statistics and intermittency naturally emerge in our system. Finally, we introduced and applied Principal Component Analysis (PCA) as a statistical tool to uncover hidden structures in the laser dynamics, providing a complementary perspective to traditional correlation-based methods.

Future work should expand these results to other nonlinear regimes known in fiber lasers (MÉLO et al., 2018; CAMPOS et al., 2020), including soliton turbulence and rogue waves (ONORATO et al., 2013), where connections between RSB and turbulent behavior can be further explored. A particularly promising direction is to establish, for our system, the same turbulence–spin-glass correspondence already demonstrated in random lasers (GONZÁLEZ et al., 2018). Additionally, mapping the polarization dynamics may provide new insights into the mechanisms underlying mode-locking and its relation to glassy phases. Together, these perspectives aim to consolidate fiber lasers as versatile platforms for investigating the interplay between disorder, turbulence, and complexity in photonic systems.

REFERENCES

AGRAWAL, G. *Nonlinear Fiber Optics*. Elsevier Science, 2007. (Electronics & Electrical). ISBN 9780123695161. Available at: <https://books.google.com.br/books?id=b5S0JqHMoxAC>.

ALMEIDA, J. R. L. de; THOULESS, D. J. Stability of the sherrington-kirkpatrick solution of a spin glass model. *Journal of Physics A: Mathematical and General*, IOP Publishing, v. 11, n. 5, p. 983–990, may 1978. ISSN 1361-6447. Available at: <http://dx.doi.org/10.1088/0305-4470/11/5/028>.

ALVES, N. P.; ALVES, W. F.; SIQUEIRA, A. C.; MATIAS, N. L.; GOMES, A. S.; RAPOSO, E. P.; MIRANDA, M. H. G. de. Observation of replica symmetry breaking in standard mode-locked fiber laser. *Physical Review Letters*, American Physical Society (APS), v. 132, n. 9, Feb. 2024. ISSN 1079-7114. Available at: <http://dx.doi.org/10.1103/PhysRevLett.132.093801>.

ALVES, W. F. *Observação de quebra de simetria de réplica em laser de modos travados*. Universidade Federal de Pernambuco, 2023. Available at: <https://repositorio.ufpe.br/handle/123456789/52459>.

ANGELANI, L.; CONTI, C.; RUOCCO, G.; ZAMPONI, F. Glassy behavior of light. *Physical Review Letters*, American Physical Society (APS), v. 96, n. 6, feb 2006. ISSN 1079-7114. Available at: <http://dx.doi.org/10.1103/PhysRevLett.96.065702>.

ANGELANI, L.; CONTI, C.; RUOCCO, G.; ZAMPONI, F. Glassy behavior of light in random lasers. *Physical Review B*, American Physical Society (APS), v. 74, n. 10, Sep. 2006. ISSN 1550-235X. Available at: <http://dx.doi.org/10.1103/PhysRevB.74.104207>.

ANSELMET, F.; GAGNE, Y.; HOPFINGER, E. J.; ANTONIA, R. A. High-order velocity structure functions in turbulent shear flows. *Journal of Fluid Mechanics*, Cambridge University Press (CUP), v. 140, p. 63–89, Mar. 1984. ISSN 1469-7645. Available at: <http://dx.doi.org/10.1017/S0022112084000513>.

ANTENUCCI, F. *Statistical Physics of Wave Interactions*. Springer International Publishing, 2016. ISSN 2190-5061. ISBN 9783319412252. Available at: <http://dx.doi.org/10.1007/978-3-319-41225-2>.

ANTENUCCI, F.; BERGANZA, M. I.; LEUZZI, L. Statistical physical theory of mode-locking laser generation with a frequency comb. *Physical Review A*, American Physical Society (APS), v. 91, n. 4, Apr. 2015. ISSN 1094-1622. Available at: <http://dx.doi.org/10.1103/PhysRevA.91.043811>.

ANTENUCCI, F.; CONTI, C.; CRISANTI, A.; LEUZZI, L. General phase diagram of multimodal ordered and disordered lasers in closed and open cavities. *Physical Review Letters*, American Physical Society (APS), v. 114, n. 4, Jan. 2015. ISSN 1079-7114. Available at: <http://dx.doi.org/10.1103/PhysRevLett.114.043901>.

ANTENUCCI, F.; CRISANTI, A.; Ibáñez-Berganza, M.; MARRUZZO, A.; LEUZZI, L. Statistical mechanics models for multimode lasers and random lasers. *Philosophical Magazine*, Informa UK Limited, v. 96, n. 7–9, p. 704–731, Mar. 2016. ISSN 1478-6443. Available at: <http://dx.doi.org/10.1080/14786435.2016.1145359>.

ANTENUCCI, F.; CRISANTI, A.; LEUZZI, L. Complex spherical 2+4 spin glass: A model for nonlinear optics in random media. *Physical Review A*, American Physical Society (APS), v. 91, n. 5, May 2015. ISSN 1094-1622. Available at: <http://dx.doi.org/10.1103/PhysRevA.91.053816>.

ANTENUCCI, F.; CRISANTI, A.; LEUZZI, L. The glassy random laser: replica symmetry breaking in the intensity fluctuations of emission spectra. *Scientific Reports*, Springer Science and Business Media LLC, v. 5, n. 1, Nov. 2015. ISSN 2045-2322. Available at: <http://dx.doi.org/10.1038/srep16792>.

AP. *python-seabreeze: Python module for Ocean Optics spectrometers*. 2019. <https://github.com/ap--/python-seabreeze>. Accessed: 2025-02-18.

ARAÚJO, C.; GOMES, A.; RAPOSO, E. Lévy statistics and the glassy behavior of light in random fiber lasers. *Applied Sciences*, MDPI AG, v. 7, n. 7, p. 644, Jun. 2017. ISSN 2076-3417. Available at: <http://dx.doi.org/10.3390/app7070644>.

BALAKRISHNAN, N.; CHEN, W. W. S. *Handbook of Tables for Order Statistics from Lognormal Distributions with Applications*. Springer US, 1999. ISBN 9781461553090. Available at: <http://dx.doi.org/10.1007/978-1-4615-5309-0>.

BARAHONA, F. On the computational complexity of ising spin glass models. *Journal of Physics A: Mathematical and General*, IOP Publishing, v. 15, n. 10, p. 3241–3253, oct 1982. ISSN 1361-6447. Available at: <http://dx.doi.org/10.1088/0305-4470/15/10/028>.

BARRAT, A. *The p-spin spherical spin glass model*. arXiv, 1997. Available at: <https://arxiv.org/abs/cond-mat/9701031>.

BARTHELEMY, P.; BERTOLOTTI, J.; WIERSMA, D. S. A lévy flight for light. *Nature*, Springer Science and Business Media LLC, v. 453, n. 7194, p. 495–498, May 2008. ISSN 1476-4687. Available at: <http://dx.doi.org/10.1038/nature06948>.

BASAK, S.; BLANCO, A.; LÓPEZ, C. Large fluctuations at the lasing threshold of solid- and liquid-state dye lasers. *Scientific Reports*, Springer Science and Business Media LLC, v. 6, n. 1, aug 2016. ISSN 2045-2322. Available at: <http://dx.doi.org/10.1038/srep32134>.

BENZI, R.; CILIBERTO, S.; TRIPICCIONE, R.; BAUDET, C.; MASSAIOLI, F.; SUCCI, S. Extended self-similarity in turbulent flows. *Physical Review E*, American Physical Society (APS), v. 48, n. 1, p. R29–R32, Jul. 1993. ISSN 1095-3787. Available at: <http://dx.doi.org/10.1103/PhysRevE.48.R29>.

BENZI, R.; TOSCHI, F. Lectures on turbulence. *Physics Reports*, Elsevier BV, v. 1021, p. 1–106, Jun. 2023. ISSN 0370-1573. Available at: <http://dx.doi.org/10.1016/j.physrep.2023.05.001>.

BIRD, R.; STEWART, W.; LIGHTFOOT, E. *Transport Phenomena*. Wiley, 2006. (Transport Phenomena, v. 1). ISBN 9780470115398. Available at: <https://books.google.com.br/books?id=L5FnNIIaGfcC>.

BLANDIN, A. Theories versus experiments in the spin glass systems. *Le Journal de Physique Colloques*, EDP Sciences, v. 39, n. C6, p. C6–1499–C6–1516, aug 1978. ISSN 0449-1947. Available at: <http://dx.doi.org/10.1051/jphyscol:19786593>.

BLUNDELL, S. *Magnetism in Condensed Matter*. OUP Oxford, 2001. (Oxford Master Series in Condensed Matter Physics 4). ISBN 9780198505921. Available at: <https://books.google.com.br/books?id=Jk5yDwAAQBAJ>.

BOUNDS, D. G. New optimization methods from physics and biology. *Nature*, Springer Science and Business Media LLC, v. 329, n. 6136, p. 215–219, Sep. 1987. ISSN 1476-4687. Available at: <http://dx.doi.org/10.1038/329215a0>.

BRADLEY, J. V. The insidious l-shaped distribution. *Bulletin of the Psychonomic Society*, Springer Science and Business Media LLC, v. 20, n. 2, p. 85–88, Aug. 1982. ISSN 0090-5054. Available at: <http://dx.doi.org/10.3758/BF03330089>.

BRAY, A. J.; MOORE, M. A. Replica-symmetry breaking in spin-glass theories. *Physical Review Letters*, American Physical Society (APS), v. 41, n. 15, p. 1068–1072, oct 1978. ISSN 0031-9007. Available at: <http://dx.doi.org/10.1103/PhysRevLett.41.1068>.

CÂMARA, J. G.; SILVA, D. M. da; KASSAB, L. R. P.; SILVA-NETO, M. L.; PALACIOS, G.; ARAÚJO, C. B. de. Random lasing and replica symmetry breaking in GeO_2-PbO-MgO glass–ceramics doped with neodymium. *Scientific Reports*, Springer Science and Business Media LLC, v. 12, n. 1, Nov. 2022. ISSN 2045-2322. Available at: <http://dx.doi.org/10.1038/s41598-022-23893-4>.

CAMLEY, R. E.; LIVESEY, K. L. Consequences of the dzyaloshinskii-moriya interaction. *Surface Science Reports*, Elsevier BV, v. 78, n. 3, p. 100605, Aug. 2023. ISSN 0167-5729. Available at: <http://dx.doi.org/10.1016/j.surfrep.2023.100605>.

CAMPOS, C. L.; MÉLO, L. B.; CAVALCANTE, H. L. d. S.; ACIOLI, L. H.; MIRANDA, M. H. de. Internal nonlinear transmission in an yb mode-locked fiber laser through bifurcations. *Optics Communications*, Elsevier BV, v. 461, p. 125154, Apr. 2020. ISSN 0030-4018. Available at: <http://dx.doi.org/10.1016/j.optcom.2019.125154>.

CAMPOS, C. L. A. V.; ACIOLI, L. H.; MIRANDA, M. H. G. d. Hysteretic behavior for transmission curve and soliton temporal separation in multi-pulsing regime for mode-locked fiber lasers. *Laser Physics*, IOP Publishing, v. 31, n. 8, p. 085103, Jul. 2021. ISSN 1555-6611. Available at: <http://dx.doi.org/10.1088/1555-6611/ac1072>.

CAMPOS, C. L. A. V.; MÉLO, L. B. A.; ACIOLI, L. H.; MIRANDA, M. H. G. de. Discrete evolution of temporal separation and relative phase for bound solitons in a mode-locked yb fiber laser. *OSA Continuum*, Optica Publishing Group, v. 3, n. 6, p. 1490, May 2020. ISSN 2578-7519. Available at: <http://dx.doi.org/10.1364/OSAC.388673>.

CAMPOS, C. L. d. A. V. *Dinâmica Não linear em Laser de Modos travados com fibra dopada com YB*. Universidade Federal de Pernambuco, 2020. Available at: <https://repositorio.ufpe.br/handle/123456789/39013>.

CANNELLA, V.; MYDOSH, J. A. Magnetic ordering in gold-iron alloys. *Physical Review B*, American Physical Society (APS), v. 6, n. 11, p. 4220–4237, Dec. 1972. ISSN 0556-2805. Available at: <http://dx.doi.org/10.1103/PhysRevB.6.4220>.

CARVALHO, A. J. A.; GONÇALVES, I. M.; SANTOS E. P., G.; L., A. S.; ARAÚJO, P. M. S.; OLIVEIRA, H. P. de. "flexible electrospun fibrous membranes for efficient random laser emission: Incorporating rhodamine b (rhb) and carbon dot-enhanced rhodamine b (cd+rhb). 2024 AMBPS, Florianópolis, Santa Catarina, Brazil. 2024.

CASTELLANI, T.; CAVAGNA, A. Spin-glass theory for pedestrians. *Journal of Statistical Mechanics: Theory and Experiment*, IOP Publishing, v. 2005, n. 05, p. P05012, may 2005. ISSN 1742-5468. Available at: <http://dx.doi.org/10.1088/1742-5468/2005/05/P05012>.

CAUTAERTS, V.; RICHARDSON, D. J.; PASCHOTTA, R.; HANNA, D. C. Stretched pulse Yb^{3+}:silica fiber laser. *Optics Letters*, Optica Publishing Group, v. 22, n. 5, p. 316, Mar. 1997. ISSN 1539-4794. Available at: <http://dx.doi.org/10.1364/ol.22.000316>.

CHOSH, P. A characterization of a bimodal distribution. *Communications in Statistics - Theory and Methods*, Informa UK Limited, v. 7, n. 5, p. 475–477, Jan. 1978. ISSN 1532-415X. Available at: <http://dx.doi.org/10.1080/03610927808827640>.

CORONEL, E.; DAS, A.; GONZÁLEZ, I. R. R.; GOMES, A. S. L.; MARGULIS, W.; WEID, J. P. von der; RAPOSO, E. P. Evaluation of pearson correlation coefficient and parisi parameter of replica symmetry breaking in a hybrid electronically addressable random fiber laser. *Optics Express*, Optica Publishing Group, v. 29, n. 15, p. 24422, Jul. 2021. ISSN 1094-4087. Available at: <http://dx.doi.org/10.1364/OE.431981>.

CORONEL, E. D.; DAS, A.; SILVA-NETO, M. L. da; GONZÁLEZ, I. R. R.; GOMES, A. S. L.; RAPOSO, E. P. Statistical analysis of intensity fluctuations in the second harmonic of a multimode nd:yag laser through a modified pearson correlation coefficient. *Physical Review A*, American Physical Society (APS), v. 106, n. 6, Dec. 2022. ISSN 2469-9934. Available at: <http://dx.doi.org/10.1103/PhysRevA.106.063515>.

CORONEL, E. D.; SILVA-NETO, M. L. da; MOURA, A. L.; GONZÁLEZ, I. R. R.; PUGINA, R. S.; HILÁRIO, E. G.; ROCHA, E. G. da; CAIUT, J. M. A.; GOMES, A. S. L.; RAPOSO, E. P. Simultaneous evaluation of intermittency effects, replica symmetry breaking and modes dynamics correlations in a nd:yag random laser. *Scientific Reports*, Springer Science and Business Media LLC, v. 12, n. 1, jan 2022. ISSN 2045-2322. Available at: <http://dx.doi.org/10.1038/s41598-022-05090-5>.

CRISANTI, A.; SOMMERS, H. J. The sphericalp-spin interaction spin glass model: the statics. *Zeitschrift für Physik B Condensed Matter*, Springer Science and Business Media LLC, v. 87, n. 3, p. 341–354, oct 1992. ISSN 1434-6036. Available at: <http://dx.doi.org/10.1007/BF01309287>.

CUERVO-REYES, E. Why the dipolar response in dielectrics and spin-glasses is unavoidably universal. *Scientific Reports*, Springer Science and Business Media LLC, v. 6, n. 1, Jul. 2016. ISSN 2045-2322. Available at: <http://dx.doi.org/10.1038/srep29021>.

CUGLIANDOLO, L. F. *Advanced Statistical Physics: Quenched random systems*. 2022. Available at: <https://www.lpthe.jussieu.fr/~leticia/TEACHING/Master2022/disorder-2022.pdf>. Accessed on: 16 Jan. 2025.

DEKKER, C.; ARTS, A. F. M.; WIJN, H. W. de. $Rb_2Cu_{1-x}Co_xF_4$, a two-dimensional ising spin glass. *Journal of Applied Physics*, AIP Publishing, v. 63, n. 8, p. 4334–4336, apr 1988. ISSN 1089-7550. Available at: <http://dx.doi.org/10.1063/1.340193>.

DOTSENKO, V. S. Critical phenomena and quenched disorder. *Phys.–Usp.*, Uspekhi Fizicheskikh Nauk (UFN) Journal, v. 38, n. 5, p. 457–496, may 1995.

DUBOS, R. J. *Louis Pasteur, Free Lance of Science*. [S.l.]: Little, Brown and Company, 1950. 418 p. Quote from Pasteur: "Science knows no country, because knowledge belongs to humanity, and is the torch which illuminates the world. Science is the highest personification of the nation because that nation will remain the first which carries the furthest the works of thought and intelligence.".

EDWARDS, A. M.; PHILLIPS, R. A.; WATKINS, N. W.; FREEMAN, M. P.; MURPHY, E. J.; AFANASYEV, V.; BULDYREV, S. V.; LUZ, M. G. E. da; RAPOSO, E. P.; STANLEY, H. E.; VISWANATHAN, G. M. Revisiting lévy flight search patterns of wandering albatrosses, bumblebees and deer. *Nature*, Springer Science and Business Media LLC, v. 449, n. 7165, p. 1044–1048, Oct. 2007. ISSN 1476-4687. Available at: <http://dx.doi.org/10.1038/nature06199>.

EDWARDS, S. F.; ANDERSON, P. W. Theory of spin glasses. *Journal of Physics F: Metal Physics*, IOP Publishing, v. 5, n. 5, p. 965–974, May 1975. ISSN 0305-4608. Available at: <http://dx.doi.org/10.1088/0305-4608/5/5/017>.

EISBERG, R.; RESNICK, R. *Quantum Physics of Atoms, Molecules, Solids, Nuclei, and Particles*. [S.l.]: Wiley, 1985. (Quantum Physics of Atoms, Molecules, Solids, Nuclei, and Particles, vol. 1). ISBN 9780471873730.

ESTRADA, E. What is a complex system, after all? *Foundations of Science*, Springer Science and Business Media LLC, v. 29, n. 4, p. 1143–1170, May 2023. ISSN 1572-8471. Available at: <http://dx.doi.org/10.1007/s10699-023-09917-w>.

FERMANN, M. E.; HARTL, I. Ultrafast fibre lasers. *Nature Photonics*, Springer Science and Business Media LLC, v. 7, n. 11, p. 868–874, Oct. 2013. ISSN 1749-4893. Available at: <http://dx.doi.org/10.1038/nphoton.2013.280>.

FERMANN, M. E.; STOCK, M. L.; ANDREJCO, M. J.; SILBERBERG, Y. Passive mode locking by using nonlinear polarization evolution in a polarization-maintaining erbium-doped fiber. *Optics Letters*, Optica Publishing Group, v. 18, n. 11, p. 894, Jun. 1993. ISSN 1539-4794. Available at: <http://dx.doi.org/10.1364/ol.18.000894>.

FISCHER, K. H. Static properties of spin glasses. *Phys. Rev. Lett.*, American Physical Society (APS), v. 34, n. 23, p. 1438–1441, jun 1975.

FISHER, D. S.; HUSE, D. A. Ordered phase of short-range ising spin-glasses. *Physical Review Letters*, American Physical Society (APS), v. 56, n. 15, p. 1601–1604, apr 1986. ISSN 0031-9007. Available at: <http://dx.doi.org/10.1103/PhysRevLett.56.1601>.

FOX, A. G.; LI, T. Resonant modes in a maser interferometer. *Bell System Technical Journal*, Institute of Electrical and Electronics Engineers (IEEE), v. 40, n. 2, p. 453–488, mar 1961. ISSN 0005-8580. Available at: <http://dx.doi.org/10.1002/j.1538-7305.1961.tb01625.x>.

GALAZKA, R. R.; NAGATA, S.; KEESOM, P. H. Paramagnetic — spin-glass — antiferromagnetic phase transitions $Cd_{1-x}Mn_xTe$ from specific heat and magnetic susceptibility measurements. *Physical Review B*, American Physical Society (APS), v. 22, n. 7, p. 3344–3355, Oct. 1980. ISSN 0163-1829. Available at: <http://dx.doi.org/10.1103/PhysRevB.22.3344>.

GHOFRANIHA, N.; VIOLA, I.; MARIA, F. D.; BARBARELLA, G.; GIGLI, G.; LEUZZI, L.; CONTI, C. Experimental evidence of replica symmetry breaking in random lasers. *Nature*

Communications, Springer Science and Business Media LLC, v. 6, n. 1, jan 2015. ISSN 2041-1723. Available at: <http://dx.doi.org/10.1038/ncomms7058>.

GOLDSTEIN, S. Fluid mechanics in the first half of this century. *Annual Review of Fluid Mechanics*, Annual Reviews, v. 1, n. 1, p. 1–29, Jan. 1969. ISSN 1545-4479. Available at: <http://dx.doi.org/10.1146/annurev.fl.01.010169.000245>.

GOMES, A.; MOURA, A.; ARAÚJO, C. de; RAPOSO, E. *Lévy Statistics and Spin Glass Behavior in Random Lasers*. Jenny Stanford Publishing, 2023. ISBN 9781000778878. Available at: <https://books.google.com.br/books?id=1gmmEAAAQBAJ>.

GOMES, A. S.; MOURA, A. L.; ARAÚJO, C. B. de; RAPOSO, E. P. Recent advances and applications of random lasers and random fiber lasers. *Progress in Quantum Electronics*, Elsevier BV, v. 78, p. 100343, Aug. 2021. ISSN 0079-6727. Available at: <http://dx.doi.org/10.1016/j.pquantelec.2021.100343>.

GOMES, A. S. L.; ARAÚJO, C. B. de; MACÊDO, A. M. S.; GONZÁLEZ, I. R. R.; MENEZES, L. de S.; PINCHEIRA, P. I. R.; KASHYAP, R.; VASCONCELOS, G. L.; RAPOSO, E. P. Photonics bridges between turbulence and spin glass phenomena in the 2021 nobel prize in physics. *Light: Science & amp; Applications*, Springer Science and Business Media LLC, v. 11, n. 1, Apr. 2022. ISSN 2047-7538. Available at: <http://dx.doi.org/10.1038/s41377-022-00793-w>.

GOMES, A. S. L.; LIMA, B. C.; PINCHEIRA, P. I. R.; MOURA, A. L.; GAGNé, M.; RAPOSO, E. P.; de Araújo, C. B.; KASHYAP, R. Glassy behavior in a one-dimensional continuous-wave erbium-doped random fiber laser. *Physical Review A*, American Physical Society (APS), v. 94, n. 1, Jul. 2016. ISSN 2469-9934. Available at: <http://dx.doi.org/10.1103/PhysRevA.94.011801>.

GOMES, A. S. L.; RAPOSO, E. P.; MOURA, A. L.; FEWO, S. I.; PINCHEIRA, P. I. R.; JEREZ, V.; MAIA, L. J. Q.; ARAÚJO, C. B. de. Observation of lévy distribution and replica symmetry breaking in random lasers from a single set of measurements. *Scientific Reports*, Springer Science and Business Media LLC, v. 6, n. 1, Jun. 2016. ISSN 2045-2322. Available at: <http://dx.doi.org/10.1038/srep27987>.

GONZÁLEZ, I. R. R. *The h-theory: universality classes of hierarchical complex systems*. Phd Thesis (PhD Thesis) — Federal University of Pernambuco, Apr. 2017. Available at: <https://repositorio.ufpe.br/handle/123456789/25596>.

GONZÁLEZ, I. R. R.; LIMA, B. C.; PINCHEIRA, P. I. R.; BRUM, A. A.; MACÊDO, A. M. S.; VASCONCELOS, G. L.; MENEZES, L. de S.; RAPOSO, E. P.; GOMES, A. S. L.; KASHYAP, R. Turbulence hierarchy in a random fibre laser. *Nature Communications*, Springer Science and Business Media LLC, v. 8, n. 1, May 2017. ISSN 2041-1723. Available at: <http://dx.doi.org/10.1038/ncomms15731>.

GONZÁLEZ, I. R. R.; RAPOSO, E. P.; MACÊDO, A. M. S.; MENEZES, L. de S.; GOMES, A. S. L. Coexistence of turbulence-like and glassy behaviours in a photonic system. *Scientific Reports*, Springer Science and Business Media LLC, v. 8, n. 1, Nov. 2018. ISSN 2045-2322. Available at: <http://dx.doi.org/10.1038/s41598-018-35434-z>.

GORDON, A.; FISCHER, B. Phase transition theory of many-mode ordering and pulse formation in lasers. *Physical Review Letters*, American Physical Society (APS), v. 89, n. 10,

Aug. 2002. ISSN 1079-7114. Available at: <http://dx.doi.org/10.1103/PhysRevLett.89.103901>.

GORDON, A.; FISCHER, B. Phase transition theory of pulse formation in passively mode-locked lasers with dispersion and kerr nonlinearity. *Optics Communications*, Elsevier BV, v. 223, n. 1–3, p. 151–156, Jul. 2003. ISSN 0030-4018. Available at: <http://dx.doi.org/10.1016/s0030-4018(03)01622-5>.

GRECCO, H. E.; DARTIAILH, M. C.; THALHAMMER-THURNER, G.; BRONGER, T.; BAUER, F. Pyvisa: the python instrumentation package. *Journal of Open Source Software*, The Open Journal, v. 8, n. 84, p. 5304, Apr. 2023. ISSN 2475-9066. Available at: <http://dx.doi.org/10.21105/joss.05304>.

GROSS, D.; MEZARD, M. The simplest spin glass. *Nuclear Physics B*, Elsevier BV, v. 240, n. 4, p. 431–452, nov 1984. ISSN 0550-3213. Available at: <http://dx.doi.org/10.1016/0550-3213(84)90237-2>.

GUIMARÃES, A. *Magnetism and Magnetic Resonance in Solids*. Wiley, 1998. ISBN 9780471197744. Available at: <https://books.google.com.br/books?id=dCCIQgAACAAJ>.

HARGROVE, L. E.; FORK, R. L.; POLLACK, M. A. Locking of he–ne laser modes induced by synchronous intracavity modulation. *Applied Physics Letters*, AIP Publishing, v. 5, n. 1, p. 4–5, Jul. 1964. ISSN 1077-3118. Available at: <http://dx.doi.org/10.1063/1.1754025>.

HARRIS, C. R.; MILLMAN, K. J.; WALT, S. J. van der; GOMMERS, R.; VIRTANEN, P.; COURNAPEAU, D.; WIESER, E.; TAYLOR, J.; BERG, S.; SMITH, N. J.; KERN, R.; PICUS, M.; HOYER, S.; KERKWIJK, M. H. van; BRETT, M.; HALDANE, A.; del Río, J. F.; WIEBE, M.; PETERSON, P.; Gérard-Marchant, P.; SHEPPARD, K.; REDDY, T.; WECKESSER, W.; ABBASI, H.; GOHLKE, C.; OLIPHANT, T. E. Array programming with numpy. *Nature*, Springer Science and Business Media LLC, v. 585, n. 7825, p. 357–362, Sep. 2020. ISSN 1476-4687. Available at: <http://dx.doi.org/10.1038/s41586-020-2649-2>.

HAUS, H. Mode-locking of lasers. *IEEE Journal of Selected Topics in Quantum Electronics*, Institute of Electrical and Electronics Engineers (IEEE), v. 6, n. 6, p. 1173–1185, Nov. 2000. ISSN 1558-4542. Available at: <http://dx.doi.org/10.1109/2944.902165>.

HURD, C. M. Varieties of magnetic order in solids. *Contemp. Phys.*, Informa UK Limited, v. 23, n. 5, p. 469–493, Sep. 1982.

ILDAY, F. O.; CHEN, J.; KÄRTNER, F. X. Generation of sub-100-fs pulses at up to 200 mhz repetition rate from a passively mode-locked yb-doped fiber laser. *Optics Express*, Optica Publishing Group, v. 13, n. 7, p. 2716, 2005. ISSN 1094-4087. Available at: <http://dx.doi.org/10.1364/OPEX.13.002716>.

INFANTE, H. G.; WARREN, J.; CHALMERS, J.; DENT, G.; TODOLI, J. L.; COLLINGWOOD, J.; TELLING, N.; RESANO, M.; LIMBECK, A.; SCHOENBERGER, T.; HIBBERT, D. B.; LEGRESLEY, A.; ADAMS, K.; CRASTON, D. Glossary of methods and terms used in analytical spectroscopy (iupac recommendations 2019). *Pure and Applied Chemistry*, Walter de Gruyter GmbH, v. 93, n. 6, p. 647–776, Jun. 2021. ISSN 1365-3075. Available at: <http://dx.doi.org/10.1515/pac-2019-0203>.

IPPEN, E.; SHANK, C.; DIENES, A. Passive mode locking of the cw dye laser. *Applied Physics Letters*, AIP Publishing, v. 21, n. 8, p. 348–350, Oct. 1972. ISSN 1077-3118. Available at: <http://dx.doi.org/10.1063/1.1654406>.

ISHIO, H.; MINOWA, J.; NOSU, K. Review and status of wavelength-division-multiplexing technology and its application. *Journal of Lightwave Technology*, Institute of Electrical and Electronics Engineers (IEEE), v. 2, n. 4, p. 448–463, 1984. ISSN 0733-8724. Available at: <http://dx.doi.org/10.1109/jlt.1984.1073653>.

JENSEN, J.; MACKINTOSH, A. R. Spin waves in the ferromagnetic heavy rare earths. In: _____. *Rare Earth Magnetism*. Oxford University Press, Oxford, 1991. p. 181–275. ISBN 9781383023343. Available at: <http://dx.doi.org/10.1093/oso/9780198520276.003.0005>.

JIANG, X.; FENG, S.; SOUKOULIS, C. M.; ZI, J.; JOANNOPOULOS, J. D.; CAO, H. Coupling, competition, and stability of modes in random lasers. *Physical Review B*, American Physical Society (APS), v. 69, n. 10, Mar. 2004. ISSN 1550-235X. Available at: <http://dx.doi.org/10.1103/PhysRevB.69.104202>.

JOLLIFFE, I. T.; CADIMA, J. Principal component analysis: a review and recent developments. *Philosophical Transactions of the Royal Society A: Mathematical, Physical and Engineering Sciences*, The Royal Society, v. 374, n. 2065, p. 20150202, Apr. 2016. ISSN 1471-2962. Available at: <http://dx.doi.org/10.1098/rsta.2015.0202>.

KARDAR, M. *Statistical Physics of Particles*. Cambridge University Press, 2007. ISBN 9781139464871. Available at: <https://books.google.com.br/books?id=1WlFhiz5UjwC>.

KATZGRABER, H. G.; PALASSINI, M.; YOUNG, A. P. Monte carlo simulations of spin glasses at low temperatures. *Physical Review B*, American Physical Society (APS), v. 63, n. 18, apr 2001. ISSN 1095-3795. Available at: <http://dx.doi.org/10.1103/PhysRevB.63.184422>.

KELLER, U.; WEINGARTEN, K.; KARTNER, F.; KOPF, D.; BRAUN, B.; JUNG, I.; FLUCK, R.; HONNINGER, C.; MATUSCHEK, N.; AU, J. Aus der. Semiconductor saturable absorber mirrors (sesam's) for femtosecond to nanosecond pulse generation in solid-state lasers. *IEEE Journal of Selected Topics in Quantum Electronics*, Institute of Electrical and Electronics Engineers (IEEE), v. 2, n. 3, p. 435–453, 1996. ISSN 1077-260X. Available at: <http://dx.doi.org/10.1109/2944.571743>.

KLAFTER, J.; SHLESINGER, M. F.; ZUMOFEN, G. Beyond brownian motion. *Physics Today*, AIP Publishing, v. 49, n. 2, p. 33–39, Feb. 1996. ISSN 1945-0699. Available at: <http://dx.doi.org/10.1063/1.881487>.

KOLMOGOROV, A. The Local Structure of Turbulence in Incompressible Viscous Fluid for Very Large Reynolds' Numbers. *Akademiia Nauk SSSR Doklady*, v. 30, p. 301–305, Jan. 1941.

KOLMOGOROV, A. N. A refinement of previous hypotheses concerning the local structure of turbulence in a viscous incompressible fluid at high reynolds number. *Journal of Fluid Mechanics*, Cambridge University Press (CUP), v. 13, n. 1, p. 82–85, May 1962. ISSN 1469-7645. Available at: <http://dx.doi.org/10.1017/s0022112062000518>.

LAMB, W. E. Theory of an optical maser. *Physical Review*, American Physical Society (APS), v. 134, n. 6A, p. A1429–A1450, Jun. 1964. ISSN 0031-899X. Available at: <http://dx.doi.org/10.1103/physrev.134.a1429>.

LAWANDY, N. M.; BALACHANDRAN, R. M.; GOMES, A. S. L.; SAUVAIN, E. Laser action in strongly scattering media. *Nature*, Springer Science and Business Media LLC, v. 368, n. 6470, p. 436–438, Mar. 1994. ISSN 1476-4687. Available at: <http://dx.doi.org/10.1038/368436a0>.

LESIEUR, M. *Turbulence in Fluids*. Springer Netherlands, 2008. ISSN 0926-5112. ISBN 9781402064357. Available at: <http://dx.doi.org/10.1007/978-1-4020-6435-7>.

LETOKHOV, V. Generation of light by a scattering medium with negative resonance absorption. *Soviet Physics Jetp*, v. 26, n. 4, p. 1442–1452, October 1967.

LEUZZI, L.; CONTI, C.; FOLLI, V.; ANGELANI, L.; RUOCCO, G. Phase diagram and complexity of mode-locked lasers: From order to disorder. *Physical Review Letters*, American Physical Society (APS), v. 102, n. 8, Feb. 2009. ISSN 1079-7114. Available at: <http://dx.doi.org/10.1103/PhysRevLett.102.083901>.

LEVER, J.; KRZYWINSKI, M.; ALTMAN, N. Principal component analysis. *Nature Methods*, Springer Science and Business Media LLC, v. 14, n. 7, p. 641–642, Jul. 2017. ISSN 1548-7105. Available at: <http://dx.doi.org/10.1038/nmeth.4346>.

LI, J.; WU, H.; WANG, Z.; LIN, S.; LU, C.; RAPOSO, E. P.; GOMES, A. S. L.; RAO, Y. Lévy spectral intensity statistics in a raman random fiber laser. *Optics Letters*, Optica Publishing Group, v. 44, n. 11, p. 2799, May 2019. ISSN 1539-4794. Available at: <http://dx.doi.org/10.1364/OL.44.002799>.

LIMA, B. C.; GOMES, A. S. L.; PINCHEIRA, P. I. R.; MOURA, A. L.; GAGNÉ, M.; RAPOSO, E. P.; ARAÚJO, C. B. de; KASHYAP, R. Observation of lévy statistics in one-dimensional erbium-based random fiber laser. *Journal of the Optical Society of America B*, Optica Publishing Group, v. 34, n. 2, p. 293, Jan. 2017. ISSN 1520-8540. Available at: <http://dx.doi.org/10.1364/JOSAB.34.000293>.

L'VOV, V.; PROCACCIA, I. Hydrodynamic turbulence: a 19th century problem with a challenge for the 21st century. In: _____. *Flow at Ultra-High Reynolds and Rayleigh Numbers*. Springer New York, 1998. p. 375–390. ISBN 9781461222309. Available at: <http://dx.doi.org/10.1007/978-1-4612-2230-9_28>.

MA, Y.; CHENG, W.; HUANG, S.; SCHMITT, F. G.; LIN, X.; HUANG, Y. Hidden turbulence in van gogh's the starry night. *Physics of Fluids*, AIP Publishing, v. 36, n. 9, Sep. 2024. ISSN 1089-7666. Available at: <http://dx.doi.org/10.1063/5.0213627>.

MACÊDO, A. M. S.; GONZÁLEZ, I. R. R.; RAPOSO, E. P.; MENEZES, L. d. S.; GOMES, A. S. L. Turbulent intermittency in a random fiber laser. *Atoms*, MDPI AG, v. 7, n. 2, p. 43, Apr. 2019. ISSN 2218-2004. Available at: <http://dx.doi.org/10.3390/atoms7020043>.

MACÊDO, A. M. S.; GONZÁLEZ, I. R. R.; SALAZAR, D. S. P.; VASCONCELOS, G. L. Universality classes of fluctuation dynamics in hierarchical complex systems. *Physical Review E*, American Physical Society (APS), v. 95, n. 3, Mar. 2017. ISSN 2470-0053. Available at: <http://dx.doi.org/10.1103/PhysRevE.95.032315>.

MAIMAN, T. H. Stimulated optical radiation in ruby. *Nature*, Springer Science and Business Media LLC, v. 187, n. 4736, p. 493–494, Aug. 1960. ISSN 1476-4687. Available at: <http://dx.doi.org/10.1038/187493a0>.

MALETTA, H.; FELSCH, W. Insulating spin-glass system $Eu_xSr_{1-x}S$. *Physical Review B*, American Physical Society (APS), v. 20, n. 3, p. 1245–1260, Aug. 1979. ISSN 0163-1829. Available at: <http://dx.doi.org/10.1103/PhysRevB.20.1245>.

MALYAREVICH, A.; DENISOV, I.; YUMASHEV, K.; MIKHAILOV, V.; CONROY, R.; SINCLAIR, B. V:yag - a new passive q-switch for diode-pumped solid-state lasers. *Applied Physics B: Lasers and Optics*, Springer Science and Business Media LLC, v. 67, n. 5, p. 555–558, Nov. 1998. ISSN 1432-0649. Available at: <http://dx.doi.org/10.1007/s003400050544>.

MANDELBROT, B. B. Intermittent turbulence in self-similar cascades: divergence of high moments and dimension of the carrier. *Journal of Fluid Mechanics*, Cambridge University Press (CUP), v. 62, n. 2, p. 331–358, Jan. 1974. ISSN 1469-7645. Available at: <http://dx.doi.org/10.1017/S0022112074000711>.

MARKUSHEV, V. M.; ZOLIN, V. F.; BRISKINA, C. M. Luminescence and stimulated emission of neodymium in sodium lanthanum molybdate powders. *Soviet Journal of Quantum Electronics*, IOP Publishing, v. 16, n. 2, p. 281–283, feb 1986. ISSN 0049-1748. Available at: <http://dx.doi.org/10.1070/QE1986v016n02ABEH005792>.

MARSH, B. P.; KROEZE, R. M.; GANGULI, S.; GOPALAKRISHNAN, S.; KEELING, J.; LEV, B. L. Entanglement and replica symmetry breaking in a driven-dissipative quantum spin glass. *Physical Review X*, American Physical Society (APS), v. 14, n. 1, Feb. 2024. ISSN 2160-3308. Available at: <http://dx.doi.org/10.1103/PhysRevX.14.011026>.

MARTIN, D. L. Specific heat of spin-glass cumn below 3 k. *Physical Review B*, American Physical Society (APS), v. 20, n. 1, p. 368–375, Jul. 1979. ISSN 0163-1829. Available at: <http://dx.doi.org/10.1103/PhysRevB.20.368>.

MCINNES, L.; HEALY, J.; MELVILLE, J. *UMAP: Uniform Manifold Approximation and Projection for Dimension Reduction*. arXiv, 2018. Available at: <https://arxiv.org/abs/1802.03426>.

MÉLO, L. B. A.; PALACIOS, G. F. R.; CARELLI, P. V.; ACIOLI, L. H.; LEITE, J. R. R.; MIRANDA, M. H. G. de. Deterministic chaos in an ytterbium-doped mode-locked fiber laser. *Optics Express*, Optica Publishing Group, v. 26, n. 10, p. 13686, May 2018. ISSN 1094-4087. Available at: <http://dx.doi.org/10.1364/OE.26.013686>.

MÉLO, L. B. d. A. *Laser de modos travados em fibra de Itérbio construção e estudos sobre a dinâmica não linear*. Universidade Federal de Pernambuco, 2017. Available at: <https://repositorio.ufpe.br/handle/123456789/24631>.

MERRILL, J. W.; CAO, H.; DUFRESNE, E. R. Fluctuations and correlations of emission from random lasers. *Physical Review A*, American Physical Society (APS), v. 93, n. 2, Feb. 2016. ISSN 2469-9934. Available at: <http://dx.doi.org/10.1103/PhysRevA.93.021801>.

MÉZARD, M.; PARISI, G.; SOURLAS, N.; TOULOUSE, G.; VIRASORO, M. Nature of the spin-glass phase. *Physical Review Letters*, American Physical Society (APS), v. 52, n. 13, p. 1156–1159, Mar. 1984. ISSN 0031-9007. Available at: <http://dx.doi.org/10.1103/PhysRevLett.52.1156>.

MEZARD, M.; PARISI, G.; VIRASORO, M. *Spin Glass Theory and Beyond: An Introduction to the Replica Method and Its Applications*. WORLD SCIENTIFIC, 1986. ISSN 1793-1436. ISBN 9789812799371. Available at: <http://dx.doi.org/10.1142/0271>.

MOLEN, K. L. van der; MOSK, A. P.; LAGENDIJK, A. Intrinsic intensity fluctuations in random lasers. *Physical Review A*, American Physical Society (APS), v. 74, n. 5, Nov. 2006. ISSN 1094-1622. Available at: <http://dx.doi.org/10.1103/PhysRevA.74.053808>.

MORIYA, T. Anisotropic superexchange interaction and weak ferromagnetism. *Physical Review*, American Physical Society (APS), v. 120, n. 1, p. 91–98, Oct. 1960. ISSN 0031-899X. Available at: <http://dx.doi.org/10.1103/PhysRev.120.91>.

MOURA, A. L.; PINCHEIRA, P. I.; REYNA, A. S.; RAPOSO, E. P.; GOMES, A. S.; ARAÚJO, C. B. de. Replica symmetry breaking in the photonic ferromagneticlike spontaneous mode-locking phase of a multimode nd:yag laser. *Physical Review Letters*, American Physical Society (APS), v. 119, n. 16, Oct. 2017. ISSN 1079-7114. Available at: <http://dx.doi.org/10.1103/PhysRevLett.119.163902>.

MUJUMDAR, S.; TüRCK, V.; TORRE, R.; WIERSMA, D. S. Chaotic behavior of a random laser with static disorder. *Physical Review A*, American Physical Society (APS), v. 76, n. 3, sep 2007. ISSN 1094-1622. Available at: <http://dx.doi.org/10.1103/PhysRevA.76.033807>.

MYDOSH, J. *Spin Glasses: An Experimental Introduction*. Taylor & Francis, 1993. ISBN 9780748400386. Available at: <https://books.google.com.br/books?id=lRpmQgAACAAJ>.

NAGATA, S.; GALAZKA, R. R.; MULLIN, D. P.; AKBARZADEH, H.; KHATTAK, G. D.; FURDYNA, J. K.; KEESOM, P. H. Magnetic susceptibility, specific heat, and the spin-glass transition in $Hg_{1-x}Mn_xTe$. *Physical Review B*, American Physical Society (APS), v. 22, n. 7, p. 3331–3343, Oct. 1980. ISSN 0163-1829. Available at: <http://dx.doi.org/10.1103/PhysRevB.22.3331>.

NAVIER, C.; PROVINCIALE, B.; TOPOGRAFICO, R. O. *Resume des lecons donnees a l'Ecole des ponts et chaussees sur l'application de la mecanique a l'etablissement des constructions et des machines par Navier*. Societe Belge de librairie, 1839. Available at: <https://books.google.com.br/books?id=P5UooUk5c68C>.

NI, D.; SPäTH, M.; KLäMPFL, F.; HOHMANN, M. Properties and applications of random lasers as emerging light sources and optical sensors: A review. *Sensors*, MDPI AG, v. 23, n. 1, p. 247, Dec. 2022. ISSN 1424-8220. Available at: <http://dx.doi.org/10.3390/s23010247>.

NIDEESH, P.; LEKHA, C. C.; ANTOINE, R.; KALARIKKAL, N. Photonic replica symmetry breaking glassy transition and lévy flight statistics of emission intensity in dye-doped colloidal potassium sodium niobate random laser. *Optics & amp; Laser Technology*, Elsevier BV, v. 169, p. 110038, Feb. 2024. ISSN 0030-3992. Available at: <http://dx.doi.org/10.1016/j.optlastec.2023.110038>.

NISHIMORI, H. *Statistical Physics of Spin Glasses and Information Processing: An Introduction*. Oxford University Press, 2001. (International series of monographs on physics). ISBN 9780198509400. Available at: <https://books.google.com.br/books?id=nO0T1VzfhZcC>.

NOBELPRIZE.ORG. *Popular Information*. 2021. Available at: <https://www.nobelprize.org/prizes/physics/2021/popular-information/>. Accessed on: 15 Jan. 2025.

NOBELPRIZE.ORG. *Summary*. 2021. Available at: <https://www.nobelprize.org/prizes/physics/2021/summary/>. Accessed on: 15 Jan. 2025.

ONORATO, M.; RESIDORI, S.; BORTOLOZZO, U.; MONTINA, A.; ARECCHI, F. Rogue waves and their generating mechanisms in different physical contexts. *Physics Reports*, Elsevier BV, v. 528, n. 2, p. 47–89, Jul. 2013. ISSN 0370-1573. Available at: <http://dx.doi.org/10.1016/j.physrep.2013.03.001>.

PÁL, K. F. The ground state energy of the edwards-anderson ising spin glass with a hybrid genetic algorithm. *Physica A: Statistical Mechanics and its Applications*, Elsevier BV, v. 223, n. 3–4, p. 283–292, Jan. 1996. ISSN 0378-4371. Available at: <http://dx.doi.org/10.1016/0378-4371(95)00348-7>.

PALACIOS, G.; RAPOSO, E. P.; AMARAL, A. M.; ACIOLI, L. H.; FILHO, E. L. F. a.; ARAÚJO, C. B. de; SIQUEIRA, A. C. A. Replica symmetry breaking in higher-order optical soliton fission. Elsevier BV, 2025. Available at: <http://dx.doi.org/10.2139/ssrn.5215238>.

PALACIOS, G.; SIQUEIRA, A. C. A.; ARAÚJO, C. B. de; GOMES, A. S. L.; RAPOSO, E. P. Replica symmetry breaking in random lasers: A monte carlo study with mean-field interacting photonic random walkers. *Physical Review A*, American Physical Society (APS), v. 107, n. 6, Jun. 2023. ISSN 2469-9934. Available at: <http://dx.doi.org/10.1103/PhysRevA.107.063510>.

PARISI, G. Infinite number of order parameters for spin-glasses. *Physical Review Letters*, American Physical Society (APS), v. 43, n. 23, p. 1754–1756, Dec. 1979. ISSN 0031-9007. Available at: <http://dx.doi.org/10.1103/PhysRevLett.43.1754>.

PARISI, G. Toward a mean field theory for spin glasses. *Physics Letters A*, Elsevier BV, v. 73, n. 3, p. 203–205, Sep. 1979. ISSN 0375-9601. Available at: <http://dx.doi.org/10.1016/0375-9601(79)90708-4>.

PARISI, G. The order parameter for spin glasses: a function on the interval 0-1. *Journal of Physics A: Mathematical and General*, IOP Publishing, v. 13, n. 3, p. 1101–1112, Mar. 1980. ISSN 1361-6447. Available at: <http://dx.doi.org/10.1088/0305-4470/13/3/042>.

PARISI, G.; FRISCH, U. *G. Parisi and U. Frisch in Turbulence and Predictability in Geophysical Fluid Dynamics, ed. M. Ghil, R. Benzi and G. Parisi*. [S.l.]: North-Holland, Amsterdam, 1985.

PASCHOTTA, R. *Active Mode Locking*. RP Photonics AG, 2006. RP Photonics Encyclopedia. Available at: <https://www.rp-photonics.com/active_mode_locking.html>.

PASCHOTTA, R.; NILSSON, J.; TROPPER, A.; HANNA, D. Ytterbium-doped fiber amplifiers. *IEEE Journal of Quantum Electronics*, Institute of Electrical and Electronics Engineers (IEEE), v. 33, n. 7, p. 1049–1056, Jul. 1997. ISSN 0018-9197. Available at: <http://dx.doi.org/10.1109/3.594865>.

PASK, H.; CARMAN, R.; HANNA, D.; TROPPER, A.; MACKECHNIE, C.; BARBER, P.; DAWES, J. Ytterbium-doped silica fiber lasers: versatile sources for the 1-1.2 μm region. *IEEE Journal of Selected Topics in Quantum Electronics*, Institute of Electrical and Electronics Engineers (IEEE), v. 1, n. 1, p. 2–13, Apr. 1995. ISSN 1077-260X. Available at: <http://dx.doi.org/10.1109/2944.468377>.

PEDREGOSA, F.; VAROQUAUX, G.; GRAMFORT, A.; MICHEL, V.; THIRION, B.; GRISEL, O.; BLONDEL, M.; PRETTENHOFER, P.; WEISS, R.; DUBOURG, V.; VANDERPLAS, J.; PASSOS, A.; COURNAPEAU, D.; BRUCHER, M.; PERROT, M.; DUCHESNAY, E. Scikit-learn: Machine learning in Python. *Journal of Machine Learning Research*, v. 12, p. 2825–2830, 2011.

PHYSICS, T. N. C. for. *Scientific Background on the Nobel Prize in Physics 2021*: "for groundbreaking contributions to our understanding of complex physical systems". 2021. Available at: <https://www.nobelprize.org/uploads/2021/10/sciback_fy_en_21.pdf>. Accessed on: 15 Jan. 2025.

PIERANGELI, D.; TAVANI, A.; MEI, F. D.; AGRANAT, A. J.; CONTI, C.; DELRE, E. Observation of replica symmetry breaking in disordered nonlinear wave propagation. *Nature Communications*, Springer Science and Business Media LLC, v. 8, n. 1, Nov. 2017. ISSN 2041-1723. Available at: <http://dx.doi.org/10.1038/s41467-017-01612-2>.

PINCHEIRA, P. I. R.; SILVA, A. F.; FEWO, S. I.; CARREÑO, S. J. M.; MOURA, A. L.; RAPOSO, E. P.; GOMES, A. S. L.; ARAúJO, C. B. de. Observation of photonic paramagnetic to spin-glass transition in a specially designed TiO_2 particle-based dye-colloidal random laser. *Optics Letters*, Optica Publishing Group, v. 41, n. 15, p. 3459, Jul. 2016. ISSN 1539-4794. Available at: <http://dx.doi.org/10.1364/OL.41.003459>.

QI, Y.; NI, L.; YE, Z.; ZHANG, J.; BAO, X.; WANG, P.; RAO, Y.; RAPOSO, E. P.; GOMES, A. S. L.; WANG, Z. Replica symmetry breaking in 1d rayleigh scattering system: theory and validations. *Light: Science & amp; Applications*, Springer Science and Business Media LLC, v. 13, n. 1, Jul. 2024. ISSN 2047-7538. Available at: <http://dx.doi.org/10.1038/s41377-024-01475-5>.

RANCOURT, D. G.; LAMARCHE, G.; TUME, P.; LALONDE, A. E.; BIENSAN, P.; FLANDROIS, S. Dipole–dipole interactions as the source of spin-glass behaviour in exchangewise two-dimensional ferromagnetic layer compounds. *Canadian Journal of Physics*, Canadian Science Publishing, v. 68, n. 10, p. 1134–1137, Oct. 1990. ISSN 1208-6045. Available at: <http://dx.doi.org/10.1139/p90-160>.

RAPOSO, E. P.; GOMES, A. S. L. Analytical solution for the lévy-like steady-state distribution of intensities in random lasers. *Physical Review A*, American Physical Society (APS), v. 91, n. 4, Apr. 2015. ISSN 1094-1622. Available at: <http://dx.doi.org/10.1103/PhysRevA.91.043827>.

REYNOLDS, O. On the dynamical theory of incompressible viscous fluids and the determination of the criterion. [abstract]. *Proceedings of the Royal Society of London*, The Royal Society, v. 56, p. 40–45, 1894. ISSN 03701662. Available at: <http://www.jstor.org/stable/115570>.

RICHARDSON, L. *Weather Prediction by Numerical Process*. University Press, 1922. ISBN 9780342808670. Available at: <https://books.google.com.br/books?id=cWXWhffnUokC>.

SALAZAR, D. S. P.; VASCONCELOS, G. L. Stochastic dynamical model of intermittency in fully developed turbulence. *Physical Review E*, American Physical Society (APS), v. 82, n. 4, Oct. 2010. ISSN 1550-2376. Available at: <http://dx.doi.org/10.1103/PhysRevE.82.047301>.

SAPIENZA, R. Controlling random lasing action. *Nature Physics*, Springer Science and Business Media LLC, v. 18, n. 9, p. 976–979, Sep. 2022. ISSN 1745-2481. Available at: <http://dx.doi.org/10.1038/s41567-022-01655-3>.

SCHIEK, R. Nonlinear refractive index in silica glass. *Opt. Mater. Express*, Optica Publishing Group, v. 13, n. 6, p. 1727–1740, Jun 2023. Available at: <https://opg.optica.org/ome/abstract.cfm?URI=ome-13-6-1727>.

SET, S.; YAGUCHI, H.; TANAKA, Y.; JABLONSKI, M. Laser mode locking using a saturable absorber incorporating carbon nanotubes. *Journal of Lightwave Technology*, Institute of Electrical and Electronics Engineers (IEEE), v. 22, n. 1, p. 51–56, Jan. 2004. ISSN 0733-8724. Available at: <http://dx.doi.org/10.1109/JLT.2003.822205>.

SHERRINGTON, D.; KIRKPATRICK, S. Solvable model of a spin-glass. *Physical Review Letters*, American Physical Society (APS), v. 35, n. 26, p. 1792–1796, Dec. 1975. ISSN 0031-9007. Available at: <http://dx.doi.org/10.1103/PhysRevLett.35.1792>.

SHLENS, J. *A Tutorial on Principal Component Analysis*. arXiv, 2014. Available at: <https://arxiv.org/abs/1404.1100>.

SIQUEIRA, A. C. A.; PALACIOS, G.; BAUTISTA, J. E. Q.; AMARAL, A. M.; REYNA, A. S.; FILHO, E. L. Falcão; ARAÚJO, C. B. de. Observation of replica symmetry breaking in filamentation and multifilamentation. *Nanophotonics*, Walter de Gruyter GmbH, v. 14, n. 6, p. 757–767, Jan. 2025. ISSN 2192-8614. Available at: <http://dx.doi.org/10.1515/nanoph-2024-0592>.

SNITZER, E. Proposed fiber cavities for optical masers. *Journal of Applied Physics*, AIP Publishing, v. 32, n. 1, p. 36–39, Jan. 1961. ISSN 1089-7550. Available at: <http://dx.doi.org/10.1063/1.1735955>.

SREENIVASAN, K. R. On the universality of the kolmogorov constant. *Physics of Fluids*, AIP Publishing, v. 7, n. 11, p. 2778–2784, Nov. 1995. ISSN 1089-7666. Available at: <http://dx.doi.org/10.1063/1.868656>.

SREENIVASAN, K. R.; KAILASNATH, P. An update on the intermittency exponent in turbulence. *Physics of Fluids A: Fluid Dynamics*, AIP Publishing, v. 5, n. 2, p. 512–514, Feb. 1993. ISSN 0899-8213. Available at: <http://dx.doi.org/10.1063/1.858877>.

STEIN, D. L. Spin glasses. *Sci. Am.*, Springer Science and Business Media LLC, v. 261, n. 1, p. 52–59, Jul. 1989.

STOKES, G. G. On the steady motion of incompressible fluids. In: _____. *Mathematical and Physical Papers vol.1*. Cambridge University Press, 1842. p. 1–16. Available at: <http://dx.doi.org/10.1017/CBO9780511702242.002>.

SVELTO, O.; HANNA, D. *Principles of Lasers*. Springer US, 2013. ISBN 9781489927484. Available at: <https://books.google.co.zw/books?id=rAYHCAAAQBAJ>.

TAYLOR, G. I. Statistical theory of turbulenc. *Proceedings of the Royal Society of London. Series A - Mathematical and Physical Sciences*, The Royal Society, v. 151, n. 873, p. 421–444, Sep. 1935. ISSN 2053-9169. Available at: <http://dx.doi.org/10.1098/rspa.1935.0158>.

THOMAS, G.; ISAACS, R. Basic principles of lasers. *Anaesthesia & amp; Intensive Care Medicine*, Elsevier BV, v. 12, n. 12, p. 574–577, dec 2011. ISSN 1472-0299. Available at: <http://dx.doi.org/10.1016/j.mpaic.2011.09.013>.

THOULESS, D. J.; ANDERSON, P. W.; PALMER, R. G. Solution of "solvable model of a spin glass". *Philosophical Magazine*, Informa UK Limited, v. 35, n. 3, p. 593–601, mar 1977. ISSN 0031-8086. Available at: <http://dx.doi.org/10.1080/14786437708235992>.

TREACY, E. Optical pulse compression with diffraction gratings. *IEEE Journal of Quantum Electronics*, Institute of Electrical and Electronics Engineers (IEEE), v. 5, n. 9, p. 454–458, Sep. 1969. ISSN 1558-1713. Available at: <http://dx.doi.org/10.1109/JQE.1969.1076303>.

UPPU, R.; MUJUMDAR, S. Lévy exponents as universal identifiers of threshold and criticality in random lasers. *Physical Review A*, American Physical Society (APS), v. 90, n. 2, Aug. 2014. ISSN 1094-1622. Available at: <http://dx.doi.org/10.1103/PhysRevA.90.025801>.

VASCONCELOS, G. L.; RIBEIRO, L. R. C.; MACÊDO, A. M. S.; GONZÁLEZ, I. R. R.; OSPINA, R.; BRUM, A. A. Turbulence hierarchy in foreign exchange markets. *Physical Review E*, American Physical Society (APS), v. 109, n. 4, Apr. 2024. ISSN 2470-0053. Available at: <http://dx.doi.org/10.1103/PhysRevE.109.044313>.

VILLAIN, J. Insulating spin glasses. *Zeitschrift für Physik B Condensed Matter and Quanta*, Springer Science and Business Media LLC, v. 33, n. 1, p. 31–42, Mar. 1979. ISSN 1434-6036. Available at: <http://dx.doi.org/10.1007/bf01325811>.

VUGMEISTER, B. E.; GLINCHUK, M. D. Dipole glass and ferroelectricity in random-site electric dipole systems. *Reviews of Modern Physics*, American Physical Society (APS), v. 62, n. 4, p. 993–1026, Oct. 1990. ISSN 1539-0756. Available at: <http://dx.doi.org/10.1103/revmodphys.62.993>.

WEINER, A. *Ultrafast Optics*. Wiley, 2011. (Wiley Series in Pure and Applied Optics). ISBN 9781118211472. Available at: <https://books.google.com.br/books?id=fhohaV7wJbYC>.

WEISSMAN, M. B. What is a spin glass? a glimpse via mesoscopic noise. *Rev. Mod. Phys.*, American Physical Society (APS), v. 65, n. 3, p. 829–839, Jul. 1993.

WIERSMA, D. The smallest random laser. *Nature*, Springer Science and Business Media LLC, v. 406, n. 6792, p. 133–135, Jul. 2000. ISSN 1476-4687. Available at: <http://dx.doi.org/10.1038/35018184>.

WIERSMA, D. S. The physics and applications of random lasers. *Nature Physics*, Springer Science and Business Media LLC, v. 4, n. 5, p. 359–367, May 2008. ISSN 1745-2481. Available at: <http://dx.doi.org/10.1038/nphys971>.

YAMAZAKI, H.; LUECK, R. G.; OSBORN, T. A comparison of turbulence data from a submarine and a vertical profiler. *Journal of Physical Oceanography*, American Meteorological Society, v. 20, n. 11, p. 1778–1786, Nov. 1990. ISSN 1520-0485. Available at: <http://dx.doi.org/10.1175/1520-0485(1990)020<1778:ACOTDF>2.0.CO;2>.

YOUNG, A. P. Direct determination of the probability distribution for the spin-glass order parameter. *Physical Review Letters*, American Physical Society (APS), v. 51, n. 13, p. 1206–1209, sep 1983. ISSN 0031-9007. Available at: <http://dx.doi.org/10.1103/PhysRevLett.51.1206>.

ZALLEN, R. *The physics of amorphous solids*. Nashville, TN: John Wiley & Sons, 1998. (Wiley classics library).

ZERVAS, M. N.; CODEMARD, C. A. High power fiber lasers: A review. *IEEE Journal of Selected Topics in Quantum Electronics*, Institute of Electrical and Electronics Engineers (IEEE), v. 20, n. 5, p. 219–241, Sep. 2014. ISSN 1558-4542. Available at: <http://dx.doi.org/10.1109/jstqe.2014.2321279>.

ZHOU, G. F.; BAKKER, H. Spin-glass behavior of mechanically milled crystalline $GdAl_2$. *Physical Review Letters*, American Physical Society (APS), v. 73, n. 2, p. 344–347, Jul. 1994. ISSN 0031-9007. Available at: <http://dx.doi.org/10.1103/PhysRevLett.73.344>.

ZIMNYAKOV, D.; VOLCHKOV, S.; KOCHUBEY, V.; PLEKHANOVA, I.; DOROGOV, A. Fluorescence amplification in laser-pumped random media: Fundamental limitations. *Journal of Luminescence*, Elsevier BV, v. 272, p. 120667, Aug. 2024. ISSN 0022-2313. Available at: <http://dx.doi.org/10.1016/j.jlumin.2024.120667>.

ANNEX A – DATA AUTOMATION VIA PYTHON

Listing 2 – Acquisition code for the automation of the experiment.

```
# ========================= IMPORT LIBRARIES =========================
import time                          # Time-related functions
import pyvisa                        # Instrument communication (e.g., via USB, GPIB)
import numpy as np                   # Numerical operations, arrays
import pandas as pd                  # Data handling (not used here, could be removed)
import pyautogui as ag               # GUI automation (clicks, typing)
import pygetwindow as gw             # Window management
from pathlib import Path             # File path management
from datetime import date            # Date handling
from seabreeze.spectrometers import Spectrometer  # Spectrometer interface


# ========================= DEFINE FUNCTIONS =========================
def spec_collection(spectrometer, samples, c, r):
    """
    Collect spectral data from the spectrometer.

    Parameters:
    - spectrometer: Spectrometer object
    - samples: Number of spectral measurements to take
    - c: Current collection index (for display)
    - r: Current round index (for display)

    Returns:
    - data: List containing wavelengths and intensity measurements
    """

    # Get the full range of wavelengths from the spectrometer
    wavelengths = spectrometer.wavelengths()

    # Keep only wavelengths within the desired range
    wavelengths_column = [i for i in wavelengths if low_limit <= i <= high_limit + 1]

    # Initialize data array with the wavelengths as the first row
    data = [wavelengths_column]

    # Loop through the requested number of samples
    for i in range(0, samples):
        # Acquire intensity measurement from the spectrometer
        intensity = spectrometer.intensities()
```

```
42          # Filter intensities to match wavelength range
            temp_data = [q for (p, q) in zip(wavelengths, intensity) if low_limit <=
                p <= high_limit + 1]
44
            # Append filtered intensities to data (tuple for faster appending)
46          data += temp_data,

48      return data

50  # ========================= GLOBAL VARIABLES =========================
    low_limit = 980                 # Minimum wavelength (nm)
52  high_limit = 1065               # Maximum wavelength (nm)
    total_replicas = 150000         # Number of spectra per collection
54  n_collection = 10               # Number of voltage points to collect
    rounds = 2                      # Number of repeats per voltage
56  start = 690                     # Initial voltage (mV)
    integration_time = 6000         # Spectrometer integration time (microseconds)
58  step = -35                      # Voltage increment per collection (mV)

60  # ========================= SET UP FILE PATHS =========================
    in_path = r'D:\LaserYb\Medidas Espectrometro'   # Spectrometer data folder
62  in_path_2 = r'D:\LaserYb\Optical Power Data'   # Optical Power Monitor data
        folder

64  # Get current date and time
    today = date.today().strftime('%d_%m_%Y')
66  hour = time.strftime("%H_%M", time.localtime())

68  # Record start time for total program
    t_time = time.time()
70
    # Create folders to save the data if they don't exist
72  Path(rf'{in_path}\{today}\{hour}\Information').mkdir(parents=True, exist_ok=True)
    Path(rf'{in_path}\{today}\{hour}\binary_data').mkdir(parents=True, exist_ok=True)
74  Path(rf'{in_path_2}\{today}\{hour}').mkdir(parents=True, exist_ok=True)

76  # ========================= SET UP WAVEFORM GENERATOR =========================
    rm = pyvisa.ResourceManager()  # Initialize VISA resource manager
78  wave_generator = rm.open_resource('USB0::0x0957::0x2C07::MY52812459::INSTR')  #
        Connect to generator
    wave_generator.write('FUNCtion DC')                     # Set generator to DC
        output
80  wave_generator.write(f'VOLTage:OFFS +{start / 1000}')     # Set initial voltage (
        V)
    wave_generator.write('OUTPut1 1')                       # Turn output ON
82
```

```
# ========================= SET UP SPECTROMETER =========================
spec = Spectrometer.from_first_available()                # Connect to first available spectrometer
spec.integration_time_micros(integration_time)            # Set integration time
print('Start program')

# ========================== SET UP OPTICAL POWER MONITOR ==========================
opm = gw.getWindowsWithTitle('Optical Power Monitor')[0]  # Get OPM window
path_opm = rf'{in_path_2}\{today}\{hour}'

# Make sure the OPM window is maximized and active
while opm.isMaximized == False:
    opm.maximize()
    opm.activate()

# Set file path in OPM software using pyautogui
ag.click(1214, 200)   # Click file path input
ag.hotkey('ctrl', 'a')
ag.press('delete')
ag.write(path_opm)

# Countdown before starting
for countdown in range(5):
    print(f'Begin program in {5 - countdown} s')
    time.sleep(1)

# ========================= MAIN DATA COLLECTION LOOP =========================
for i in range(n_collection):

    # Target voltage for this collection (mV)
    target_voltage = start + step * i

    # Get current voltage from generator (assume we track it in a variable)
    try:
        current_voltage = float(wave_generator.query('VOLTage:OFFS?')) * 1000  # Convert V to mV
    except:
        current_voltage = start  # fallback if query fails

    # Ramp voltage 1 mV per second until it reaches target
    while current_voltage < target_voltage:
        current_voltage += 1  # increase by 1 mV
        if current_voltage >= target_voltage:
            current_voltage = target_voltage  # do not overshoot
        wave_generator.write(f'VOLTage:OFFS +{current_voltage / 1000}')  # convert mV to V
```

```
126         wave_generator.write('OUTPut1 1')  # ensure output is ON
            time.sleep(1)  # wait 1 second per 1 mV
128
        # Repeat collection for number of rounds
130     for j in range(rounds):
            # Define file path to save spectrometer data
132         path_spec = rf'{in_path}\{today}\{hour}\binary_data\b_data_{(start + step
                * i)}_{j}'

134         # Control OPM software GUI to set file name and start logging
            ag.click(1080, 81)      # Open settings tab
136         ag.click(1199, 256)     # Click file name input
            ag.hotkey('ctrl', 'a')
138         ag.press('delete')
            ag.write(f'opm_data_{(start + step * i)}_{j}')  # Insert filename
140         ag.click(1200, 666)     # Start logging

142         # Record start time for this collection
            start_time = time.time()
144         c_time = time.ctime()

146         # Collect spectral data
            dados = spec_collection(spec, total_replicas, (i) + 1, j + 1)
148
            # Convert data to numpy array and save
150         final_data = np.array(np.transpose(dados))
            np.save(rf'{path_spec}.npy', final_data)
152
            # Calculate elapsed time
154         end_time = (time.time() - start_time)

156         # Stop OPM logging
            ag.click(1200, 666)
158
            print('\n')
160         print("Time taken: --- %s seconds ---" % (end_time))

162         # Save collection info in a text file
            with open(rf'{in_path}\{today}\{hour}\Information\info_{i+1}_{j}.txt', 'w
                ') as f:
164             f.write('Important information:\n')
                f.write('Collection number %s\n' % (i+1))
166             f.write('Begin: %s \n' % (c_time))
                f.write('End: %s \n' % (time.ctime()))
168             f.write('Range: %s to %s \n' % (low_limit, high_limit))
                f.write('Voltage (mV): %s \n' % (start + step * i))
170             f.write('Samples: %s \n' % total_replicas)
```

```
            f.write('Time taken: --- %s seconds ---\n' % end_time)

        print('\n')

# Print total program runtime
print("Total time --- %s seconds ---" % (time.time() - t_time))
```

Source: The Author (2025)